A Polarization Sensitive Interferometer for Faraday Rotation Detection

by

Joshua Michael LaForge
B.Sc.(Honours) University of Alberta 2004

A Thesis Submitted in Partial Fullfillment of the
Requirements for the Degree of

MASTER OF SCIENCE

in the Department of Physics and Astronomy

© Joshua Michael LaForge, 2007
University of Victoria

All rights reserved. This thesis may not be reproduced in whole or in part, by photocopy or other means, without the permission of the author.

A Polarization Sensitive Interferometer for Faraday Rotation Detection

By

Joshua Michael LaForge

B.Sc.(Honours) University of Alberta 2004

Supervisory Committee

Dr. Geoffrey Steeves
Department of Physics and Astronomy

Dr. Byoung-Chul Choi
Department of Physics and Astronomy

Dr. Matthew Moffitt
Department of Chemistry

Dr. Alexandre Brolo, (External Examiner)
Department of Chemistry

Supervisory Committee

Dr. Geoffrey Steeves
Department of Physics and Astronomy

Dr. Byoung-Chul Choi
Department of Physics and Astronomy

Dr. Matthew Moffitt
Department of Chemistry

Dr. Alexandre Brolo, (External Examiner)
Department of Chemistry

Abstract

Time-resolved Faraday rotation (TRFR) is a pulsed laser pump/probe optical measurement used to characterize electron spin dynamics in semiconductor materials. A Mach-Zehnder type interferometer with orthogonally polarized arms is presented as a device for TRFR measurement that is superior to optical bridge detection, the traditional measuring technique, since Faraday rotation can be passively optically amplified via interference. Operation of the interferometer is analyzed under ideal conditions. Corrections to the ideal case stemming from imperfectly aligned optics, finite polarization extinction ratios, and an imperfect recombination optic are analyzed using a matrix transformation approach. The design of the interferometer is presented and chronicled. A description of the single-beam active control system utilized to stabilize the interferometer by continuous corrections to the optical path

length of one arm with a piezoelectric actuator is given. Optical amplification by increasing the power in either arm of the interferometer is demonstrated and TRFR measurements taken with the interferometer at ambient temperatures are compared with measurements taken with the optical bridge. We find the interferometer to offer a detection limit on the order of 50 mrad at room temperature, which is five times more sensitive than the optical bridge. Isolation and stabilization of the interferometer were also successful in reducing signal noise to a level comparable with the optical bridge. Our results demonstrate that the interferometer is a better detection device for Faraday rotation under ambient conditions. In the immediate future, improvements to the control system should be made and experiments should be performed with high-quality samples at cryogenic temperatures to confirm that the interferometer performs as favorably under those conditions.

Table of Contents

List of Figures

List of Tables

Acknowledgments

Funding support from the Natural Sciences and Engineering Research Council of Canada (NSERC), and the Canadian Foundation for Innovation, and the University of Victoria has enabled the project's completion.

Contributions from my colleagues Alex Wlasenko, Daniel Lidstrom and Alastair Fraser have been important during various phases of the project.

The technical staff at the University of Victoria including electronics technicians Nicolas Braam, Reece Hasanen and Neil Honkanen as well as machinist David Smith have been invaluable sources of expertise. Their assistance has been greatly appreciated.

The faculty and staff as the University of Victoria especially Dr. B.C. Choi, and Dr. Reuven Gordon have provided helpful input and shared necessary equipment.

Lastly my supervisor Dr. Geoffrey Steeves has been a steady hand of guidance throughout the course of the project. His continued support in terms of technical advice, and resources has made this project possible.

Dedication

Mom and Dad,

You have always strived to provide me with the conditions and tools necessary to achieve my dreams. None of this would have been possible without your relentless devotion, your constant encouragement, and your love. Thank you.

Chapter 1

Introduction

Spintronics is the field of research focused on the utilization of electron spin, the intrinsic angular momentum and magnetic moment of electrons, for academic and technological purposes. The field has already met some technological success; the high-density magnetic storage found in modern hard-disks is made possible by our understanding of a spintronic effect: giant magneto-resistance (GMR) [1, 2, 3, 4]. Current research activities in the field focus on applications in both classical and quantum information processing and storage. Spin sensitive devices have the potential to provide nonvolatile solid-state memory (MRAM), an increase in data processing speed (Spin-FET), and an overall decrease in power consumption over today's semiconductor electrical devices. [5, 6]

Successful development of spin-based technologies requires an understanding of

the spin dynamics in semiconductor materials; spin mobility, coherence times, and coupling dynamics need to be understood. Efficient, versatile detection schemes for studying material properties are needed to study spin dynamics. Time-Resolved Faraday Rotation (TRFR) is one such optical pump/probe experimental technique that is used to study both temporal [7] and spatial spin dynamics. [8].

1.1 Time Resolved Faraday Rotation

Optical TRFR experiments are versatile in that many diverse sample configurations and materials can be used (ie. bulk, quantum wells, quantum dots). The only requirement is that the laser beam used for detection be transmitted (or reflected for Time Resolved Kerr Rotation) through the sample. This has led to experiments on many different semiconductor materials in bulk form, two-dimensional quantum wells, and quantum dots.

All optical TRFR measurements consist of two pulsed laser beams named the pump and probe beam which are circularly and linearly polarized respectively. The light from the pump pulse is absorbed by the semiconductor sample. Momentum transfer from photons in the circularly polarized light to electrons in the material creates an optical orientated, spin polarized state in the conduction band of the semiconductor sample.

1.1.1 Optical Orientation

Now it would be appropriate to briefly discuss the theory of optical orientation and how circularly polarized light creates a spin polarized state in semiconductors. For a more complete discussion see *Optical Orientation*[9]. Consider GaAs, a III-V semiconductor material [10] that we have used as our test sample in bulk form. The valence band in GaAs at the zero momentum (k=0) point, the center of the Brillouin zone (Γ-point), consists of three twice spin degenerate sub-bands: the heavy-hole sub-band, the light-hole sub-band, and the split-off sub-band. A schematic of the conduction and valence bands in gallium arsenide is given in Fig.1.1.[9]

Allowed optically excited inter-band transitions between the valence bands and conduction bonds near k=0 are governed by a set of selection rules. To find the allowed transitions and their probabilities consider the correspondence between quantum transitions and a classical dipole with frequency $\omega_{ab} = (E_a - E_b)/\hbar$ [9], where a and b are quantum states. The amplitude of the dipole moment is equal to the transitions matrix element given by:

$$\mathbf{D_{ab}} =< a|\hat{\mathbf{D}}|b > \tag{1.1}$$

Using the wave-functions for electrons in the valence and conduction bands for cubic semiconductors, like gallium arsenide, and directing the quantization axis (z-

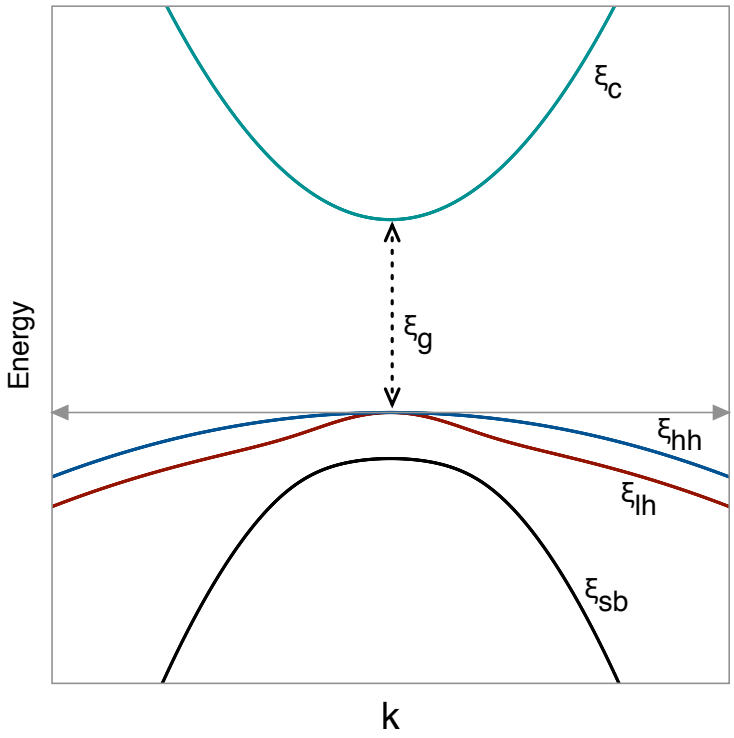

Figure 1.1: Schematic of the conduction (ε_c) and valence bands at the Γ-point (k=0) in gallium arsenide. The valence band is composed of the heavy-hole band (ε_{hh}), the light-hole band (ε_{lh}), and the split-off band (ε_{sb}), which is separated by the spin-orbit splitting energy δ from the heavy-hole and light-hole bands.

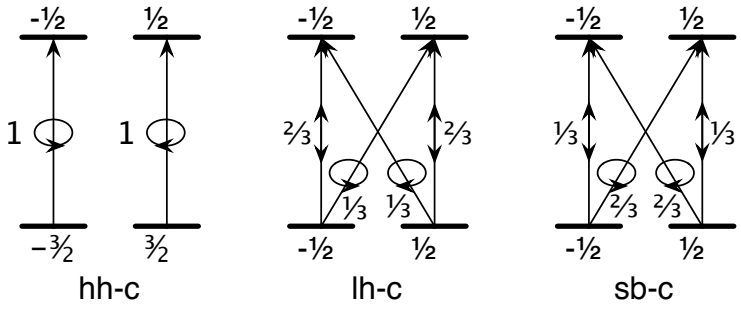

Figure 1.2: Dipoles corresponding to various inter-band transitions. The numbers near the arrows representing the dipoles indicate the relative transition intensities. The numbers near the levels correspond to the projection of the total angular momentum on the quantization axis directed along the quasi-momentum.[9]

axis) along the wave vector $\mathbf{k}$ the matrix elements of the dipole moment can be found [9, 11]. The only none zero elements are

$$< S|D_x|X >=< S|D_y|Y >=< S|D_z|Z > \tag{1.2}$$

A diagram of the dipoles corresponding to various inter-band transitions is given in Fig.1.2.

A density matrix, $\hat{F}(\mathbf{k})$, is used to calculate the momentum and spin distribution of electrons generated in the conduction band by the absorption of light.

$$F_{mm'}(\mathbf{k}) \sim \sum_{M} (\mathbf{D_{mM}e})(\mathbf{D_{m'M}e})^* \tag{1.3}$$

Where $\mathbf{e}$ is the unit polarization vector, $\mathbf{D}$ is the dipole transition matrix, m,m'

are the spin indices of an electron in the conduction band assuming values of $\pm\frac{1}{2}$, and the summation index M denotes two degenerate states in each sub-band of the valence band.

Using the density matrix the average spin of an electron with a given direction of momentum excited with right circularly polarized light at the instant of creation can be found. The various transitions from the valence sub-bands are given below:

$$\begin{aligned} \text{hh-c:} \quad & \mathbf{S}_o(\vec{\nu}) = -\tfrac{\vec{\nu}(\vec{\nu}\cdot\vec{n})}{1+(\vec{\nu}\cdot\vec{n})^2} \\ \text{lh-c:} \quad & \mathbf{S}_o(\vec{\nu}) = \tfrac{3\vec{\nu}(\vec{\nu}\cdot\vec{n})-2\vec{n}}{5-3(\vec{\nu}\cdot\vec{n})^2} \\ \text{sb-c:} \quad & \mathbf{S}_o(\vec{\nu}) = \tfrac{1}{2}\vec{n} \end{aligned} \tag{1.4}$$

Where $\vec{n}$ and $\vec{\nu}$ are unit vectors in the direction of the pump beam and electron momentum respectively. Average values over all momentum vectors reveal that the heavy-hole, light-hole and sub-band transitions have an average spin along $\vec{n}$ (the z-axis) at the moment of photo-creation of $-\frac{1}{4}$, $-\frac{1}{4}$, and $\frac{1}{2}$ respectively. At the moment of creation electrons with momentum along the direction of the excited beam are completely orientated. Transitions from the light-hole band and sub-band are orientation along the photon angular momentum, whereas transitions from the heavy-hole band are aligned oppositely.

In effect, spin polarization of the excited state depends on the different transition

probabilities of electrons from the valence bands (Fig.1.2). When exciting electrons from the heavy-hole and light-hole band, there is a preference for the heavy-hole transition which leads to an overall net polarization in the conduction band.

Spin polarization of the excited state depends strongly on the energy of the exciting photons. When the energy of the photons exceeds the sum of the band-gap and the spin-orbit splitting energy ($\hbar\omega > \epsilon_g + \delta$) electrons from the sub-band are excited as well as from the heavy-hole and light-hole bands. Since the spins from sub-band transitions are oppositely aligned (on average) to the heavy-hole and light-hole transitions the degree of polarization of the excited state decreases and eventually reaches zero. Thus the wavelength of the pump beam during experiments is optimized near the band-gap energy to create an optimally polarized excited state, which will in turn create a stronger Faraday rotation signal.

With p-doped semiconductors it is clear from the above discussion that excitation of electrons is going to lead to a spin-polarized state of minority carriers in the conduction band. The situation is different in n-type semiconductors (n-type semiconductors were used for our experiments). Optical orientation is achieved in n-type materials by adding oriented photo-excited electrons to the conduction band that replace non-oriented electrons that are recombined with the holes generated during photo-excitation. The degree of polarization will thus increase with the irradiance of the pump beam until saturation occurs when all valence electrons are depleted.

1.1.2 Spin Precession and Relaxation

In TRFR experiments the semiconductor samples are placed in an external magnetic field. Our experiments used the Voigt geometry, where the magnetic field is in the plane of the sample's surface, and perpendicular to the pump and probe beams.

Zeeman splitting along the magnetic field causes electrons to precess around the field at the Larmor frequency shown in Eq.1.5. Where g is the Landé g-factor (typical values of -0.44 for GaAs), μ_B is the Bohr magneton, and B is the magnetic field.

$$\nu_L = \frac{g\mu_B}{\hbar} B_{total} \tag{1.5}$$

Inhomogeneities in the g-factor will cause spin de-phasing as electrons precess at different frequencies.

Spin relaxation comes from three major sources: spin-orbit interactions due to a lack of inversion symmetry (D'yakonov-Perel' mechanism), band-mixing (Elliott-Yafet mechanism), and electron-hole exchange interaction (Bir-Aronov-Pikus mechanism).[9] These relaxation mechanisms will play different roles in p-type and n-type GaAs and their strengths will have an affect on the spin lifetime.[12, 13]

Holes in the valence band relax more rapidly than electrons due to the strong spin-orbt interaction in the valence band. However under crystal deformation it is possible to slow down the relaxation of holes with sufficiently small energy, smaller

than the deformational splitting, ΔE (for GaAs $\Delta E \approx 10$ meV / kBar).

Spin relaxation times can be either shorter or longer than the carrier recombination time. However in p-type semiconductors carrier recombination depletes the spin-polarization, even in situations were the spin relaxation is an order of magnitude longer.[14] Oppositely, in n-type GaAs spin lifetimes longer than the carrier recombination time have been demonstrated.[15, 16] Obviously this is caused by the persistence of polarized electrons in the conduction band due to a lack of holes with which to recombine.

1.1.3 Faraday Rotation

At some variable delay time Δt a linearly polarized probe pulse arrives and is transmitted through the sample. Circular dichroism in the sample due to the spin polarized excited state will result in the rotation of the plane of polarization of the probe beam.[17] In effect, the rotation of the probe pulse records the projection of the net magnetization of electrons along the beam direction. This is the Faraday effect, which is described by Eq. 1.6 [18], where δ is the angle of rotation, V is the Verdet constant, B is the magnetic flux density and d is the thickness of the material.

$$\delta = VBd \tag{1.6}$$

By varying the delay time the temporal evolution of the electron spin precession is measured indirectly via the detection of the angle of rotation induced upon the polarization axis of the probe beam.

In the Voigt geometry this will lead to a time-varying signal of the form:

$$\delta(t) = Ae^{-\Delta t/T_2^*}\cos(2\pi\nu_L\Delta t) \tag{1.7}$$

Where T_2^* is the effective transverse spin lifetime, which can include contributions from both the longitudinal (T_1) and transverse (T_2) spin relaxation times.[17]

1.2 Faraday Rotation Detection

1.2.1 Optical Bridge Detection

Traditionally the rotation of the probe beam's polarization axis has been detected using the optical bridge technique (Fig.1.3).[7] In this detection method the probe beam is transmitted through a half-wave plate, split by a polarizing beam splitter and then collected by two photodiodes. Before a measurement is taken the half-wave plate's fast axis is orientated so that without any Faraday rotation the photodiodes are balanced: the difference signal between the two diodes is zero.

The difference signal between the two photodiodes PDA and PDB is related to

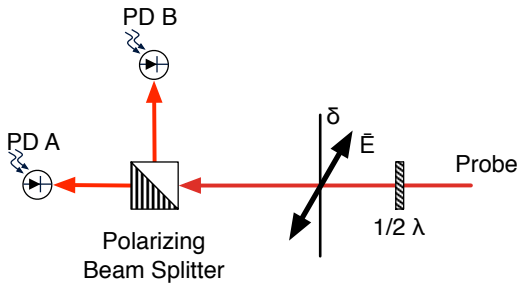

Figure 1.3: Optical bridge setup with the polarization axis of the probe beam rotated by an angle δ.

the optical power of the probe beam, P_{Probe}, and the angle of rotation, δ, for small angles, by Eq.1.8 derived in §2.1.

$$A - B = 2 < P_{Probe} > \delta \tag{1.8}$$

The optical bridge technique has been successful at reaching rotation resolutions on the order of 10 nano-radians (nrad), for probe beam powers of approximately $10\mu W$.[19, 16] Experiments on colloidal quantum dot films probe approximately $10^5 - 10^6$ individuals dot at once to produce a measurable signal.[19, 20].

Quantum dot systems hold interest for spintronic devices particularly as candidates for quantum information processing [21, 22] since electron spin coherence times are longer in quantum dots than in high-dimensional systems [23, 24]. The increase in spin coherence times is due to a decrease in coupling to the surrounding environment and fewer internal degrees of freedom. Longer coherence times are important, since it

allows more time for useful interactions to take place between coupled electron spins [25, 6], which is particularly important for quantum error correction[26].

An understanding of interaction between low-dimensional systems, like quantum dots, requires an increase in the sensitivity of the optical bridge technique. It is apparent from Eq.1.8 that the probe beam power can be increased to increase the detection sensitivity. However, the probe power is limited so as to remain non-invasive to the sample, thereby creating a maximum achievable sensitivity.

Several constraints limit the probe power to remain non-invasive. Obviously, the probe beam's power is kept to a fraction of the pump beam's power. The probe power is also kept low to limit sample heating, prevent extra carrier excitation that can lead to an increase in spin scattering via spin-spin interactions, and in the case of some colloidal quantum dot samples, to avoid sample bleaching.

Recently optical cavities have been used to increase the sensitivity of the optical bridge measurement technique by increasing the interaction of the probe pulse with the sample.[27] This technique has been used to read a single electron spin on a quantum dot.[28]

However there is motivation to develop a new detection technique that avoids the limitations in probe power, and does not require special optical cavity samples.

1.2.2 Interferometric Detection

We present a novel method to increase the sensitivity to Faraday rotation using a Mach-Zehnder (two-armed) interferometer.[18] This idea was originally presented in the theoretical work of Dr. Y.Yamamoto.[29] Our initial interest in examining the spin properties of novel quantum dot materials led us to investigate the interferometer as an unexplored method that could be used to increase the sensitivity of Faraday rotation detection non-invasively.

The interferometer splits the probe beam into two orthogonal polarization components with a polarizing beam splitting cube. The y-component propagates along the signal arm where it interacts with the sample, and the x-component propagates in the local arm unchanged. A basic schematic outlining the principal operation of the interferometer is shown in Fig.1.4.

Faraday rotation caused by interaction with the sample causes the polarization axis of the signal beam to rotate slightly. The signal beam then passes through a polarizer that transmits only the x-component. Thus, information about the degree of rotation is contained in the power of the beam after the polarizer. The local and signal beam are recombined with a 50:50 non-polarizing beam splitter and detected with photodiodes PDA and PDB. Only the difference signal between photodiodes PDA and PDB is measured. The difference signal is related to the optical power in the signal and local arm, as well as the angle of rotation, δ, and the phase difference,

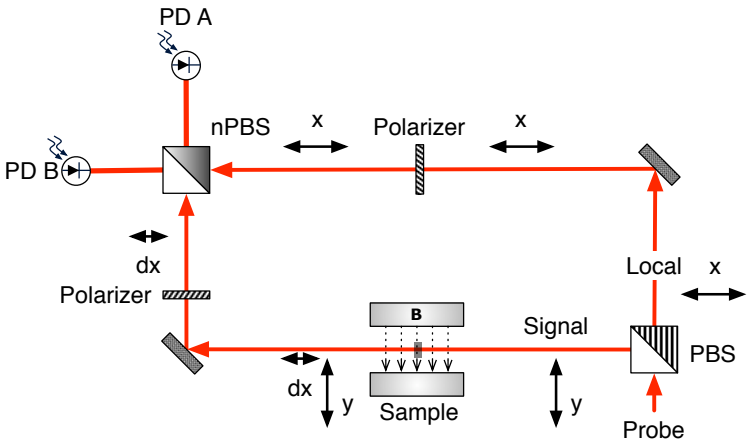

Figure 1.4: Mach-Zehnder interferometer setup. PBS is a Polarizing Beam Splitter and nPBS is a 50:50 Non-Polarizing Beam Splitter.

ϕ, between the two arms by Eq. 1.9 for small angles of rotation (see §2.2 for the derivation).

$$A - B = 2\sqrt{< P_{Signal} >< P_{Local} >}\,\delta \sin\phi \tag{1.9}$$

Using the interferometer has introduced an extra factor, the power in the local arm, to the difference signal: there are now two options for increasing the strength of the measured signal. The power in the signal arm can be increased, which is analogous to increasing the probe power in the optical bridge setup. Alternatively, and more importantly, the measured signal can be strengthened by increasing the power in the local arm. In other words the Faraday rotation can be passively optically amplified through the interference of the signal arm and local arm.

Unlike the signal arm where the maximum power is limited to be non-invasive to

the sample, the power in the local arm is only limited by the optical components used to create the interferometer and the detection devices. Thus P_{Local} can be increased to compensate for a reduction P_{Signal} and/or to amplify the Faraday rotation, δ.

The flexibility and sensitivity gained by using an interferometer comes at the cost of coupling vibrational sources of noise into the difference signal via the phase difference between the two arms, ϕ. Careful attention must be paid to placing the interferometer into a vibrational and acoustically isolated environment while performing measurements. A significant amount of time during the project was devoted to the reduction and elimination of environmental noise sources coupled into the difference signal through ϕ. ;

Chapter 2

Theory of Operation

2.1 Optical Bridge Detection of Faraday Rotation

Typically Faraday rotation caused by the magnetic moment of electrons in semiconductor materials is measured with the optical bridge technique (Fig.2.1).[7] In this detection scheme the probe beam is transmitted through a half wave plate which is used to calibrate the polarization axis of the beam. A polarizing beam splitter cube then splits the beam into two beams with orthogonal linear polarization. The two orthogonally polarized beams are detected separately with two photo-diodes and the difference signal between the diodes is measured.

Before the detector is used the half wave plate is calibrated such that in the absence of a Faraday rotation the two photo-diodes are balanced; the difference signal between

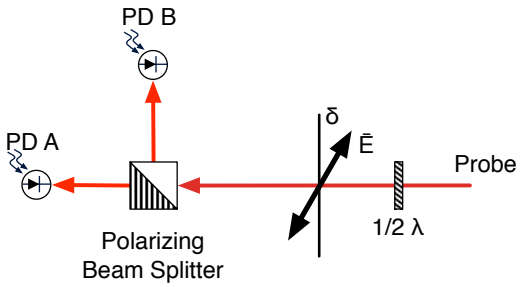

Figure 2.1: Optical bridge setup with the polarization axis of the probe beam rotated by an angle δ.

the two diodes is zeroed. Thus, any rotation in the beam causes a proportional imbalance in the difference signal. Splitting the photodiodes this way and measuring the difference signal eliminates any common mode noise, such as power fluctuations from the laser, since both diodes will track the power fluctuations in the same way and will thus not affect the difference signal.[7]

The electric field of the beam after the half-wave plate is made of two separate polarization components.

$$\vec{E} = E_x\hat{x} + E_y\hat{y}$$

Before any sample interactions the two components are equal, such that the dif-

ference between the signals at the two photodiodes, PDA and PDB, is zero.

$$E_x = E_y = \frac{E}{\sqrt{2}}$$
$$\therefore \vec{E}_A = \frac{E}{\sqrt{2}}\hat{x} \qquad \vec{E}_B = \frac{E}{\sqrt{2}}\hat{y}$$
$$\vec{E} = \frac{E}{\sqrt{2}}\hat{x} + \frac{E}{\sqrt{2}}\hat{y} \tag{2.1}$$

Equation 2.1 can be written in a general parametric form::

$$\vec{E} = E\cos\theta\hat{x} + E\sin\theta\hat{y} \tag{2.2}$$

Where $\theta = 45^\circ$ without Faraday Rotation at the sample is equivalent to Eq. 2.1.

$$\therefore |\vec{E}_A|^2 = E_A^2 = E^2\cos^2\theta \qquad |\vec{E}_B|^2 = E_B^2 = E^2\sin^2\theta$$

The photodiodes cannot measure the electric field of the beams directly. Instead the irradiance (the average energy per unit area per unit time) [18] of the beam is measured.

$$A_{Irradiance} = A = \left\langle |\vec{S}_A| \right\rangle$$

Where <> denotes the time average over the Poynting vector (instantaneous

power per unit area), $\vec{S_A}$, for the beam at PDA.

$$A = \epsilon_0 c < E_A^2 >= \epsilon_0 c < E^2 > \cos^2\theta$$

Where ϵ_0 is the permittivity of free space and c is the speed of light. Similarly,

$$B = \epsilon_0 c < E^2 > \sin^2\theta$$

Thus the difference signal between the two photodiodes A and B is proportional to the difference between E_A^2 and E_B^2 assuming the photodiodes are the same.

$$A - B \propto \epsilon_0 c < E^2 > (\cos^2\theta - \sin^2\theta)$$

For now neglect the time average and physical constants for now.

For small chances in θ

$$\theta = 45^\circ + \delta$$

Or in radians

$$\theta = \frac{\pi}{4} + \delta$$

Where $\delta << 1$ during experiments (typical rotations due to the Faraday effect are

on the order of μrad to mrad).

$$A = E^2 \cos^2(\frac{\pi}{4} + \delta) \qquad B = E^2 \sin^2(\frac{\pi}{4} + \delta)$$

$$\therefore A - B = E^2 \left(\cos^2(\frac{\pi}{4} + \delta) - \sin^2(\frac{\pi}{4} + \delta)\right)$$

A and B can be simplified in the following way with two trigonometric identities.

$$\cos(u + v) = \cos u \cos v - \sin u \sin v$$

$$\sin(u + v) = \sin u \cos v + \cos u \sin v$$

$$\cos^2(\frac{\pi}{4} + \delta) = \left(\frac{\cos\delta}{\sqrt{2}} - \frac{\sin\delta}{\sqrt{2}}\right)^2$$

$$\sin^2(\frac{\pi}{4} + \delta) = \left(\frac{\cos\delta}{\sqrt{2}} + \frac{\sin\delta}{\sqrt{2}}\right)^2$$

$$\therefore A = \frac{E^2}{2}(\cos\delta - \sin\delta)^2 \qquad B = \frac{E^2}{2}(\cos\delta + \sin\delta)^2$$

$$A = \frac{E^2}{2}(\cos^2\delta + \sin^2\delta - 2\cos\delta\sin\delta)$$

$$A = \frac{E^2}{2}(1 - 2\cos\delta\sin\delta)$$

$$A = \frac{E^2}{2}(1 - \sin 2\delta) \tag{2.3}$$

Similarly,

$$B = \frac{E^2}{2}(1 + \sin 2\delta) \tag{2.4}$$

Subtracting 2.4 from 2.3 we find

$$A - B = -E^2 \sin 2\delta$$

But δ is small so we can use the approximation $\sin\theta \simeq \theta$ for small θ.

$$\therefore A - B = -E^2 2\delta$$

Assuming that the entire cross section of each beam is captured by photo diodes PDA and PDB then the signal A-B is directly related to the optical power, P, of the probe beam [Eq. 2.5].

$$A - B = 2 < P_{Probe} > \delta \tag{2.5}$$

From [2.5] we can see that the strength of the difference signal is directly coupled to the optical power in the probe beam. The power of the probe beam is limited to remain non-invasive to the sample, which limits the strength of the signal being detected.

2.2 Mach-Zehnder Interferometer Detection

The Mach-Zehnder interferometer technique uses the interference of the local and signal beams to optically amplifies a TRFR signal. Therefore measurements can

be less invasive on the sample by reducing the transmitted power, while maintaining signal strength with an appropriate amount of amplification. Alternatively the optical amplification allows for the detection of weak Faraday Rotation signals at traditional probe power levels.

In this scheme (Fig. 2.2) the probe beam is divided with a polarizing beam splitter cube into two separate beams named the signal beam and local beam. The signal beam passes through the sample and its polarization axis is rotated via the Faraday effect.[18, 17] Afterwards the signal beam passes through a polarizer to remove the unrotated component. The polarizer in the local beam is there to maintain symmetry between the two arms of the interferometer as discussed in Chapter 3. The signal beam and local beam now have the same polarization axis and are recombined with a non-polarizing 50:50 beam splitter. The two outputs of the non-polarizing beam splitter are then detected by two photodiodes and the difference signal between the diodes is measured.

Now consider the electric fields of the local and signal beams before the non-polarizing beam splitter. In general

$$\vec{E}_{Signal} = \vec{E}_S = E_{Sx}\hat{x} + E_{Sy}\hat{y} \tag{2.6}$$

$$\vec{E}_{Local} = \vec{E}_L = (E_{Lx}\hat{x} + E_{Ly}\hat{y})e^{i\phi} \tag{2.7}$$

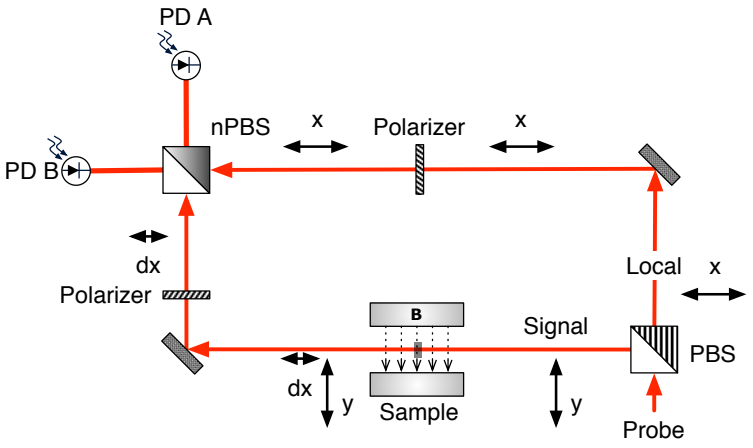

Figure 2.2: Conceptual diagram of a polarization sensitive Mach-Zehnder interferometer. PBS is a Polarizing Beam Splitter and nPBS is a 50:50 Non-Polarizing Beam Splitter.

Where ϕ represents a phase difference between the signal and local beams.

After passing through the non-polarizing beam splitter the electric fields at photodiodes PDA and PDB will be:

$$\vec{E}_A = (t_x E_{Sx}\hat{x} + t_y E_{Sy}\hat{y}) + (r_x E_{Lx}\hat{x} + r_y E_{Ly}\hat{y})e^{i(\phi+\frac{\pi}{2})} \tag{2.8}$$

$$\vec{E}_B = (r_x E_{Sx}\hat{x} + r_y E_{Sy}\hat{y})e^{i\frac{\pi}{2}} + (t_x E_{Lx}\hat{x} + t_y E_{Ly}\hat{y})e^{i\phi} \tag{2.9}$$

Where $r_{x/y}$ and $t_{x/y}$ are the Fresnel reflection and transmission coefficients for the polarization basis of the non-polarizing beam splitting cube. The $\frac{\pi}{2}$ phase change in $\vec{E}_A$ and $\vec{E}_B$ is due to the reflection on the interface of the cube.

Examine $\vec{E}_A$ [Eq. 2.8]

$$\vec{E}_A = (t_x E_{Sx} + r_x E_{Lx} e^{i(\phi+\frac{\pi}{2})})\hat{x} + (t_y E_{Sy} + r_y E_{Ly} e^{i(\phi+\frac{\pi}{2})})\hat{y}$$

$$\therefore |\vec{E}_A|^2 = E_A^2 = t_x^2 E_{Sx}^2 + r_x^2 E_{Lx}^2 + t_x E_{Sx} r_x^* E_{Lx}^* e^{-i(\frac{\pi}{2}+\phi)} + t_x^* E_{Sx}^* r_x E_{Lx} e^{i(\frac{\pi}{2}+\phi)}$$
$$+ t_y^2 E_{Sy}^2 + r_y^2 E_{Ly}^2 + t_y E_{Sy} r_y^* E_{Ly}^* e^{-i(\frac{\pi}{2}+\phi)} + t_y^* E_{Sy}^* r_y E_{Ly} e^{i(\frac{\pi}{2}+\phi)}$$

Now since we have already taken into account the phase change at the interface of the recombining cube the reflection and transmission coefficients are real. We have also taken into account the relative phase change between the electric field components with ϕ and therefore the electric field amplitudes are also real.

$$\therefore E_A^2 = t_x^2 E_{Sx}^2 + r_x^2 E_{Lx}^2 + t_x r_x E_{Sx} E_{Lx} (e^{i(\frac{\pi}{2}+\phi)} + e^{-i(\frac{\pi}{2}+\phi)})$$
$$+ t_y^2 E_{Sy}^2 + r_y^2 E_{Ly}^2 + t_y r_y E_{Sy} E_{Ly} (e^{i(\frac{\pi}{2}+\phi)} + e^{-i(\frac{\pi}{2}+\phi)})$$

Recall

$$\cos\theta = \frac{e^{i\theta} + e^{-i\theta}}{2} \tag{2.10}$$

$$\therefore E_A^2 = \left(t_x^2 E_{Sx}^2 + r_x^2 E_{Lx}^2 + 2 t_x r_x E_{Sx} E_{Lx} \cos(\tfrac{\pi}{2} + \phi) \right)$$
$$+ \left(t_y^2 E_{Sy}^2 + r_y^2 E_{Ly}^2 + 2 t_y r_y E_{Sy} E_{Ly} \cos(\tfrac{\pi}{2} + \phi) \right)$$

$$E_A^2 = (t_x^2 E_{Sx}^2 + r_x^2 E_{Lx}^2 - 2t_x r_x E_{Sx} E_{Lx} \sin\phi) + (t_y^2 E_{Sy}^2 + r_y^2 E_{Ly}^2 - 2t_y r_y E_{Sy} E_{Ly} \sin\phi) \tag{2.11}$$

Now examine $\vec{E}_B$ (Eq. 2.9)

$$\vec{E}_B = (r_x E_{Sx} e^{i\frac{\pi}{2}} + t_x E_{Lx} e^{i\phi})\hat{x} + (r_y E_{Sy} e^{i\frac{\pi}{2}} + t_y E_{Ly} e^{i\phi})\hat{y}$$

$$\therefore |\vec{E}_B|^2 = E_B^2 = r_x^2 E_{Sx}^2 + t_x^2 E_{Lx}^2 + t_x r_x E_{Sx} E_{Lx}(e^{i(\frac{\pi}{2}-\phi)} + e^{-i(\frac{\pi}{2}-\phi)})$$

$$+ r_y^2 E_{Sy}^2 + t_y^2 E_{Ly}^2 + t_y r_y E_{Sy} E_{Ly}(e^{i(\frac{\pi}{2}-\phi)} + e^{-i(\frac{\pi}{2}-\phi)})$$

Again using Eq. 2.10

$$E_B^2 = \left(r_x^2 E_{Sx}^2 + t_x^2 E_{Lx}^2 + 2t_x r_x E_{Sx} E_{Lx} \cos(\tfrac{\pi}{2} - \phi)\right)$$

$$+ \left(r_y^2 E_{Sy}^2 + t_y^2 E_{Ly}^2 + 2t_y r_y E_{Sy} E_{Ly} \cos(\tfrac{\pi}{2} - \phi)\right)$$

$$E_B^2 = (r_x^2 E_{Sx}^2 + t_x^2 E_{Lx}^2 + 2t_x r_x E_{Sx} E_{Lx} \sin\phi) + (r_y^2 E_{Sy}^2 + t_y^2 E_{Ly}^2 + 2t_y r_y E_{Sy} E_{Ly} \sin\phi) \tag{2.12}$$

Since we are measuring the beams we must consider the irradiance at photodiodes PDA and PDB.

$$A_{Irradiance} = A = < |\vec{S}_A| >$$

Where <> denotes the time average over $\vec{S_A}$, the Poynting vector for the beam at PDA.

$$\therefore A = \epsilon_0 c < E_A^2 >$$

Where ϵ_0 is the permittivity of free space and c is the speed of light. Similarly,

$$B = \epsilon_0 c < E_B^2 >$$

Thus the difference signal between the two photodiodes A and B is proportional to the difference between E_A^2 and E_B^2.

$$A - B = \epsilon_0 c \Big(< E_A^2 > - < E_B^2 > \Big) \tag{2.13}$$

Neglect the time average and physical constants for now.

$$A - B = E_A^2 - E_B^2$$

Now substitute Eq. 2.11 and 2.12.

$$A - B = (t_x^2 E_{Sx}^2 + r_x^2 E_{Lx}^2 - 2t_x r_x E_{Sx} E_{Lx} \sin\phi) + (t_y^2 E_{Sy}^2 + r_y^2 E_{Ly}^2 - 2t_y r_y E_{Sy} E_{Ly} \sin\phi)$$

$$-(r_x^2 E_{Sx}^2 + t_x^2 E_{Lx}^2 + 2t_x r_x E_{Sx} E_{Lx} \sin\phi) - (r_y^2 E_{Sy}^2 + t_y^2 E_{Ly}^2 + 2t_y r_y E_{Sy} E_{Ly} \sin\phi)$$

$$A - B = (t_x^2 - r_x^2)E_{Sx}^2 + (r_x^2 - t_x^2)E_{Lx}^2 + (t_y^2 - r_y^2)E_{Sy}^2 + (r_y^2 - t_y^2)E_{Ly}^2$$
$$-4t_x r_x E_{Sx} E_{Lx} \sin\phi - 4t_y r_y E_{Sy} E_{Ly} \sin\phi \tag{2.14}$$

For an ideal 50:50 beam splitter $|r_x| = |r_y| = |t_x| = |t_y| = \frac{1}{\sqrt{2}}$. Substituting into the previous equation the first four terms are zero.

$$A - B = -2(E_{Sx}E_{Lx} + E_{Sy}E_{Ly}) \sin\phi \tag{2.15}$$

From Eq. 2.15 we can see that the measured signal will depend on the product of the electric field components in the two arms of the interferometer and the phase difference ϕ.

Assuming that the polarizers in the interferometer (Fig. 2.2) are ideal then $E_{Sy} = E_{Ly} = 0$. The minus sign can be ignored since it has no bearing on the nature of the signal measured at the photodiodes.

$$A - B = 2E_{Sx}E_{Lx} \sin\phi$$

Or since the local arm is always polarized in the x-direction.

$$A - B = 2E_{Sx}E_{L} \sin\phi \tag{2.16}$$

Now that an equation for how the difference signal at photodiode PDA and PDB is related to the electric field components of the signal and local beams is established Faraday rotation of the signal beam can be considered. As shown in Fig. 2.2 before sample interaction the electric field of the signal beam is entirely in the $\hat{y}$ direction. Therefore

$$\vec{E}_S = E_{Sy}\hat{y} = E_S\hat{y}$$

After interaction with the sample the electric field direction is rotated slightly (typical experiments values are on the order of μrad to mrad rotations) around the propagation direction of the beam (Fig. 2.3) via the Faraday effect.

$$\therefore \vec{E}_S = E_S \sin\delta\hat{x} + E_S \cos\delta\hat{y}$$

For small rotations such that $\delta << 1$

$$\vec{E}_S = E_S\delta\hat{x} + E_S(1-\delta)\hat{y} \tag{2.17}$$

Substituting the $\hat{x}$ component of $\vec{E}_S$ back in Eq. 2.16

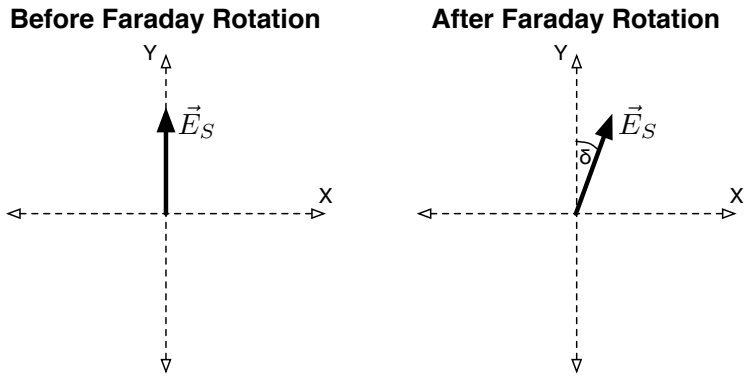

Figure 2.3: The electric field vector of the signal beam before and after Faraday rotation at the sample, where δ is the angle of rotation.

$$A - B = 2(E_S\delta)E_L \sin\phi$$

$$A - B = 2E_S E_L \delta \sin\phi \tag{2.18}$$

Assuming that the entire cross section of each beam is captured by photo diodes A and B then Eq. 2.18 can be rewritten in terms of the optical powers in the beams incident on photodiodes PD A and PD B.

$$A - B = 2\sqrt{< P_S >< P_L >}\delta \sin\phi \tag{2.19}$$

Where $< P_S >$ and $< P_L >$ are the time averaged, over a pulse cycle of the laser, optical powers in the signal and local beams.

Compare Eq.2.19 to Eq.2.5, the difference single for the optical bridge detection

scheme:

$$A - B = 2\sqrt{< P_S >< P_L >}\,\delta \sin\phi \qquad \text{(Interferometer)}$$

$$A - B = 2 < P_{Probe} > \delta \qquad \text{(Optical Bridge)}$$

Notice the optical gain factor, $< P_L >$, in the difference signal for the interferometer.

2.2.1 Accounting for Real World Limitations

In the above derivation for the difference signal between photodiodes PDA and PDB in the interferometer it was assumed that the optics in the interferometer performed ideally. Obviously the optics in the real interferometer will not perform ideally.

Imperfections in optics placement, optics shape, and other sources of error are all going to degrade the quality of the interference pattern. These types of imperfections should attenuate the signal measured at the photodiodes but will not affect the nature of the signal being measured. Two types of imperfections will have an affect on the nature of the measured signal [Eq. 2.19] and move it away from the ideal case that has already been analyzed. First, the non-polarizing beam splitting cube used to recombine the local and signal beams is not an ideal 50:50 beam splitter but does have a preference for transmitting/reflecting light polarized in a particular direction.

The polarizing optics used in the interferometer are not ideal either but instead have a finite extinction ratio, which introduces small, unwanted, polarization components in the signal and local arms.

Taking these two realities into consideration, means that $|r_x| = |r_y| = |t_x| = |t_y| = \frac{1}{\sqrt{2}}$ is not true since the beam splitter used for recombining the beam is not polarization independent. The finite extinction ratio of the polarizing optics also means that $E_{Sy} = E_{Ly} = 0$ as taken above is not true.

To analyze the effect of these imperfections the equations for the local and signal beams before beam recombination will be found. Then they will be substituted into Eq. 2.14 to determine the final form of the measured signal.

The extinction ratio is defined as the ratio of the optical power associated with the desired component and unwanted component of light transmitted through the optic. In the case of the polarizing beam splitter there are extinction ratios for both the transmitted and reflected components. The extinction ratios are related according to Eq. 2.20.

$$\text{Extinction Ratio} = ER = \frac{T_p}{T_s} = \frac{R_s}{R_p} \tag{2.20}$$

Before the PBS the electric field components of the probe beam can be written as:

$$\vec{E}_{Probe} = \vec{E}_P = E_{Px}\hat{x} + E_{Py}\hat{y}$$

Alternatively, the electric field of the probe beam can be represented in vector form:

$$\vec{E}_P = \begin{bmatrix} E_{Px} \\ \\ E_{Py} \end{bmatrix} \tag{2.21}$$

Now we can use a series of matrix operators on $\vec{E}_P$ to determine the form of the signal and local beams before they are recombined at the non-polarizing beam splitting cube.

The two matrix operators for handling either the transmission or reflection of the beam through a polarizer or polarizing beam splitting cube take the following form.

$$\mathbf{P}_R = \begin{bmatrix} r_x & 0 \\ \\ 0 & r_y \end{bmatrix} \qquad\qquad \mathbf{P}_T = \begin{bmatrix} t_x & 0 \\ \\ 0 & t_y \end{bmatrix} \tag{2.22}$$

Where $\mathbf{P}_R$ is the matrix for reflections and $\mathbf{P}_T$ is the matrix for transmission.

A matrix is also needed to describe the rotation of the polarization axis at the sample due to the Faraday Effect.

$$\mathbf{R}(\theta) = \begin{bmatrix} \cos\theta & -\sin\theta \\ \\ \sin\theta & \cos\theta \end{bmatrix} \tag{2.23}$$

It is impossible to ensure that all the optics are positioned so that all of the polarizing optics have the same polarization basis. Therefore the rotation of the

polarization basis between optics needs to be accounted for. A rotation in the basis by an amount θ is the same as a rotation of the vector in the original basis by an amount $-\theta$. Therefore

$$\mathbf{R}_{basis}(\theta) = \mathbf{R}(-\theta) \tag{2.24}$$

First consider the local beam and the matrix transformations that occur along the beam line. The probe beam $[\vec{E}_P]$ is transmitted through the polarizing beam splitter PBS1 $[\mathbf{P}_{T1}]$. Further down the local arm the beam is filtered by another polarizing beam splitter, PBS3, which will have a different polarization basis than PBS1 $[\mathbf{P}_{T3} \cdot \mathbf{R}_{PBS3}(\theta_{L2})]$. The beam is then recombined at the non-polarizing beam-splitter which has a different basis again $[\mathbf{R}_{nPBS}(\theta_{L3})]$. By taking the product of these factors, the form of the electric field before beam recombination can be calculated:

$$\vec{E}_L = \mathbf{R}_{nPBS}(\theta_{L3}) \cdot \mathbf{P}_{T3} \cdot \mathbf{R}_{PBS3}(\theta_{L2}) \cdot \mathbf{P}_{T1} \cdot \vec{E}_P \tag{2.25}$$

Note that θ_{L1} is not used so that the equations for the signal and local beam are similar. Also the basis of the first polarizing beam splitter, PBS1, is incorporated

into the factor for the probe beam [$\vec{E}_P$]:

$$\vec{E}_L = \begin{bmatrix} E_{Py} t_{y_1} (\cos\theta_{L3} \sin\theta_{L2} t_{x_3} + \cos\theta_{L2} \sin\theta_{L3} t_{y_3}) \\ E_{Py} t_{y_1} (\cos\theta_{L2} \cos\theta_{L3} t_{y_3} - \sin\theta_{L2} \sin\theta_{L3} t_{x_3}) \end{bmatrix} + \begin{bmatrix} E_{Px} t_{x_1} (\cos\theta_{L2} \cos\theta_{L3} t_{x_3} - \sin\theta_{L2} \sin\theta_{L3} t_{y_3}) \\ -E_{Px} t_{x_1} (\cos\theta_{L2} \sin\theta_{L3} t_{x_3} + \cos\theta_{L3} \sin\theta_{L2} t_{y_3}) \end{bmatrix}$$

Alternatively, the electric field in the local beam can be described using the extinction ratio of the two polarizers, PBS1 and PBS3, and their primary transmission coefficients, which are t_{x_1} and t_{x_3} respectively in this case.

Thus, substituting $t_{y_1} = \frac{t_{x_1}}{\sqrt{ER_1}}$ and $t_{y_3} = \frac{t_{x_3}}{\sqrt{ER_3}}$ into the previous equation:

$$\vec{E}_L = \begin{bmatrix} E_{Py} \frac{t_{x_1}}{\sqrt{ER_1}} t_{x_3} (\cos\theta_{L3} \sin\theta_{L2} + \cos\theta_{L2} \sin\theta_{L3} \frac{1}{\sqrt{ER_3}}) \\ E_{Py} \frac{t_{x_1}}{\sqrt{ER_1}} t_{x_3} (\cos\theta_{L2} \cos\theta_{L3} \frac{1}{\sqrt{ER_3}} - \sin\theta_{L2} \sin\theta_{L3}) \end{bmatrix} + \begin{bmatrix} E_{Px} t_{x_1} t_{x_3} (\cos\theta_{L2} \cos\theta_{L3} - \sin\theta_{L2} \sin\theta_{L3} \frac{1}{\sqrt{ER_3}}) \\ -E_{Px} t_{x_1} t_{x_3} (\cos\theta_{L2} \sin\theta_{L3} + \cos\theta_{L3} \sin\theta_{L2} \frac{1}{\sqrt{ER_3}}) \end{bmatrix} \tag{2.26}$$

(2.27)

The signal beam goes through similar transformations as the local beam [Eq.2.25]

with the addition of a term to account for the Faraday rotation at the sample [$\mathbf{R}(\theta_{S1})$]; where θ_{S1} is the rotation due to the Faraday effect.

The probe beam [$\vec{E}_P$] is reflected by the polarizing beam splitter PBS1 [$\mathbf{P}_{R1}$]. After PBS1, the beam is transmitted through the sample and the polarization axis is rotated slight via the Faraday effect [$\mathbf{R}(\theta_{S1})$]. Further down the signal arm the beam is filtered by another polarizing beam splitter, PBS2, which will have a different polarization basis than PBS1 [$\mathbf{P}_{T2} \cdot \mathbf{R}_{PBS2}(\theta_{S2})$]. The beam is then recombined at the non-polarizing beam-splitter which has a different basis again [$\mathbf{R}_{nPBS}(\theta_{S3})$]. By taking the product of these factors the form of the electric field before beam recombination can be calculated.

Therefore

$$\vec{E}_S = \mathbf{R}_{nPBS}(\theta_{S3}) \cdot \mathbf{P}_{T2} \cdot \mathbf{R}_{PBS2}(\theta_{S2}) \cdot \mathbf{R}(\theta_{S1}) \cdot \mathbf{P}_{R1} \cdot \vec{E}_P \tag{2.28}$$

Note that the basis of the first polarizing beam splitter, PBS1, is incorporated into the factor for the probe beam [$\vec{E}_P$].

After simplification

$$\vec{E}_S = \begin{bmatrix} E_{Py} r_{y_1} (t_{y_2} \sin\theta_{S3} \cos(\theta_{S1} - \theta_{S2}) - t_{x_2} \cos\theta_{S3} \sin(\theta_{S1} - \theta_{S2})) \\ E_{Py} r_{y_1} (t_{x_2} \sin\theta_{S3} \sin(\theta_{S1} - \theta_{S2}) + t_{y_2} \cos\theta_{S3} \cos(\theta_{S1} - \theta_{S2})) \end{bmatrix} + \begin{bmatrix} E_{Px} r_{x_1} (t_{x_2} \cos\theta_{S3} \cos(\theta_{S1} - \theta_{S2}) + t_{y_2} \sin\theta_{S3} \sin(\theta_{S1} - \theta_{S2})) \\ E_{Px} r_{x_1} (t_{y_2} \cos\theta_{S3} \sin(\theta_{S1} - \theta_{S2}) - t_{x_2} \sin\theta_{S3} \cos(\theta_{S1} - \theta_{S2})) \end{bmatrix}$$

Substituting for the extinction ratio of the polarizers using $r_{x_1} = \frac{r_{y_1}}{\sqrt{ER_1}}$ and $t_{y_2} = \frac{t_{x_2}}{\sqrt{ER_2}}$.

$$\vec{E}_S = \begin{bmatrix} E_{Py} r_{y_1} t_{x_2} \left(\frac{1}{\sqrt{ER_2}} \sin\theta_{S3} \cos(\theta_{S1} - \theta_{S2}) - \cos\theta_{S3} \sin(\theta_{S1} - \theta_{S2}) \right) \\ E_{Py} r_{y_1} t_{x_2} \left(\sin\theta_{S3} \sin(\theta_{S1} - \theta_{S2}) + \frac{1}{\sqrt{ER_2}} \cos\theta_{S3} \cos(\theta_{S1} - \theta_{S2}) \right) \end{bmatrix} + \begin{bmatrix} E_{Px} \frac{r_{y_1}}{\sqrt{ER_1}} t_{x_2} \left(\cos\theta_{S3} \cos(\theta_{S1} - \theta_{S2}) + \frac{1}{\sqrt{ER_2}} \sin\theta_{S3} \sin(\theta_{S1} - \theta_{S2}) \right) \\ E_{Px} \frac{r_{y_1}}{\sqrt{ER_1}} t_{x_2} \left(\frac{1}{\sqrt{ER_2}} \cos\theta_{S3} \sin(\theta_{S1} - \theta_{S2}) - \sin\theta_{S3} \cos(\theta_{S1} - \theta_{S2}) \right) \end{bmatrix} \quad (2.29)$$

It is clear that with substituting the components of the signal [Eq. 2.29] and local [Eq. 2.27] beams into Eq. 2.14, the expression for the measured signal will not be as simple as was described previously with Eq. 2.19.

Before substitution into the expression for the difference signal [Eq. 2.14], the expressions for $\vec{E}_L$ [Eq. 2.27] and $\vec{E}_S$ [Eq. 2.29] can be simplified slightly.

Both θ_{L2} and θ_{L3} are small because the difference in the polarization axes of the nPBS, PBS1, and PBS3 in the interferometer are on the order of a degree or two. Therefore Eq. 2.27 can be rewritten without trigonometric functions:

$$\vec{E}_L \cong \begin{bmatrix} E_{Py}\frac{t_{x_1}}{\sqrt{ER_1}}t_{x_3}((1-\theta_{L3})\theta_{L2}+(1-\theta_{L2})\theta_{L3}\frac{1}{\sqrt{ER_3}}) \\ E_{Py}\frac{t_{x_1}}{\sqrt{ER_1}}t_{x_3}((1-\theta_{L2})(1-\theta_{L3})\frac{1}{\sqrt{ER_3}}-\theta_{L2}\theta_{L3}) \end{bmatrix} + \begin{bmatrix} E_{Px}t_{x_1}t_{x_3}((1-\theta_{L2})(1-\theta_{L3})-\theta_{L2}\theta_{L3}\frac{1}{\sqrt{ER_3}}) \\ -E_{Px}t_{x_1}t_{x_3}((1-\theta_{L2})\theta_{L3}+(1-\theta_{L3})\theta_{L2}\frac{1}{\sqrt{ER_3}}) \end{bmatrix} \tag{2.30}$$

Similarly, θ_{S1} should be small since it is due to Faraday Rotation at the sample. The polarization axes of the PBS1, PBS2, and nPBS, while not all parallel, should be within a few degrees of separation and therefore θ_{S2} and θ_{S3} should also be small. Therefore $(\theta_{S1}-\theta_{S2})$ should also be small and therefore Eq. 2.29 can be approximated as a strictly algebraic equation:

$$\vec{E}_S \cong \begin{bmatrix} E_{Px}\frac{r_{y_1}}{\sqrt{ER_1}}t_{x_2}\left((1-\theta_{S3})(1-\theta_{S1}+\theta_{S2})+\frac{1}{\sqrt{ER_2}}\theta_{S3}(\theta_{S1}-\theta_{S2})\right) \\ E_{Py}r_{y_1}t_{x_2}\left(\frac{1}{\sqrt{ER_2}}(1-\theta_{S3})(1-\theta_{S1}+\theta_{S2})+\theta_{S3}(\theta_{S1}-\theta_{S2})\right) \end{bmatrix} + \begin{bmatrix} E_{Py}r_{y_1}t_{x_2}\left(\frac{1}{\sqrt{ER_2}}\theta_{S3}(1-\theta_{S1}+\theta_{S2})-(1-\theta_{S3})(\theta_{S1}-\theta_{S2})\right) \\ E_{Px}\frac{r_{y_1}}{\sqrt{ER_1}}t_{x_2}\left(\frac{1}{\sqrt{ER_2}}(1-\theta_{S3})(\theta_{S1}-\theta_{S2})-\theta_{S3}(1-\theta_{S1}+\theta_{S2})\right) \end{bmatrix} \tag{2.31}$$

Now the components of the local and signal beams from Eq. 2.30 and Eq. 2.31

respectively can be substituted into Eq. 2.14:

$$A - B = (t_{x_4}^2 - r_{x_4}^2)E_{Sx}^2 + (r_{x_4}^2 - t_{x_4}^2)E_{Lx}^2 + (t_{y_4}^2 - r_{y_4}^2)E_{Sy}^2 + (r_{y_4}^2 - t_{y_4}^2)E_{Ly}^2$$
$$- 4t_{x_4}r_{x_4}E_{Sx}E_{Lx}\sin\phi - 4t_{y_4}r_{y_4}E_{Sy}E_{Ly}\sin\phi$$

Where,

$$\begin{aligned}
E_{Sx} &= E_{Px}\frac{r_{y_1}}{\sqrt{ER_1}}t_{x_2}\left((1-\theta_{S3})(1-\theta_{S1}+\theta_{S2}) + \frac{1}{\sqrt{ER_2}}\theta_{S3}(\theta_{S1}-\theta_{S2})\right) \\
&\quad + E_{Py}r_{y_1}t_{x_2}\left(\frac{1}{\sqrt{ER_2}}\theta_{S3}(1-\theta_{S1}+\theta_{S2}) - (1-\theta_{S3})(\theta_{S1}-\theta_{S2})\right) \\
E_{Sy} &= E_{Py}r_{y_1}t_{x_2}\left(\frac{1}{\sqrt{ER_2}}(1-\theta_{S3})(1-\theta_{S1}+\theta_{S2}) + \theta_{S3}(\theta_{S1}-\theta_{S2})\right) \\
&\quad + E_{Px}\frac{r_{y_1}}{\sqrt{ER_1}}t_{x_2}\left(\frac{1}{\sqrt{ER_2}}(1-\theta_{S3})(\theta_{S1}-\theta_{S2}) - \theta_{S3}(1-\theta_{S1}+\theta_{S2})\right) \\
E_{Lx} &= E_{Py}\frac{t_{x_1}}{\sqrt{ER_1}}t_{x_3}\left((1-\theta_{L3})\theta_{L2} + (1-\theta_{L2})\theta_{L3}\frac{1}{\sqrt{ER_3}}\right) \\
&\quad + E_{Px}t_{x_1}t_{x_3}\left((1-\theta_{L2})(1-\theta_{L3}) - \theta_{L2}\theta_{L3}\frac{1}{\sqrt{ER_3}}\right) \\
E_{Ly} &= E_{Py}\frac{t_{x_1}}{\sqrt{ER_1}}t_{x_3}\left((1-\theta_{L2})(1-\theta_{L3})\frac{1}{\sqrt{ER_3}} - \theta_{L2}\theta_{L3}\right) \\
&\quad - E_{Px}t_{x_1}t_{x_3}\left((1-\theta_{L2})\theta_{L3} + (1-\theta_{L3})\theta_{L2}\frac{1}{\sqrt{ER_3}}\right)
\end{aligned} \tag{2.32}$$

To get a better sense of how the ideal signal is modified consider the imperfections in the interferometer separately.

Non-ideal 50:50 nPBS

Previously it was assumed that the non-polarizing beam splitting cube used to recombine the local and signal beam was a perfect 50:50 beam splitter: $|r_{x_4}| = |r_{y_4}| = |t_{x_4}| = |t_{y_4}| = \frac{1}{\sqrt{2}}$.

However, the beam splitter used in the interferometer is only an approximation of a ideal 50:50 beam splitter. Therefore a DC component, one that is not related to the phase difference between the two arms of the interferometer will be introduced into difference signal between the photodiodes. Consider a non-ideal 50:50 beam splitter separate from the other imperfections incorporated into the model above [Eq. 2.32]. Therefore disregard contributions from misaligned polarization axis and the finite extinction ratio of the polarizers:

$$\theta_{S2}, \theta_{S3}, \theta_{L2}, \theta_{L3} \rightarrow \quad 0$$

$$ER_1, ER_2, ER_3 \rightarrow \quad \infty$$

Thus

$$E_{Sx} = -E_{Py} r_{y_1} t_{x_2} \theta_{S1} \qquad E_{Lx} = E_{Px} t_{x_1} t_{x_3}$$

$$E_{Sy} = 0 \qquad E_{Ly} = 0$$

$$\begin{aligned}\therefore A - B &= (t_{x_4}^2 - r_{x_4}^2)E_{Sx}^2 + (r_{x_4}^2 - t_{x_4}^2)E_{Lx}^2 - 4t_{x_4}r_{x_4}E_{Sx}E_{Lx}\sin\phi \\ &= (t_{x_4}^2 - r_{x_4}^2)t_{x_2}^2 r_{y_1}^2 E_{Py}^2\theta_{S1}^2 + (r_{x_4}^2 - t_{x_4}^2)t_{x_1}^2 t_{x_3}^2 E_{Px}^2 \\ &+ 4t_{x_4}r_{x_4}(t_{x_2}r_{y_1}E_{Py})(t_{x_1}t_{x_3}E_{Px})\theta_{S1}\sin\phi \end{aligned} \tag{2.33}$$

Since $t_{x_4} \neq r_{x_4}$ two additional DC terms (terms which do not depend on the phase difference ϕ) appear in the difference signal of the photodiodes. As the mismatch between the reflection and transmission coefficient of the nPBS increases there will be a larger DC component in the measured difference signal.

Misalignment of the Polarization Optics

Aligning the polarization optics in the interferometer so that each of their basis are parallel is not possible. Consider the affect this has on the difference signal independent of the other imperfections:

$$\begin{aligned} ER_1, ER_2, ER_3 &\rightarrow \infty \\ |r_{x_4}| = |r_{y_4}| = |t_{x_4}| = |t_{y_4}| &= \frac{1}{\sqrt{2}} \end{aligned}$$

and Eq. 2.32 becomes

$$\therefore A - B = -2E_{Sx}E_{Lx}\sin\phi - 2E_{Sy}E_{Ly}\sin\phi$$

$$E_{Sx} = -E_{Py}r_{y_1}t_{x_2}(1-\theta_{S3})(\theta_{S1}-\theta_{S2})$$

$$E_{Sy} = E_{Py}r_{y_1}t_{x_2}\theta_{S3}(\theta_{S1}-\theta_{S2})$$

$$E_{Lx} = E_{Px}t_{x_1}t_{x_3}(1-\theta_{L2})(1-\theta_{L3})$$

$$E_{Ly} = -E_{Px}t_{x_1}t_{x_3}(1-\theta_{L2})\theta_{L3}$$

$$\therefore A - B = 2\left(E_{Py}r_{y_1}t_{x_2}(1-\theta_{S3})\left(\theta_{S1}-\theta_{S2}\right)\right)\left(E_{Px}t_{x_1}t_{x_3}(1-\theta_{L2})(1-\theta_{L3})\right)\sin\phi$$

$$+ 2\left(E_{Py}r_{y_1}t_{x_2}\theta_{S3}(\theta_{S1}-\theta_{S2})\right)\left(E_{Px}t_{x_1}t_{x_3}(1-\theta_{L2})\theta_{L3}\right)\sin\phi$$

Rewrite the equation with the following substitutions.

$$A - B = Z(1-\theta_{S3})(Y(1-\theta_{L3}))\sin\phi + Z\theta_{S3}(Y\theta_{L3})\sin\phi$$

Where

$$Z = 2r_{y_1}t_{x_2}(\theta_{S1}-\theta_{S2})E_{Py}$$

$$Y = t_{x_1}t_{x_3}(1-\theta_{L2})E_{Px}$$

Therefore

$$A - B = ZY \sin\phi(1 - \theta_{S3})(1 - \theta_{L3}) + ZY \sin\phi(\theta_{S3}\theta_{L3})$$

$$A - B = ZY \sin\phi(1 + 2\theta_{S3}\theta_{L3} - \theta_{S3} - \theta_{L3}) \tag{2.34}$$

The form of this equation looks similar to Eq.2.19 but with an extra factor.

Consider the terms inside the brackets in Eq.2.34. It is expected that $\theta_{S3} \approx \theta_{L3}$ and are on the order of 1 degree, thus $\theta_{S3} << 1$ and $\theta_{L3} << 1$. Since these angles represent the misalignment of the nPBS with respect to the polarization basis of the signal and local arms, $\theta_{S3}\theta_{L3}$ in Eq. 2.34 is a second-order term and will be dominated by the first-order terms $-\theta_{S3}$ and $-\theta_{L3}$. Thus the misalignment of the nPBS will reduce the strength of the measured signal.

Expand $ZY \sin\phi$ in Eq. 2.34:

$$ZY \sin\phi = (2r_{y_1}t_{x_2}(\theta_{S1} - \theta_{S2})E_{Py})(t_{x_1}t_{x_3}(1 - \theta_{L2})E_{Px}) \sin\phi \tag{2.35}$$

The form of Eq. 2.35 is similar to Eq. 2.19 developed for the ideal case only attenuated by the fresnel coefficients. The misalignment of the PBS3 used in the local beam will further attenuate the signal through the factor $(1 - \theta_{L2})$. Recall that θ_{S2} is rotation of the polarization basis due to the polarizer PBS2, and should therefore be on the order of one degree. Now since $\theta_{S2} >> \theta_{S1}$ the factor $(\theta_{S1} - \theta_{S2})$

will introduce a small DC offset in the difference signal.

In conclusion the misalignment of the polarization bases of the optics used in the interferometer work to attenuate the signal, and create a small offset in the measured difference signal.

Extinction Ratio

The extinction ratio of the polarizing optics used in the interferometer is finite. Thus unwanted polarization components of the beam will be transmitted through each of the polarizing optics in the beam path: PBS1, PBS2, PBS3. To consider the affect these unwanted components have on the difference signal neglect the affect of misaligned basis and assume that the nPBS is a perfect 50:50 beam splitter.

$$\theta_{S2}, \theta_{S3}, \theta_{L2}, \theta_{L3} \rightarrow 0$$

$$|r_{x_4}| = |r_{y_4}| = |t_{x_4}| = |t_{y_4}| = \frac{1}{\sqrt{2}}$$

Therefore Eq. 2.32 becomes

$$
\begin{aligned}
A - B &= -2E_{Sx}E_{Lx}\sin\phi - 2E_{Sy}E_{Ly}\sin\phi \\
E_{Sx} &= E_{Px}r_{y_1}t_{x_2}\left(\frac{1}{\sqrt{ER_1}}\right)(1-\theta_{S1}) - E_{Py}r_{y_1}t_{x_2}\theta_{S1} \\
E_{Sy} &= E_{Py}r_{y_1}t_{x_2}\left(\frac{1}{\sqrt{ER_2}}\right)(1-\theta_{S1}) + E_{Px}r_{y_1}t_{x_2}\left(\frac{1}{\sqrt{ER_1\cdot ER_2}}\right)\theta_{S1} \\
E_{Lx} &= E_{Px}t_{x_1}t_{x_3} \\
E_{Ly} &= E_{Py}t_{x_1}t_{x_3}\frac{1}{\sqrt{ER_1\cdot ER_3}}
\end{aligned}
$$

Note that all the extra terms in the electric fields of the signal and local beams are reduced by the extinction ratio of the contributing polarizer.

After substitution and some simplification

$$
\begin{aligned}
A - B = {} & 2(r_{y_1}t_{x_1}t_{x_2}t_{x_3})E_{Py}E_{Px}\theta_{S1}\sin\phi \\
& - 2(r_{y_1}t_{x_1}t_{x_2}t_{x_3})\left(\frac{E_{Px}^2}{\sqrt{ER_1}}(1-\theta_{S1})\right)\sin\phi \\
& - 2(r_{y_1}t_{x_1}t_{x_2}t_{x_3})\left(\frac{E_{Py}^2}{\sqrt{ER_1\cdot ER_2\cdot ER_3}}(1-\theta_{S1})\right)\sin\phi \\
& - 2(r_{y_1}t_{x_1}t_{x_2}t_{x_3})\left(\frac{E_{Px}E_{Py}}{ER_1\sqrt{ER_2\cdot ER_3}}\theta_{S1}\right)\sin\phi
\end{aligned}
\tag{2.36}
$$

The first term in Eq. 2.36 is the original difference signal found in Eq. 2.16. The other three terms subtract from the original signal by a small amount that is governed

by the size of the extinction ratio. The larger the extinction ratio of the polarizers used in the interferometer, the smaller this effect will be.

2.2.2 Prioritizing Interferometer Improvements

Now that the relevant equations for the imperfections (non-ideal 50:50 nPBS, polarization axis misalignment, and finite extinction ratios) in the interferometer have been developed the relevance of each of these effects on the measured signal can be determined. Simply substituting typical values for the variables in equations 2.33, 2.34, and 2.36 will provide an estimate as to the importance of each of these effects.

The same type of optic was used for both PBS1, PBS2, and PBS3. Consulting the Appendix (§B) reveals that $t_{x_{1,2,3}} \approx \sqrt{0.9 = 0.949}$ and $r_{y_1} \approx \sqrt{0.995} = 0.997$. The extinction ratio for these optics is typically around 1000:1, and therefore $ER_{1,2,3} = 1000$. There are no absolute values given for the reflectance and transmittance of the nPBS, but taking values from a different supplier we can estimate that $t_{x_4} = r_{y_4}\sqrt{0.5} = 0.707$, and $t_{y_4} = r_{x_4} = \sqrt{0.4} = 0.632$ where the greatest difference between these values has been assumed. Misalignment between the polarization axes of the optics is small ($\approx 2^\circ$), so $\theta_{L2,L3} \simeq \theta_{S2,S3} \simeq 0.0349$ rad. In our experiments the interferometer is stabilized so that $\sin\phi \simeq 1$.

Taking a beam radius of 4 mm, and therefore an area of $0.5cm^2$, the electric field for E_{P_x} and E_{P_y} can calculated from the beam power. Consider a situation were both

arms of the interferometer have a power of 1 mW. Thus $E_{P_x} = E_{P_y} = 122.4N/C$.

Substitution of these values reveals the following:

Ideal:	Eq.2.14	25527.1δ N/C
nPBS:	Eq.2.33	$1342.03\delta^2 + 22832.1\delta - 1213.89$ N/C
Misalignment:	Eq.2.34	$22976.6\delta - 801.883$ N/C
Extinction Ratio:	Eq.2.36	$26335.1\delta - 808.044$ N/C

Where the Fresnel coefficients along the beam line have been incorporated into the calculation for Eq.2.14.

There are some changes if we consider the case were the local beam power is increased to 2 mW, and the signal arm remains at 1 mW. Therefore $E_{P_x} = 173.1N/C$ and $E_{P_y} = 122.4N/C$.

Ideal:	Eq.2.14	36100.7δ N/C
nPBS:	Eq.2.33	$1342.03\delta^2 + 32289.5\delta - 2427.79$ N/C
Misalignment:	Eq.2.34	$32493.8\delta - 1134.03$ N/C
Extinction Ratio:	Eq.2.36	$37716\delta - 1615.28$ N/C

The above equations are plotted in Fig.2.4. Clearly imperfections in the nPBS are

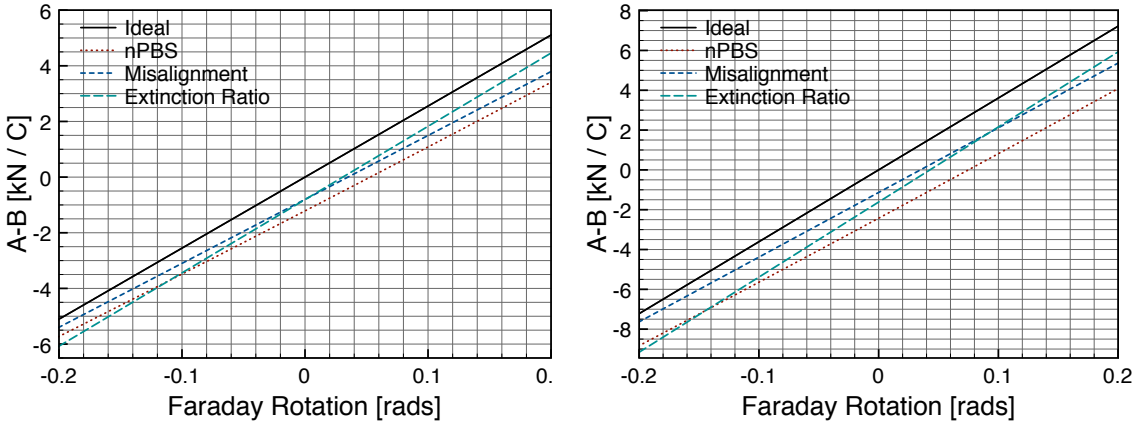

Figure 2.4: Plots demonstrating how the difference signal (A-B) changes with the amount of Faraday rotation using equations 2.33, 2.34, and 2.36 and the substituted values described above. (a) Power in signal arm and local arm equal to 1 mW. (b) Power in signal arm equal to 1 mW, and power in local arm equal to 2 mW.

dominant at small Faraday rotations, but both polarization axis misalignment and poor extinction ratios cause comparable errors in the difference signal.

Improving the misalignment between the polarization axis of the optics in the interferometer is a daunting task. However improving the nPBS and extinction ratios only requires replacing the existing optics with ones of higher-quality, thus these areas should be the focus of future improvements.

2.3 Experimental Setup and Parameters

The derivation of the interferometer's difference signal [Eq.2.19] ignored the envelope of the laser pulses. This was done to simplify the derivation and make it easier to

understand. However the pulse envelope will play an important role in the setup, design and operation of the interferometer.

During the derivation (§2.2) it was implied that we were dealing with a continuous signal with an electric field oscillating in space and time [Eq.2.37].

$$\vec{E}(t,\vec{x}) = \vec{E}\sin(\omega t - \vec{k}\cdot\vec{x}) \tag{2.37}$$

Ignoring the variation with position, the pulse envelope will change the electric field by adding a time-dependent factor [Eq.2.38].

$$\vec{E}(t) = \vec{E}\sec\left(\frac{\tau t}{FWHM}\right)\sin\omega t \tag{2.38}$$

Where τ is a constant dependent on the laser cavity that generates the pulse, and $FWHM$ is the full-width half-maximum of the pulse in temporal units.

The pulse envelope will modify the difference signal of the interferometer [Eq.2.39].

$$A - B = 2\sqrt{< P_S >< P_L >}\delta\sec^2\left(\frac{\phi}{\Delta}\right)\cos\phi \tag{2.39}$$

Where $\Delta = 2\pi cFWHM/\tau\lambda$ and it has been assumed that when ϕ is zero the two pulses are perfectly overlapped (note: that $\sin\phi$ had been changed to $\cos\phi$ so that the phase change is consistent between both terms). Note that Eq.2.39 ignores

spectral variations in the response of the photodiodes. Since the laser pulses are relatively narrow (full-width half-max spectral width of 14) the spectral variation of the photodiode response can be safely ignored.

For small variations in the phase, on the order of several wavelengths, the envelop function is approximately unity and constant.

When the phase ϕ is swept over the entire pulse-width an autocorrelation trace of the laser pulse is measured at the photodiodes which allows us to easily measure the pulse-width.

The amplitude of the difference signal will be affected by the quality of the overlap of the two beams. Typically the quality of an interference signal is characterized by a quantity called the visibility: the ratio between the difference of the maximum and minimum power in the interference pattern and their sum [Eq.2.40].

$$Visibility = \frac{P_{Max} - P_{Min}}{P_{Max} + P_{Min}} \tag{2.40}$$

In the interferometer the photodiodes are used to detect the interference. The difference between the two photodiodes is a bipolar voltage signal. Bipolar values will not work with the visibility as it has been defined. So instead of using the visibility

Channel	**Signal Arm / V**	**Local Arm / V**	**Both / V**
A	2.19	1.82	4.00
B	-1.60	-2.45	-4.16
A-B	-0.410	0.827	0.347

Table 2.1: Experimental data taken on October 13, 2006. The signal and local beams were at powers of 756 μW and 764 μW respectively.

the quality of the beam overlap (interference) is characterized by χ [Eq.2.41].

$$\chi = \frac{\text{Measured Autocorrelation Trace Height}}{\text{Expected Autocorrelation Trace Height}} \tag{2.41}$$

To calculate the expected autocorrelation trace height each photodiode and their difference is measured outside of the interference pattern (large ϕ) with just the local arm (signal arm blocked), then just the signal arm (local arm blocked) and then both (neither blocked). The expected values for the maximum and minimum trace heights at each diode can be calculated using Eq.2.11 and Eq.2.12. For example consider the following experimental data.

Measured Trace Height = 13.2 Vpp

$$\begin{aligned} A_{Max/Min} &= A_{Signal} + A_{Local} \pm 2\sqrt{A_{Signal}A_{Local}} \\ &= 8.01V/0.01V \\ A_{Trace} &= A_{Max} - A_{Min} \\ &= 8.00V \\ B_{Max/Min} &= B_{Signal} + B_{Local} \pm 2\sqrt{B_{Signal}B_{Local}} \\ &= -0.09V/-8.01V \\ B_{Trace} &= B_{Max} - B_{Min} \\ &= 7.92V \\ \text{Expected Trace Height} &= A_{Trace} + B_{Trace} \\ &= 15.9V \end{aligned}$$

The expected trace value thus assumes that all the power available contributes directly to the interference pattern. In reality some of the power will contribute to the various errors discussed in the previous section (§2.2.1).

Taking these two values the overlap quality can be calculated.

$$\chi = \frac{13.2V}{15.9V} = 0.830$$

This is typical value for the χ. When the interferometer is properly aligned values of χ between 0.7 and 0.9 should be achievable.

Chapter 3

Interferometer Design and Description

Mach-Zehnder interferometers are common tools for scientific analysis. In principle building such an interferometer is a simple task but several issues must be considered during design in order that the beams in the two arms of the interferometer, named the signal and local arms, can be overlapped upon recombination to produce the desired interference pattern. During the assembly of the polarization interferometer four main issues affected the quality of the beam recombination or stability of the interference pattern: recombination and beam overlap, wavefront distortions and dispersion, environmental isolation, and computer stabilization.

A schematic of the polarization sensitive interferometer is provided in Fig.3.1 to

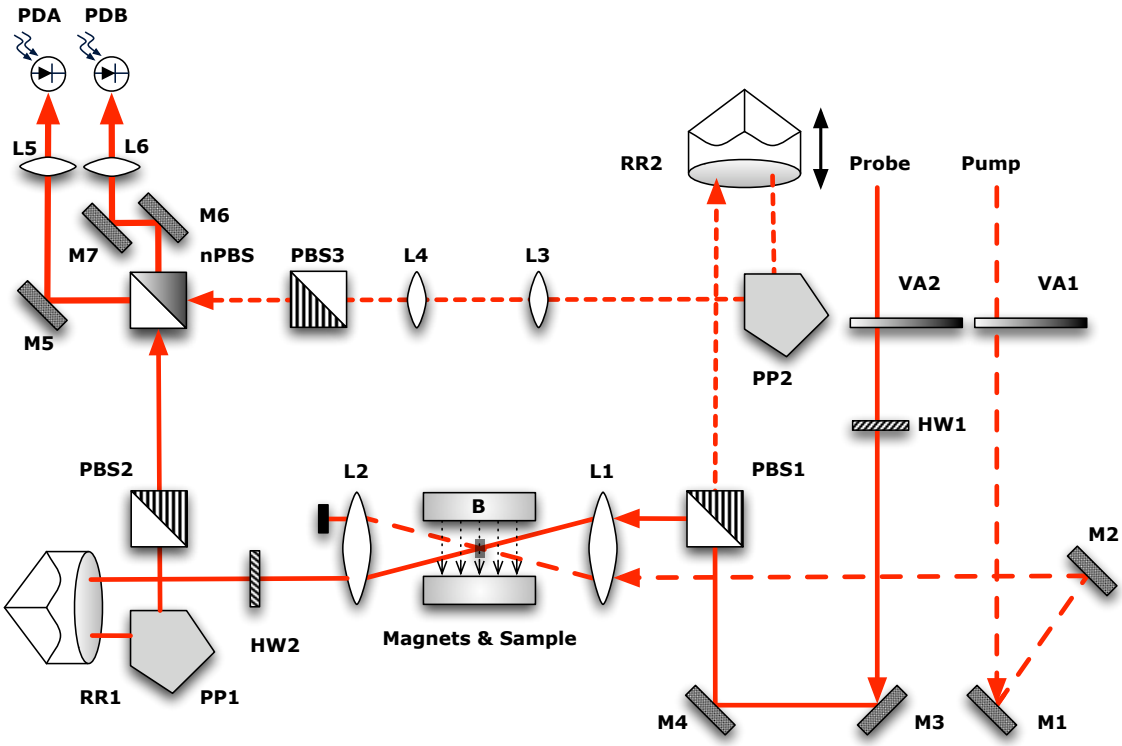

Figure 3.1: The signal arm of the interferometer is indicated by a solid beam, whereas the local arm beam path is traced by a dotted line. Lens pairs L1 and L2, as well as L3 and L4 are matched and form 1x beam collimators. VA = Variable Attenuator. HW = Half wave plate. M = Mirror. L = Lens. PP = Penta Prism. RR = Retroreflector. PBS = Polarizing Beamsplitting Cube. nPBS = non-Polarizing Beamsplitting Cube. PD = Photodiode. Further specification found in Appendix B.

serve as a reference for this chapter.

3.1 Recombination / Beam Overlap

In order to recombine the beam at the non-polarizing cube the local and signal beams must meet perpendicular to each other. Deviations away from a perpendicular cross-

ing of the local and signal arm will make it impossible to achieve complete overlap of the two beams after the recombination cube. When the beams are not completely overlapped, interference fringes will appear in the interference pattern. With complete overlap the interference pattern encompasses the entire beam waist (see Appendix A Fig.A.2). The interferometer will still function if the beams are not perfectly overlapped but the quality of the beam overlap directly affects the sensitivity of the interferometer to Faraday rotation in the signal arm by introducing an attenuating factor (¡1) to Eq.2.19. Therefore optimal overlap of the two beams is desired.

Typical schematics of a basic Mach-Zehnder interferometer show the two arms being directed with mirrors at the corners (Fig.3.2). In practice the use of mirrors for precise overlap of the two beams on the recombining cube is a difficult task that requires micrometer positioning of the tilt controls on the mirror mounts. The quality of the overlap is extremely sensitive to any deviations towards an acute or obtuse meeting of the two arms. The rotation controls on the recombining cube exacerbate the alignment of the interferometer with corner steering mirrors. Combined with the two degrees of freedom for tilting the signal and local arms with the corner mirrors there are a total of seven independent parameters to adjust and finely tune to achieve precise overlap (two on each mirror, three on the recombination cube). It is also difficult to know which control should be adjusted resulting in a lot of trial and error without a clear path towards proper alignment. The alignment procedure is therefore

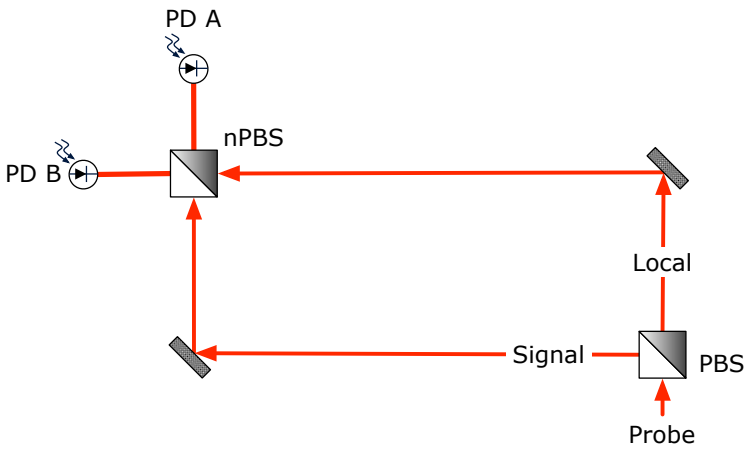

Figure 3.2: Schematic diagram of a basic Mach Zehnder interferometer. PBS = Polarizing Beam Splitting cube. nPBS = non-Polarizing Beam Splitting cube.

tedious, laborious and imprecise.

To avoid the problems associated with using corner mirrors to steer the two arms penta-prisms are used instead. Penta-prisms are special optics that are able to reflect an incoming beam at precisely 90 degrees regardless of the angle of incidence on the optic. The glass penta-prisms used in the assembly of the presented interferometer reflect the beam at 90 degrees with a maximum deviation of 30 arc seconds due to manufacturing imperfections (Appendix B). Optics with greater precision can be purchased for an appropriate increase in expense, however the performance of the penta-prisms used here has been satisfactory.

The degree to which the inclusion of the penta-prisms ease the alignment of the interferometer cannot be over-stressed. Instead of three-degrees of freedom in the horizontal plane when using mirrors there is now only one: the rotation of the cube.

Optimization of the beam overlap with the penta-prisms is, therefore, not a highly involved process. Every nine to twelve months laser or lab maintenance has to be performed which deviates the pointing of the laser slightly. These small deviations typically require complete alignment of the optics along the beam-path, including the interferometer. These periodic re-alignments further enhance the utility of the penta-prisms in easing the interferometer's alignment.

Proper alignment of the interferometer must also take into account imperfections in the optics. The glass cubes used to split, filter, and recombine the beam in the interferometer are imperfectly shaped and therefore cause unpredictable deviations of the beam. Fortunately the cubes can be arranged (rotated, flipped) so that the deviations add so that they do not severely impact the visibility of the interference. Proper positioning of the cubes can produce an order of magnitude difference in the peak-to-peak magnitude of the interference fringes measured at the photodiodes; care should be taken to optimize their placement.

3.2 Wavefront Distortions and Dispersion

Matching the wavefronts of the two beams after they are recombined is essential to achieve strong visibility of the interference pattern. If the wavefronts are not appropriately matched (ie. one wavefront is the mirror of the other) it is still possible to get a interference pattern, but the visibility will be quite poor. To match the

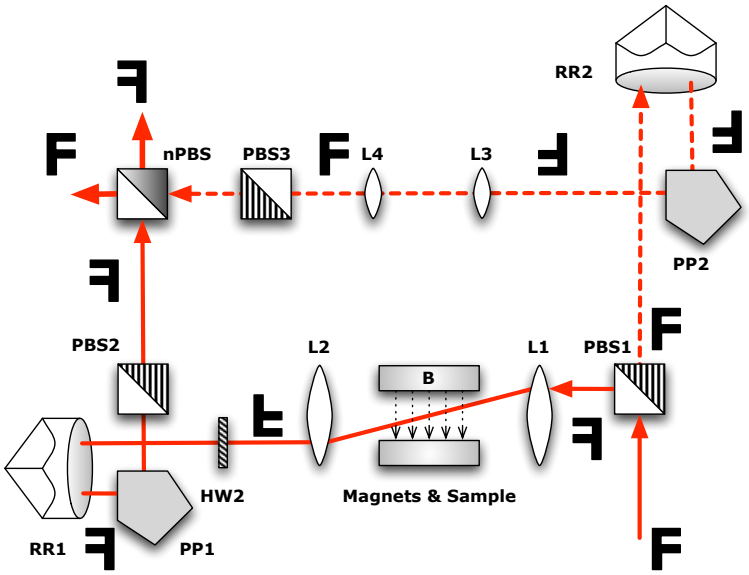

Figure 3.3: The image "F" is used to demonstrate the wavefront transformations that both the signal and local beams undergo while traversing their respective arms. Each image is shown as if the observer were looking down the beam line towards the image plane.

wavefronts properly it is critical that the two arms of the interferometer be symmetric; any transformations of the wavefront (flipping, mirroring, etc) must occur in each of the arms for the wavefronts to overlap properly after recombination.

The diagram shown in Fig.3.3 demonstrates the wavefront transformations that occur as the beams traverse the arms of the interferometer.

The collimator made from lenses L3 and L4 in the local arm is used only to match the transformations undergone in the signal arm by focusing the beam through the sample with lenses L1 and L2. Similarly, a retroreflector is placed in each arm so that the beam transformations are matched.

It is also important that the lenses used for the two collimators consist of a matched pair: both lenses in the pair should be the same size and make. If the lenses are of different diameters the wavefront will travel through different path lengths along its profile. The inhomogeneity in the delay of the wavefront will degrade the visibility of the interference pattern. Variations of $90\mu m$ (the length of one laser pulse) in the optical path length traveled across the wavefront will be enough to eliminate interference in some sections of the wavefront and severely degrade the visibility of the interference pattern.

Pulse dispersion also has a significant impact on the visibility of the interference pattern. If one arm contains dispersive optics that are absent in the other arm visibility will dramatically decrease. In an attempt to reduce expenses the interferometer originally used a one inch, hollow retroreflector in the signal arm for RR1, and a two inch, glass retroreflector in the local arm for RR2. Although the optical path lengths of the two arms could be equalized with appropriate positioning of the retroreflectors the differences in the pulse dispersion between the two arms degraded the visibility of the interference pattern significantly. Replacing the glass retroreflector with another hollow retroreflector increased the interference quality from $\chi = 0.02$ to $\chi = 0.8$ [Eq.2.41], which is a significant increase.

The polarizing beam splitter in the local arm, PBS3, was added to the interferometer precisely to compensate for dispersive effects that degraded the visibility of the

interference. Without the PBS3 present in the local arm there is an decrease between one to two orders of magnitude in the peak-to-peak amplitude of the interference fringes measured at the photodiodes.

3.3 Environmental Isolation

The interference of the two beams is sensitive to fluctuations in the optical path length of the two arms on length scales of the optical wavelength ($\sim$ 870 nm). Atmospheric turbulence, acoustic vibrations, thermal fluctuations, and mechanical vibrations all degrade the quality of the overlap by introducing unwanted phase noise. Care must be taken to reduce these sources of error whenever possible.

Care is taken to avoid placing heat sources near the interferometer. For example, incandescent reading lamps are placed away from the interferometer since they will heat the surface of the optics table and cause a measurable displacement ($\sim \mu$m) of the optics within the interferometer. Experiments are performed after sufficient time, approximately one to two hours, has been given for the laser and electrical equipment to reach a thermal steady state.

Thermal stability in the lab is maintained by an air conditioning unit that keeps the ambient temperature in the room stable to within one degree Celsius. Unfortunately, use of the air conditioning unit contributes significantly to air turbulence on the surface of the optical table as cold air is blown from the roof vents.

Air is not an ideal environment in which to operate an interferometer since it can act as a medium for vibrations and turbulence. To eliminate air turbulence over the interferometer the interferometer is entirely enclosed with a box made of particle board. Acoustical dampening foam (Appendix C) lines the inside walls and ceiling of the box to reduce acoustical vibrations within the interferometer. The walls were built to be a three quarters of an inch thick to help further dampen acoustical noise, and create a sturdy frame. A glass window is installed in one of the panels of the box to allow laser light into the interferometer. Although the box is not air tight, acoustical foam covers all the seams in the box to nearly eliminate air flow. The box also reduces stray light sources being detected by the photodiodes. Details of the box design can be found in Appendix C.

Characterization of the dampening effect the box has on acoustical vibrations was performed by measuring the drift of the difference signal over a long period of time with a lock-in amplifier (Fig.3.4). After 80 minutes the lid of the box was removed and caused a remarkable increase in the signal noise on both the magnitude and phase channels of the lock-in amplifier.

By passing the magnitude signal through a low-pass filter and using the filtered output as a fit we calculated the signal-to-noise ratio ($10 \log \frac{measured}{fit}$) of the magnitude signal before and after the lid of the acoustical dampening box was removed. With the lid on we calculated a signal-to-noise ratio of 35.1 dB, whereas when the lid was

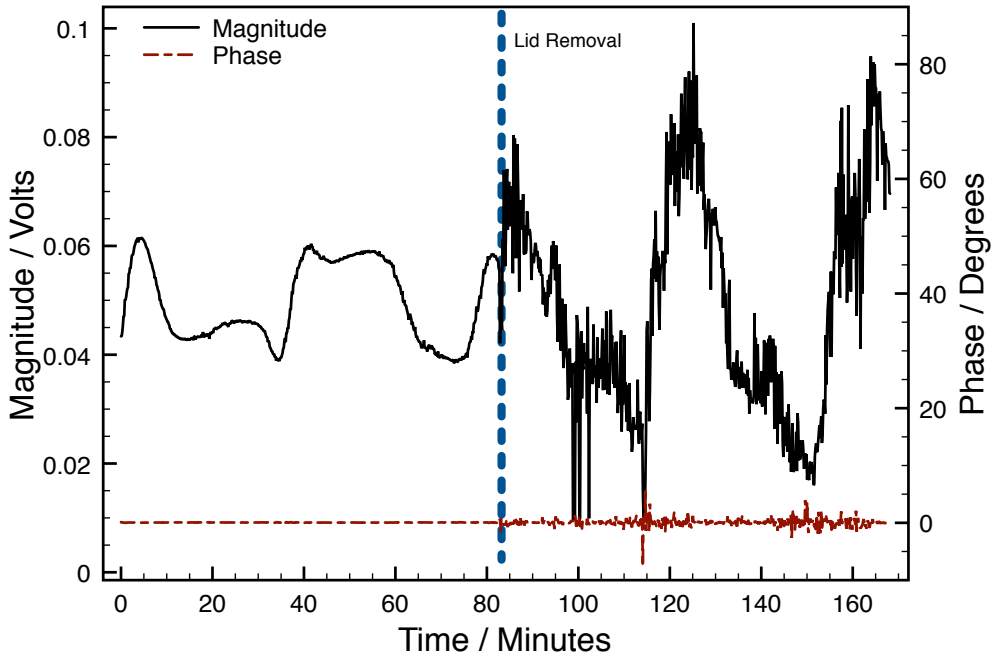

Figure 3.4: Lock-in measurement of the difference signal over time. Around 80 minutes the lid of the box is removed. Notice the dramatic increase in the signal noise present in both the magnitude and phase of the lock-in measurement after the lid is removed.

removed the noise increased dramatically to produce a signal to noise ratio of 18.2 dB. Also, the standard deviation of the noise distribution in the phase channel increased significantly from 0.0251 degrees with the lid on, to 2.41 degrees with the lid removed.

These results effectively demonstrate the performance of the acoustical dampening box and the importance that environmental isolation has in reducing unwanted vibrations (signal noise) within the interferometer.

While measurements are being taken, the optics table (Newport RS 4000) is floated on mechanical isolators (Newport I-2000) that act as low pass filters for mechanical

vibrations passing from the floor onto the table. With resonant frequencies around 1 Hz the isolators effectively dampen vibrations down to very-low frequencies. The optics table is also designed to be rigid surface for optical mounting. Vibrations on the table surface are dampened so that they do not cause unwanted spatial displacement between mounted optical components.

What should be clear is that there is no single solution to eliminate environmental noise within the interferometer. Several precautions have to be taken, each serving to reduce sources of noise.

3.4 Computer Stabilization

The efforts made to reduce perturbations to the optical path length of the two arms of the interferometer in the above section effectively attenuate high-frequency mechanical vibrations. However, thermal fluctuations still cause optical path length changes between the signal and local arms (changes in ϕ in Eq.2.19) that result in ultra-low frequency drifts in the measured signal. These drifts degrade the quality of the measured signal as the overlap of the two beams at the photodiodes moves from constructive to destructive interference over a period of several minutes. Completely constructive interference ($\phi = pi/2$) causes a maximum in the sensitivity of the interferometer to Faraday rotation signals. Conversely, when the interference is completely destructive ($\phi = 0$) the sensitivity is zero. Low-frequency drifts in

the path length thus causes unknown drifts in the sensitivity of the interferometer. This behavior makes it impossible to take reliable, consistent measurements with the interferometer.

To compensate for drift in interference the optical path length of the local arm is continually adjusted using a computer controlled feedback loop. With the feedback loop in place the interference signal is stabilized and is constant over a period several hours. Eventually technical limitations in the control software related to LabVIEW force the control system to be turned off briefly before being reinitiated, a minor inconvenience. Feedback makes it possible to make many reliable, consistent measurements over the course of hours.

The feedback loop uses two separate but equally important components: an active controller and piezoelectric actuator that precisely positions the retroreflector in the local arm with sub-nanometer resolution, and an error amplifier algorithm implemented in LabVIEW running on a PC that stabilizes the interference pattern by continually re-positioning the retroreflector in the local arm. This tiered approach to the feedback system used to stabilize the interferometer leverages the complex technology of the active controller and piezoelectric actuator supplied by Physik Instrumente to produce accurate, repeatable motion of the piezoelectric actuator. Thus, the control loop algorithm implemented in LabVIEW is relatively simple which made it possible to develop within the time-span of the project.

Ideally the control loop would monitor another laser of a different color traveling through the interferometer. A two color setup allows the measured signal for the experiment and the signal monitored for the control loop to be completely independent. This scheme was not feasible since it would have required additional optics, modifications to the interferometer's optical path and more time than was available for the remainder of the project. Therefore it was necessary to imbed the signal used for the control loop within the beam used to make experimental measurements. When doing this it is critically important that the control loop signal not disturb the experimental measurement.

To create a feedback signal that would not disturb the TRFR experimental measurement the retroreflector in the local arm is oscillated with a very small amplitude. This oscillatory motion creates a sinusoidal signal at the photodiodes, which is measured with a lock-in amplifier and analyzed with a control algorithm on a PC.

A flow diagram of the control loop implemented for the interferometer is shown in Fig.3.5. The lock-in amplifier is set so that its internal oscillator is at 733 Hz. This frequency choice was not arbitrary; 733 Hz is outside any low frequency noise, and 733 is a prime number thereby reducing signal mixing with AC signals associated with the experimental measurement which are also set at prime number frequencies. Outputs on the back of the lock-in amplifier provide a low amplitude (0.5 mV_{RMS}) sine-wave signal locked to the internal oscillator frequency and a DC offset that are summed

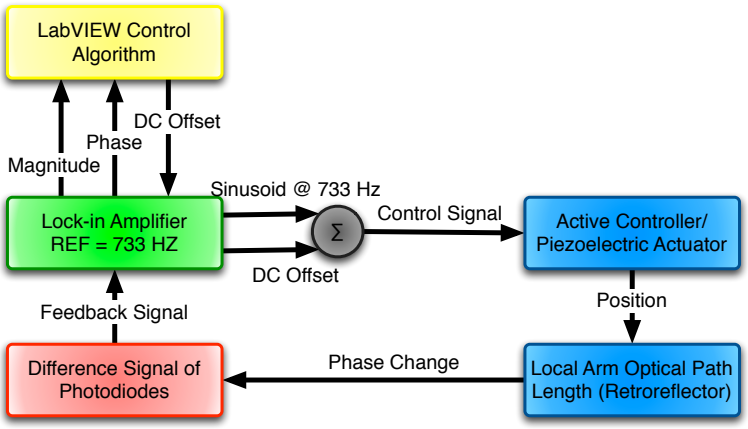

Figure 3.5: Flow diagram of the control loop setup to stabilize the optical path length of the local arm from low-frequency drifts.

together. The summed signal is input into the active controller for the piezoelectric actuator (Note: the summed signal must be within 0-12 V, which is the input range of the active controller). The voltage signal is converted into a position reference and the active controller moves the actuator to track the input.

The small oscillatory motion of the retroreflector perturbs the optical path length of the local arm. Small periodic perturbations to the optical path length can be interpreted as a periodic phase variation between the local and signal arms. The periodic phase variation is modulated by the sinusoidal interference signal, and creates a small feedback signal at the photodiodes that is measured with a lock-in amplifier. An illustration of how the phase variation is modulated by the interference fringe and results in a measurable feedback signal is shown in Fig.3.6. Alternatively the small

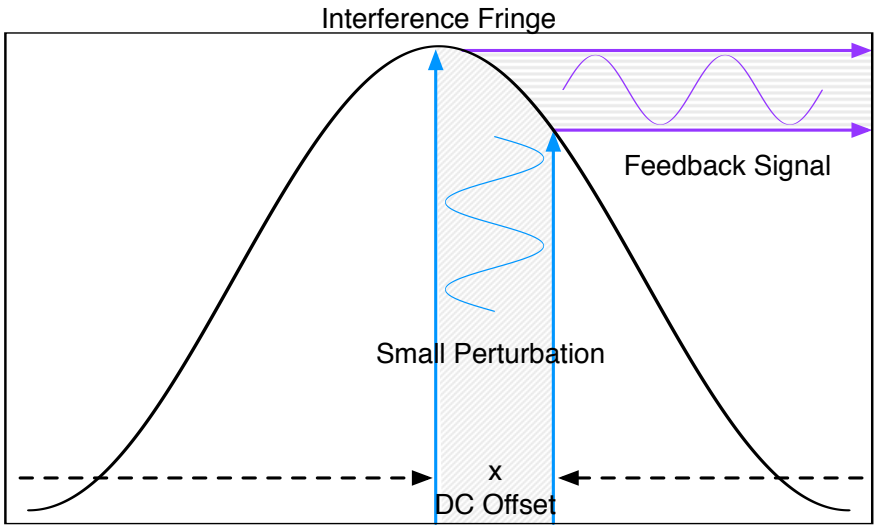

Figure 3.6: Illustration demonstrating how a small periodic variation in the phase (due to a small oscillation of the retroreflector in the local arm of the interferometer) is modulated by the interference signal and leads to a sinusoidal feedback signal. As the DC offset is varied the magnitude of the feedback signal will be affected. When the phase variation is centered on the peak of the fringe the magnitude of the feedback signal is at a minimum. Thus the control system maintains constructive interference between the two beams by continually adjusting the DC offset to minimize the feedback signal.

sinusoidal phase change can be modeled by adding an AC phase term [Eq.3.1]:

$$\begin{aligned} A - B &= 2\sqrt{< P_{Signal} >< P_{Local} >}\delta \sin\phi \\ &= 2\sqrt{< P_{Signal} >< P_{Local} >}\delta \sin(\Delta \sin(\omega t) + \beta) \end{aligned} \tag{3.1}$$

Where $\Delta \sin(\omega t)$ is the varying phase term with amplitude Δ and frequency ω. The DC offset is given by β.

The sinusoidal feedback signal has the same frequency as the exciting AC signal,

733 Hz. Ideally the retroreflector will be positioned so that the interference between the two arms is completely constructive. In this case the DC offset of the control signal is set appropriately and the magnitude of the feedback signal will be minimized (Fig.3.6).

When the interference is completely constructive the periodic oscillation of the retroreflector is centered at the fringe peak where the derivative of the slope is zero. Since the amplitude of the retroreflector's motion is on the order of 0.1 nm, and the wavelength of the laser light used during experiments is between 800-900 nm, this effectively imbeds a sinusoidal signal at near zero amplitude into the difference signal of the photodiodes.

This can be shown mathematically. Consider $\sin(\Delta \sin(\omega t) + \beta)$ from Eq.3.1 and substitute the above values into the equation.

$$\Delta = 2\pi \frac{0.1 \text{ nm}}{800 \text{ nm}} \qquad\qquad \beta = \frac{\pi}{2} = 2\pi \frac{200 \text{ nm}}{800 \text{ nm}}$$

The value for β is chosen so that the oscillation should be centered at the peak of the fringe.

$$\begin{aligned} \sin(\Delta \sin(\omega t) + \beta) &= \sin\left(\frac{2\pi}{800\text{nm}}(0.1\text{nm}\sin(\omega t) + 200\text{nm})\right) \\ &\simeq \sin\left(10^{-3}\sin(\omega t) + \frac{\pi}{2})\right) \end{aligned} \tag{3.2}$$

Therefore the perturbation has a negligibly small effect on the experimental measurement since $\sin(10^{-3} + \frac{\pi}{2})$ is very close to one. Even if the perturbation were on the order of a nanometer the change in the amplitude of the experimental signal would only be 1.5^{-6} %. This is a very small change in the amplitude of the difference signal. Experimental measurements are also taken with a lock-in amplifier at a lower frequency so the noise introduced into the experimental measurement by the feedback signal should be negligible.

However this situation is not ideal, and it would be better if the control scheme did not perturb the signal used for experimental measurements. As mentioned above it was simply not possible to develop another, more robust method of stabilization within the breadth of the project.

The above method of imbedding a feedback signal into the measured signal has been successful in stabilizing the interferometer against low-frequency noise. Completely constructive interference of the two beams can be maintained well over the course of several TRFR measurements. This is important since it maximizes the sensitivity of the interferometer to Faraday rotation signals, and ensures that drifts do not lead to situations where destructive interference occurs and the interferometer's sensitivity falls to zero.

3.4.1 Active Controller / Piezoelectric Actuator

The active controller and piezoelectric actuator were purchased from Physik Instrumente, an industry leader of nano-motion equipment based on piezoelectric materials. Piezoelectric materials are ceramics that compress under an applied voltage (inversely under mechanical stress a voltage is generated across the material). Since there are no moving parts in a piezoelectric actuator movement resolutions that are impossible to achieve with mechanical actuators due to stiction are possible.

A capacitive sensor is built into the piezoelectric actuator, model P-753.1 CD. As the actuator moves over its 12 μm range the capacitance of the sensor changes which is measured by the active controller, model E-665.CR, to determine the position of the actuator. Use of the capacitive sensor allows the active controller to stabilize the position of the actuator with a feedback loop. The active controller is tuned from the factory so that when it is operated in closed-loop mode it eliminates any hysteresis or drift in the motion of the actuator. Adjustments to the position of the piezoelectric actuator in closed-loop operation achieve a resolution of 0.05 nm, a linearity of 0.03%, and a resonant frequency of 2.5 kHz with a 200 g load.

The active controller accepts a voltage input between 0-12 Volts that can be used to tell the controller at what position the actuator should be. This function is used in our setup to oscillate the actuator at 733 Hz and 0.5 Vrms (0.1 nm) and position the actuator using a DC offset. During use, the active controller is always operated

in closed-loop mode so the position and movement of the actuator is stabilized by the controller.

3.4.2 LabVIEW Control Algorithm

Since all the technology for stabilizing the motion of the actuator is contained within the controller the effort to implement a simple stabilization routine for the interferometer was relatively minimal. All that is required of the LabVIEW control algorithm is to analyze the phase of the feedback signal from the lock-in amplifier and digitally adjust the DC offset output of the lock-in amplifier accordingly.

As was explained above, to stabilize the interferometer so that the local and signal beams interfere constructively the magnitude of the feedback signal must be minimized by the control algorithm. To accomplish this, the control algorithm adjusts the DC offset of the control signal (Fig.3.5) so that the retroreflector oscillates around the peak (complete constructive interference) of the interference fringe (Fig.3.6) thereby minimizing the magnitude of the feedback signal.

An example of the feedback signal taken as the algorithm increments the DC offset in 1 mV steps, which corresponds to 0.1 nm step in the position of the actuator, is shown in Fig.3.7. Notice that when the feedback signal is minimized the phase of the signal goes through a jump of 180° or π radians. The jump in phase indicates the sign cahnge in the amplitude of the feedback signal (the lock-in measures the magnitude,

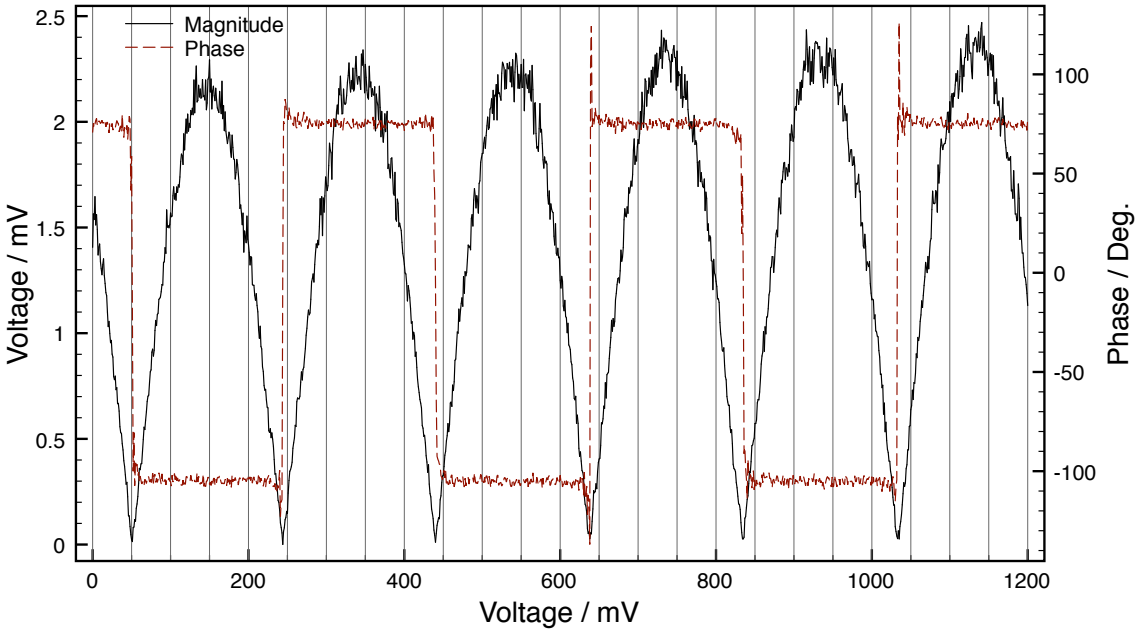

Figure 3.7: Example of the feedback signal measured by the lock-in amplifier as the position of the piezoelectric actuator is increased in 1 mV (0.1 nm) steps. This task is performed by the control algorithm to determine the set-point for the feedback loop. The left axis indicates the magnitude of the signal, and the right axis indicates the phase. Note that although the feedback signal is sinusoidal the lock-in amplifier measures the magnitude, which is unipolar.

absolute value, of the amplitude).

At the set-point (any of the minimums in the magnitude of the feedback signal) the derivative of the phase is much larger than the derivative in the magnitude. Therefore the phase of the feedback signal will be much more sensitive to changes in the DC offset than the magnitude around the set-point. Since the phase is going to respond stronger than the magnitude to changes in the offset of the control signal it is advantageous to indirectly minimize the magnitude by controlling the phase around

a calibrated set-point.

First the control algorithm must determine where the set-point is. To do this the software increments the position of the piezoelectric actuator in 1 mV (0.1 nm) steps (Fig.3.7). At each increment the magnitude and phase of the feedback signal is measured and stored in two centered arrays of adjustable length (usually set to 100 and 10 points). Two arrays of different sizes are used to avoid detecting false minimum in the signal due to noise. For each cycle the software finds the minimum magnitude in each array. The absolute position and value of the minimum for each array is compared and when the two arrays report the same minimum value at the same position the software concludes that the minimum of the magnitude signal has been found. Then the average of the phase at the beginning and end of the large array is computed and is taken as the phase set-point. An illustration of this process is given in Fig.3.8. By taking the first and last values of the phase in the array any anomalies around the phase jump are avoided when computing the average. Note that this set-point finding routine only works if the phase of the internal oscillator of the lock-in amplifier has been adjusted so that the phase of the feedback signal lies within $-180°$ to $180°$.

Once the phase set-point has been determined the value of DC offset is reset to its value the set-point and the control loop is initiated (Fig.3.9).

The control loop algorithm is an error amplifier. During each software cycle the

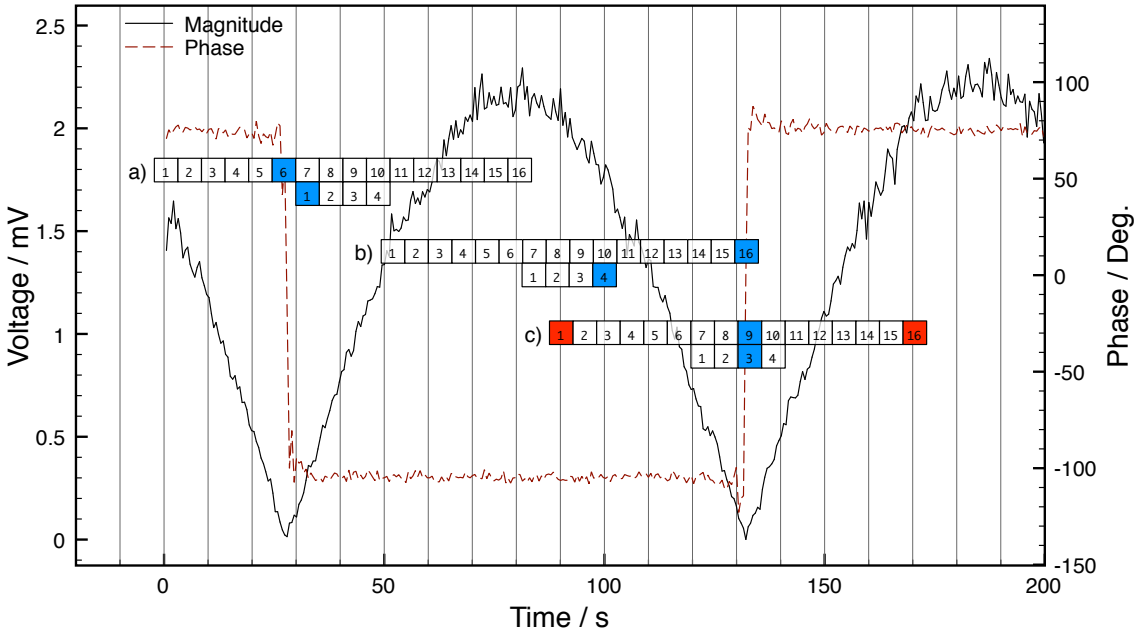

Figure 3.8: Illustration of the algorithm used to find the set-point. The two rectangular boxes represent the large and small arrays. a) The arrays are initialized. The minimum value of the magnitude is found for each array (blue boxes). Since the minimum of each array is different the a the minimum of the magnitude signal has not been found. b) The software continues to scan the magnitude of the signal in looking for the same minimum value at the same point. c) Finally the arrays report the same minimum at the same position. The set-point has been found. Two phase values are then taken from the endpoints of the large array (red) and averaged to compute the phase set-point, around $-15°$ in this case.

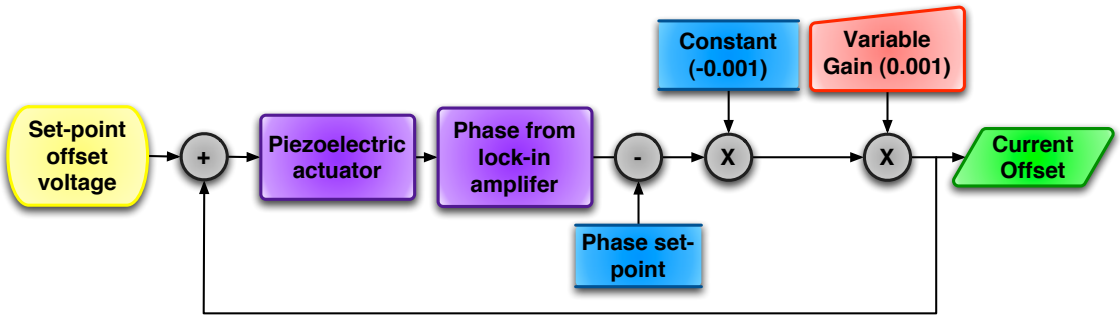

Figure 3.9: Flow diagram of the software control loop implemented to stabilize the interference pattern.

phase at the set-point is subtracted from the currently measured phase value of the signal thereby creating a phase error. The phase error is multiplied by a constant value (-0.001), selected to account for unit conversion within the algorithm, and by an adjustable gain value. The product of the gain value with the phase error is then added to the current DC offset and the cycle repeats.

It is rare for the phase to exactly equal the set-point value because the phase is so sensitive to changes in the DC offset (position of the piezoelectric actuator). Instead when the control loop is operating the phase bounces quickly between values above and below the set-point, but the magnitude of the feedback signal remains near the minimum value (Fig.3.10).

Using this control system the optical path length of the interferometer can be stabilized to within 1 nanometer. This is a significant accomplishment considering the interferometer is approximately 1-2 square meters in area (Fig.3.11).

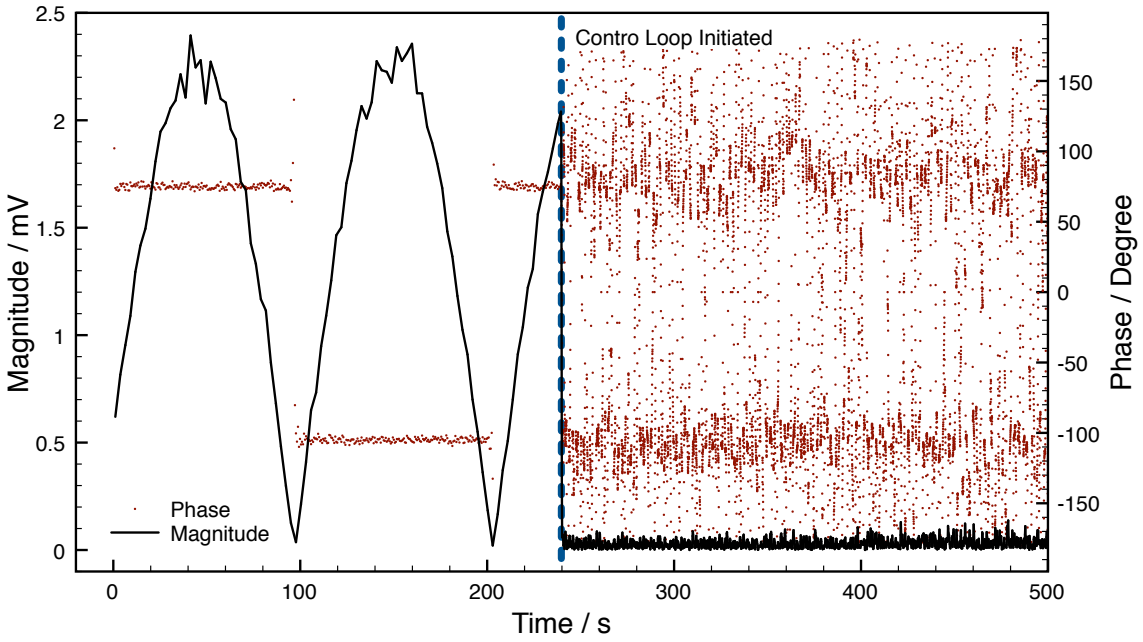

Figure 3.10: Example of the how the magnitude and phase of the feedback signal change once the control loop algorithm is initiated.

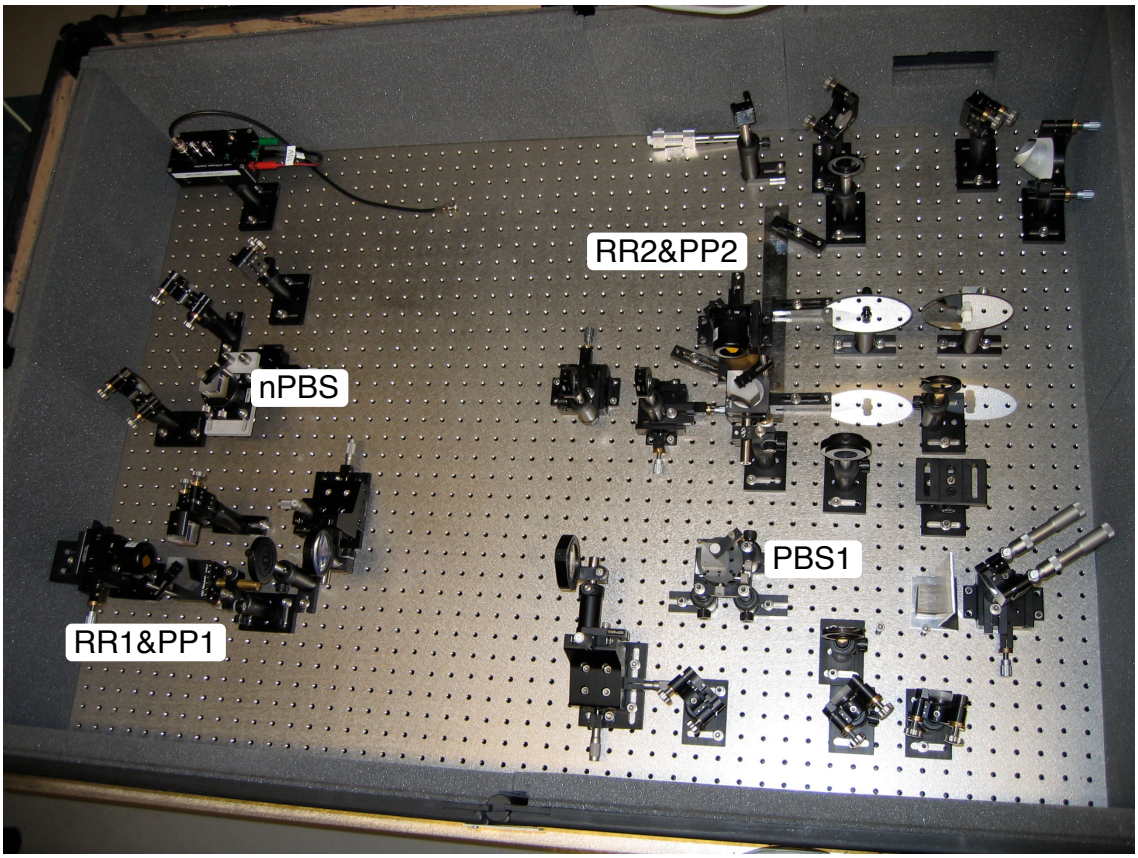

Figure 3.11: Photo of the interferometer and the acoustical box wall (§3.3). To provide a sense of scale, the holes on the table are spaced 1 inch apart. Note that both PBS3 and the sample are absent from this photo.

The magnitude, phase, and offset history is all saved and this sets a limit on how long the control algorithm can be run. Eventually the performance of LabVIEW begins to degrade as the saved data becomes too large. This behavior is not detrimental to experiments because the control algorithm can easily be reset within minutes between experimental runs.

3.4.3 Failed Stabilization Schemes

Before the stabilization scheme described above (§3.4) was developed and implemented a lot of effort went into attempting different schemes for measuring the TRFR signal. Aligning the optics in the interferometer so that constructive interference could be achieved between the two arms was only half the work. Making a stable, consistent TRFR measurement in the presence of noise, especially the low-frequency drifts that have a parasitic affect on the sensitivity, effectively negating any gains made through optical amplification, was a difficult task.

Before developing direct active stabilization of the interferometer several other solutions for making an accurate Faraday rotation measurement were investigated. These techniques were originally seen as shortcuts or quick-fixes, that would save us from having to build an active control system. During the beginning of the investigation all that was available to control the motion of the retroreflector RR2 was a rather inexpensive piezoelectric actuator operated in open-loop mode. The sophis-

ticated piezoelectric actuator and active controller used in the final control scheme was purchased much later on when sufficient justification of its utility warranted the expenditure.

Peak Detection

One of the first schemes we attempted was to move away from a frequency measurement with the lock-in amplifier and instead make a measurement with an analog-to-digital converter ("ADC"). The idea was to oscillate RR2 enough that it would pass through several fringes, thereby creating a periodic sine wave at the photodiodes. By continually sampling the signal at the photodiodes it was thought that perhaps the peak of the fringes could be detected. Since Faraday rotation would cause an increase in the peak of fringes it could be detected in this way.

However it was soon realized that the ADC scheme, while feasible, would not provide sufficient sensitivity to the TRFR signal. The ADC, even at 16-bits, and 100 kHz sampling rate was simply not sensitive enough. Even upgrading the equipment for high-resolutions, and sampling rates was not going to be enough to give us the required sensitivity. It was clear that a lock-in amplifier would need to be used to achieve the required sensitivity.

Modulation / Gated Sinusoid

At this point it was clear that the lock-in amplifier was the correct instrument to reach the required level of sensitivity.

The difference signal at the photodiodes is sinusoidally dependent on the phase difference between the two arms of the interferometer [Eq.2.19]. Oscillating the retroreflector in the local arm with an amplitude of several wavelengths will therefore cause a sinusoidal signal at the photodiodes. Since the amplitude of the interference fringes is related to the amount of Faraday rotation in the signal arm [Eq.2.19] the lock-in amplifier, properly referenced, should be able to measure the Faraday rotation.

Initially we attempted to oscillate the retroreflector with a sinusoidal voltage. Ideally this would have produced a frequency modulated signal at the photodiodes [Eq.3.3].

$$\begin{aligned} A - B &= 2\sqrt{P_S P_L}\delta \sin\phi \\ A - B &= 2\sqrt{P_S P_L}\delta \sin(A\sin(\omega t) + B) \end{aligned} \tag{3.3}$$

Where A contains the amplitude of the retroreflector's motion, and B contains the central position of the retroreflector around which is oscillates. Both of these parameters can be tuned by adjusting the amplitude and DC offset of the voltage signal that drives the piezoelectric actuator's motion.

This signal [Eq.3.3] is of the form:

$$A - B = C_1 \sin(C_2 \sin \omega t + C_3)$$

The Fourier series coefficients for this signal are linearly dependent on C_1. Thus, if C_2 and C_3 are held constant the lock-in amplifier can be used to measure the magnitude of one of the Fourier components and therefore the Faraday rotation since $C_1 = 2\sqrt{P_S P_L}\delta$.

We attempted to reference the lock-in amplifier using either the first or second harmonic of ω. At the time the position of the retroreflector was controlled with a different piezoelectric than the one described in the above (§3.4.1) and without an active controller. Due to the deficiencies in the actuator the retroreflector was not able to follow the exciting voltage signal (Fig.3.12). The unexpected motion of the actuator caused random noise and large-scale drifts in the magnitude and phase of the lock-in signal. Thus this mode of excitation proved ineffective.

Next we tried to improve the signal at the photodiodes by moving the retroreflector with a triangle waveform. If the motion of the actuator properly tracks the linear ramp-up and ramp-down components of the triangle waveform the retroreflector's motion will produce a constant phase-change between the local and signal arm. A constant phase change will result in a constant sweep through the interference fringes

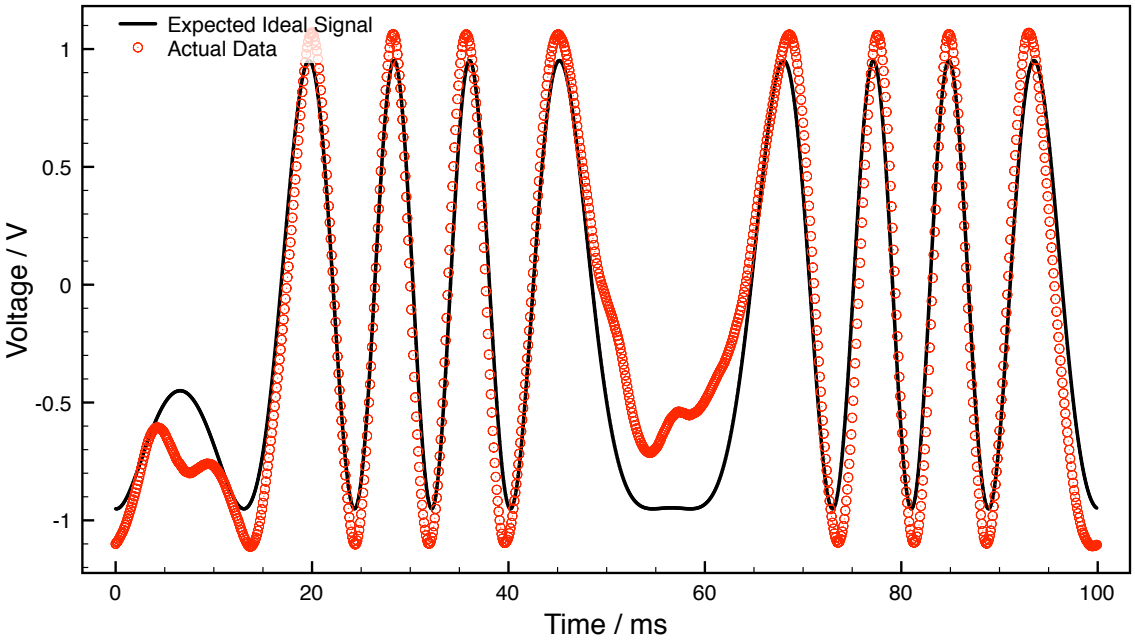

Figure 3.12: Expected and resulting signal at the photodiodes generated by the sinusoidal oscillation of the retroreflector [Eq.3.3]

which will result in a sinusoidal signal of a single frequency at the photodiodes [Eq.3.4] (the frequency of the sinusoid will change signs corresponding to either the ramp-up or ramp-down section of the triangle waveform).

$$\begin{aligned} A - B &= 2\sqrt{P_S P_L}\delta \sin\phi \\ &= 2\sqrt{P_S P_L}\delta \sin(At + B) \\ &= 2\sqrt{P_S P_L}\delta \sin(n\omega t + B) \end{aligned} \tag{3.4}$$

Where n is the number of interference fringes scanned through by the movement of the retroreflector and B is the starting point of the motion. It is implied that n is an integer; this is true and it is critical that n be an integer for the lock-in amplifier to be successful in measuring the Faraday rotation.

The lock-in amplifier will properly measure the Faraday rotation from the signal [Eq.3.4] only when n is an integer and the photodiode signal is gated so that only the ramp-up (or ramp-down) section of the signal is input to the lock-in. Thus the signal input to the lock-in amplifier will be a sine-wave of n periods for half of the duty cycle of the gate, and zero for the other half. If the frequency of the gated signal (and therefore the motion of the retroreflector) is faster than the major noise sources, so that B is constant over several periods of the gated signal, the magnitude of the lock-in amplifier's measurement will be proportional to the Faraday rotation. Any

noise sources will appear only in the phase channel of the lock-in amplifier, effectively decoupling the phase noise in the interferometer from the Faraday rotation signal.

We initially attempted gating the signal electronically but found limited success. Optically gating the signal with an optical chopper was not any more successful. While we were able to see an improvement in the long-term stabilization of the magnitude channel of the lock-in amplifier over the previous FM modulation scheme the quality of the measurement was not sufficient to make a Faraday rotation measurement.

An example of a lock-in measurement using the gated photodiode signal is shown in Fig.3.13. The magnitude channel is fairly constant, but a lot of higher frequency noise components are present that limit the sensitivity to Faraday rotation.

Two issues prevented this measurement scheme from being successful. The requirements on the motion of the piezoelectric actuator both to create n-integer fringes, and move linearly through the ramp were impossible to meet with the open-loop piezoelectric setup. Deviations from an integer value of n causes frequency beating between the lock-in amplifier's internal oscillator and the signal, which introduces low-frequency drift into the magnitude channel.

Second, synchronizing all the electronics and mechanical devices with the lock-in amplifier with a stable, precise reference clock frequency also proved to be a difficult task. Small variations on the order of 0.001-0.01 Hz in the reference frequency

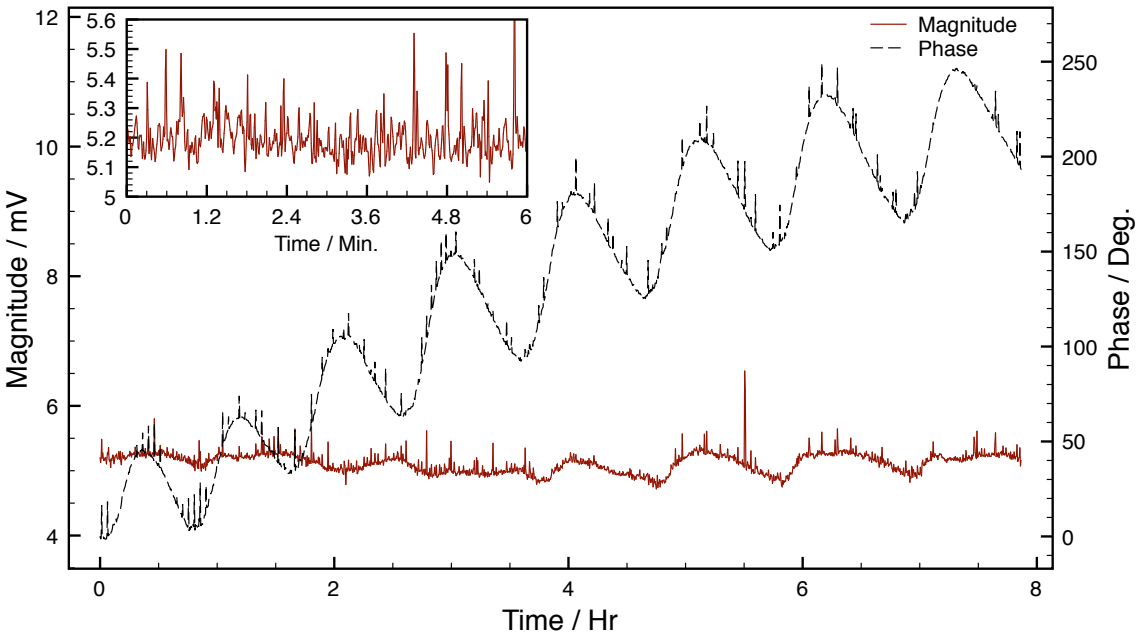

Figure 3.13: Magnitude and phase channel of a lock-in measurement of the gated sinusoidal signal presented above [Eq.3.4]. The insert is a close-up of the magnitude channel.

of the electronics also introduces noise into the magnitude channel of the lock-in measurement. To get around the limitations in synchronizing the electrical components, we tried to reference the lock-in amplifier directly with the dominant frequency component of the photodiode signal. This was accomplished either through virtual referencing the lock-in amplifier, or by analyzing the photodiode signal with a digital filter that output a reference clock signal at an appropriate frequency. Both of these methods were insufficient at reducing the noise and drifts in the measured signal down to an acceptable level.

Considerable effort went into developing electronic equipment to test and improve this measurement scheme. It was originally an idea that was supposed to be easier and quicker to implement than a control scheme described above (§3.4). While it is technically possible, in the end we were not able to meet the strict requirements of the piezoelectric motion and this scheme also failed. In retrospect the idea should have been abandoned earlier than it was, but what we learned during this period of the project led to a final working solution. Also a strong case was made for a better piezoelectric actuator that would be able to move the retroreflector accurately and repeatedly.

3.5 Description of the Beam Path

In the previous sections the four main design challenges associated with developing the interferometer were discussed. It is now appropriate to give a brief description of the optical components used throughout the interferometer. Refer to the schematic of the interferometer (Fig.3.1) where necessary. (Note: There is some overlap between this section and the previous sections in this chapter.)

Detailed alignment and operation procedures for the interferometer are provided in Appendix A and technical information about the optical components can be found in Appendix B.

3.5.1 Pump Beam

A variable attenuating wheel (VA1) is used to control the pump beam power. Two steering mirrors (M1,M2) are used to direct the pump beam so that it is parallel to the probe beam. When the pump beam is properly aligned both the pump beam and signal beam will be focused by the achromatic doublet lens (L1) onto the same spot on the sample.

Actuators with micrometer resolution are used to maintain precise control over the tilt of the steering mirror M2. Without the fine control over the tilt of the optical mount used to hold mirror M2 provided by the micrometers it would not be possible to overlap the signal and pump beam on the sample. These fine controls are used

during experiments to optimize the TRFR signal which only occurs within a range of approximately 2 μm for both the horizontal and vertical tilt axis.

3.5.2 Probe Beam

A variable attenuating wheel (VA2) is used to control the power in the pump beam. The half-wave plate (HW1) is used to rotate the oscillation axis of the probe beam. Since the local and signal beams are split from the probe beam using a polarizing beam splitter the ratio of power between the local and signal arms can be adjusted with half-wave plate HW1. When the incoming oscillation axis of the probe beam is at a 45° angle with the polarization axis of the beam splitter the signal and local arms will be at the same power.

The two steering mirrors (M3, M4) are used primarily to add extra length to the beam line. This is done to ensure that the zero point, the point where pulses from the signal beam and pump beam overlap in time, can be found within the temporal delay accessible with the mechanical delay line (§4.2). Mirrors M3 and M4 are also used to make any final adjustments to the beam height.

A polarizing beam splitting cube (PBS1) is used to split the probe beam into two orthogonal polarization components. One component is transmitted through the cube and is labeled as the local beam, since it does not pass through the sample and serves as a reference to the original state of the beam, and the other beam is labeled

the signal beam since it travels through the sample.

The beam splitting cube (PBS1) is mounted on a three-axis tilt mount so that independent rotations around each axis can be performed. This level of control is absolutely necessary so that the incoming beam is normal to the surface of the cube and that the two outgoing beams are propagating horizontally to the table. Fine controls are not necessary on the tilt mount, but they would be a useful addition which would allow even more precise control over the vertical tilt of the signal and local beams. However other degrees of freedom elsewhere in the interferometer can be used to compensate for small misalignments in the vertical tilt of the signal and local beams.

Signal Arm

A pair of achromatic doublet lenses are used to focus the signal beam and pump beam onto a spot of roughly $50\mu m$ on the sample and then collimate the signal beam. Both of the achromatic doublet lenses have a diameter of $2''$ so there is a large enough clear aperture on the first lens to accommodate the full beam waist (1 cm) of both the signal and pump beams. Although it is not pertinent that the pump beam be collimated after passing through the sample the second lens (L2) must be the same diameter as the first to reduce unwanted distortions of the wavefront (§3.2). Pragmatically, the use of matched lens pairs for the collimator eases the alignment of

the lens considerably.

Both of the achromatic doublet lenses are mounted on three-axis linear translation stages. Each of the axis on the stages is controlled by a manual actuator with micrometer resolution. The alignment of the lenses is much easier when using three-axis translation stages than when using stages with only one or two axes, which means height adjustment must be made by hand with the post and post-holder. Markings on the actuators allow the lenses to be moved together accurately. Although the three-axis stages for L1 and L2 are not strictly necessary at this time it is hoped that future work on the interferometer will house the sample in a cryostat so that experiments can be performed at cryogenic temperatures and magnetic fields of several Telsa. With the sample inside a cryostat it will not be possible to move the sample into focus, instead the lenses will have to be adjusted to bring the focus to the sample. In this scenario it will be necessary to be able to move both L1 and L2 together accurately so that beam collimation is maintained.

The hollow retroreflector (RR1) is mounted on a vertical one axis translation stage which is used to adjust the height of the beam to optimize the overlap of the signal and local beams. Vertical adjustment of the position of retroreflector RR1 is important because the height of the beam in the local and signal arms may not be matched. Hollow retroreflectors are superior to glass retroreflectors since they eliminate dispersion in the beam (§3.2) which spreads the pulse thereby reducing the

temporal resolution of experiments. There is also the danger that if the dispersion is not matched in both arms of the interferometer it will lead to a severe degradation in the visibility of the interference pattern.

A glass penta-prism (PP1) reflects the beam at a right-angle invariant to the angle of incident of the beam on the surface of the glass; the beam can be incident on the surface of the prism at a non-normal angle and still undergo a right-angle reflection. Ideally hollow penta-prisms would be used in the interferometer to eliminate dispersion, but they are far more costly then their glass counterparts. Since both arms contain a glass penta-prism the dispersion in each arm is matched and good visibility of the interference pattern can be still be achieved. The penta-prism combined with the retroreflector allows for precise, incident angle invariant, right angle reflections (§3.1).

It is important that the signal and local beams intersect at a right-angle on the non-polarizing beam splitter. The beam reflected from the retroreflector is parallel to the incident beam to within 5 arc seconds. The penta-prism which reflects the beam at 90° within 30 arc seconds. With the combination of the retroreflector and penta-prism it is possible to perform the right-angle reflections in the local arm and signal arm to within a maximum error of 35 arc seconds. Although it is possible to duplicate this level of pointing accuracy with a mirror mounted with micrometer resolution actuators it would be considerably more difficult to align.

Penta-prism (PP1) is mounted on a flat stage with tilt controls. Rotation of the penta-prism around the vertical axis (axis normal to the surface of the table) can only be achieved by coarsely positioning the prism on the stage, or rotating the stage on its post. Finer control over the rotation of the prism is not necessary since the beam is reflected at a right-angle regardless of the angle of incidence. The tilt controls are used to ensure that the incoming beam is incident normal to the prism (in that degree of freedom) and to ensure that the outgoing beam is horizontal to the table.

Finally another polarizing beam splitter (PBS2) filters out the non-rotated components of the signal beam before the signal beam and local beam are recombined at the non-polarizing beamsplitting cube (nPBS). The beam splitter, PBS2, is mounted in a stage similar to a mirror mount that allows vertical and horizontal tilt control. Therefore the cube can be positioned so that the beam is incident normal to the face of the cube.

Half-wave plate HW1 is used to adjust the oscillation axis of the signal beam which effectively controls the transmitted power through PBS2. This functionality is useful for testing purposes. During experiments the half-wave plate is orientated so that it does not rotate the signal beam.

Local Arm

The contents of the local arm beam path are the same as the signal arm (§3.5.2) with the exception of the beam collimator composed of lenses L3 and L4, and the mount for retroreflector RR2. The arms of the interferometer must be similar so that each beam undergoes the same wavefront transformations (§3.2).

Instead of using achromatic doublet lenses with a $2''$ diameter for lens L3 and L4 achromats with a $1''$ diameter are used. The larger lenses are not necessary. The lens pair will also be static after the initial alignment even if a cryostat were added to the interferometer. Thus these lenses do not require the expensive three-axis linear stages used for L1 and L2 in the signal arm. A one and two-axis linear stage are used instead. These stages are sufficient for positioning the lenses with the needed accuracy.

Retroreflector RR1 is mounted on a vertical translation stage. This functionality does not need to be duplicated in the local arm. Instead the retroreflector RR2 is mounted onto a one-axis linear translation stage and a piezoelectric actuator with a $12\mu m$ range to equalize the optical path lengths of both arms (§3.4.1).

Rigidly mounting the retroreflector is important for the piezoelectric actuator to be able to move RR2 smoothly. Physik Instrumente, the supplier for the piezoelectric actuator, provided advice on how to mount the piezoelectric actuator so that the mount would be sufficiently rigid and a one-axis manual linear translation stage could

be used to center the overlap of the local and signal beam pulses.

The key component of the mount for the actuator is a heavy, rigid brass post that is $2''$ in diameter. A post and post-holder configuration which is typically used for optics will not provide a rigid enough mount for the actuator. A one-axis linear translation stage for coarse, long-range adjustments is rigidly mounted to the surface of the optics table. Sitting on top of the stage is a brass post which provides a rigid, massive object on which to mount the piezoelectric actuator.

3.5.3 Recombination Cube

Arguably the most critical component of the interferometer is the non-polarizing beam splitting cube used to recombine the local and signal beams. The cube is mounted one a three-axis tilt and rotation stage. Each axis is controlled with a differential micrometer with 0.2-0.3 arc second resolution.

This level of rotation resolution is important for the cube mount since the overlap of the two beams is extremely sensitive to the positioning of the cube (near the resolution limit of the differential micrometer), especially to rotation around the vertical (normal to the table surface) axis. Even with the differential micrometers the positions of the cube can be touchy and requires a bit of optimization.

The tilt mount is positioned on a platform anchored to a one-axis linear translation stage. The axis of the stage is aligned with the beam line of the local arm so that

the cube can be moved along the beam in the local arm and positioned so that both beams overlap within the cube.

Chapter 4

Supporting Optical Systems

A Coherent Mira 900-F Ti:Sapphire pulsed laser system has been used as the primary laser source throughout the project. The Mira is pumped by a 10 Watt Coherent Verdi V-10 diode pumped laser. In this configuration the Mira is able to output horizontally polarized pulses at a repetition rate of 76 MHz with a optimal pulse width of 130 fs.

Between the Mira and the interferometer the beam is split into a pump and probe beam. The pump beam's polarization is made to be circularly polarized with a variable retarder optimized for the wavelength of operation. A variable time delay is introduced between the pulses in the pump and probe been with a mechanical delay line. Finally both beams are mechanically chopped at their focus and expanded before entering the interferometer. The installation of the optics required to perform these actions on the beam were non-trivial. There have also been several revisions to the

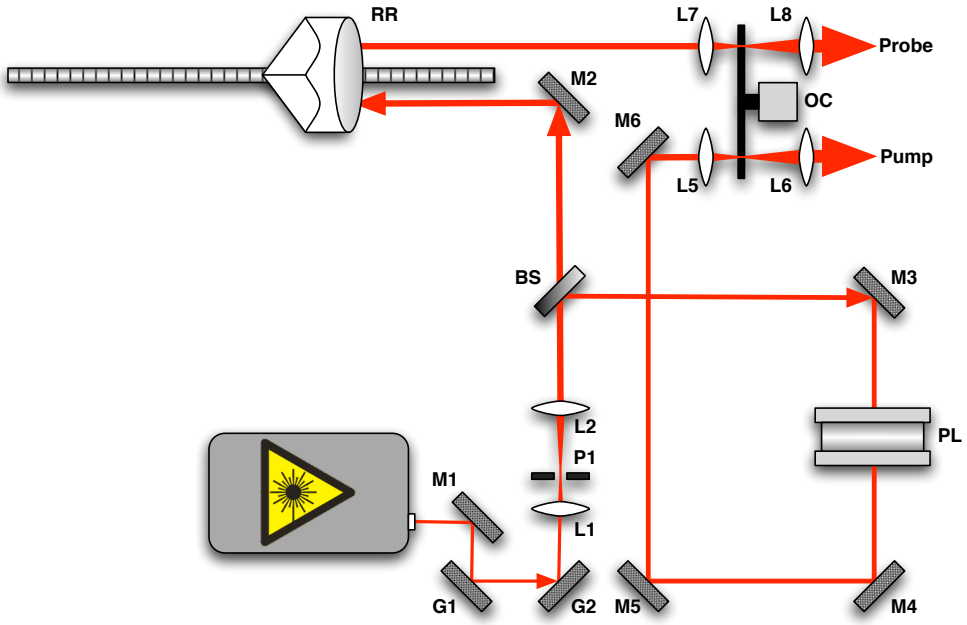

Figure 4.1: Diagram of the optical setup before the interferometer (not to scale). M1-6 = Mirrors. G1-G2 = Gimbal mounted mirrors. L1-L6 = Lens. P1-P2 = Pinholes. BS = Beamsplitter. PL = Berek Polarizer. RR = Retroreflector. OC = Optical Chopper.

configuration of the optics used for these purposes over the course of the project. This was necessary to remedy recurring beam misalignment caused by an apparatus overly sensitive to mechanical vibrations, to improve the beam quality entering the interferometer or because the Mira failed thereby forcing a complete re-alignment of the beam line.

A schematic of the optics used (Fig.4.1) and an outline of their installation follows.

4.1 Overview of Optics Layout

Upon exiting the laser cavity the beam is directed using a pair of gimbal mounted mirrors (G1-G2). These mirrors allow for small corrective adjustments to the beam path, with minimal adverse effects from beam translation inherent to non-gimbal mounted optics. By placing the axis of rotation at the center of the mirror, gimbal mounts avoid beam translations, which are inherent in standard optical mounts where the axis of rotation is located at the corner of the mount. A pair of mirrors are used in order that small corrections can be made to the pointing of the beam as well as small beam translations. Due to the distance traveled by the beam between the laser cavity and photodiode detector within the interferometer, and the large number of optics in the beam path, the small translations caused by non-gimbal mounted mirrors are catastrophic to the interference pattern.

After the gimbal mounts, the beam is expanded by a factor of two with a pair of achromatic doublet lenses, L1 and L2. The beam is spatially filtered at the focus of L1 by a 75 μm pinhole (P1) and then collimated with lens L2. The pinhole also acts as a reference point for the location of the beam at initial setup. By using another aperture or pinhole further down the beam path (not shown), two stable reference positions of the beam path during initial setup are available. Disturbances in the beam path can then be detected and corrected for.

Achromatic doublet lenses are used throughout the interferometer and supporting

optics instead of spherical singlet lenses. Achromats provide superior performance to singlet lenses with smaller focal spots, and far superior off-axis performance. More importantly, achromats have near constant focal length across a wide spectrum of wavelengths. It is vital to the experiments done within the lab that the laser wavelength can be tuned to any wavelength in its operating range (700 nm to 1000 nm). Any beam collimators made from singlet lenses will be misaligned after tuning the laser, this is clearly not acceptable and therefore achromatic doublet lenses are used for all of the beam collimators on the optics table.

A 70:30 non-polarizing beam splitter (BS) divides the beam into a probe beam (70%) and a pump beam (30%). The pump beam is passed through a Berek polarization compensator (PL), a variable retarder, that is used to convert the polarization of the pump from linearly polarized to circularly polarized. The loop created by mirrors M3, M4, M5 is used to create extra time delay in the pump beam so that the zero-point, the point on the mechanical delay line where the retroreflector is positioned so that pulses from both the pump and probe beam arrive at the sample in the interferometer at the same time, is near the front of the delay line.

After the beam splitter (BS) the probe is directed with mirror M2 into a mechanical delay line. The delay line is used to adjust the temporal difference between pulses in the probe and pump beam arriving at the sample within the interferometer. By delaying the probe beam by small increments a time-resolved measurement can be

made.

Finally both the pump and probe beams are transmitted through a pair of achromatic doublet lenses: L5-L6 for the pump, and L7-L8 for the probe. The focal length of the second lens in each pair is approximately twice the length of the first. Thus both the pump and probe are expanded by another factor of two before being recollimated by L6 and L8 respectively. Both the pump and probe beam have a beam diameter that is approximately four times the diameter ($\sim$ 8 mm) of the beam exiting the Mira's laser cavity ($\sim$ 2 mm). The beam is expanded in order to decrease the beam waist at the focus on the sample. The spot size is inversely proportional to the beam waist before focusing as shown in Eq. 4.1 where λ is the wavelength of light, ω_0 is the focal spot diameter, F is the focal length of the lens and D is the beam waist illuminating the lens. A smaller spot size on the sample has the advantage of increased spatial resolution for pump/probe experiments.

$$\omega_0 = \frac{4\lambda F}{\pi D} \tag{4.1}$$

4.2 Mechanical Delay Line

The purpose of the mechanical delay line is to create an adjustable path length for the probe beam. Hence the difference in arrival times between the probe and pump

pulses on the sample can be varied manually or via a computer interface.

The delay line consists of a hollow retroreflector (RR), chosen to eliminate unwanted pulse dispersion, that moves along a metal track parallel to the beam line. It is critical that the track be as close to parallel to the beam line as possible. Any deviations from the beam line will cause a translation of the reflected beam as the retroreflector moves along the track thereby causing any subsequent alignment of optics in the probe beam to be lost. Thus, care should be taken to ensure that the track is straight and flat. Minor thermal fluctuations can place stress on the track and cause it to bow if it is not properly mounted. This will result in a vertical translation of the retroreflector and cause misalignment of the optics in the probe beam's path. Minor thermal variations in the surface of the optics table should be accounted for when mounting the track. After mounting the track the steering mirror M2 can be used to direct the beam parallel to the track.

The range of temporal variation between the pump and probe pulse arrival time is dependent on the distance the retroreflector can travel along the track (a maximum value of temporal variation is set by the repetition rate of the laser). Originally the delay line was setup so that the probe beam made two passes so that a delay greater than the pulse separation was possible. This would allow the probe beam to be delayed by a complete cycle of the laser relative to the pump beam. The Faraday isolator used to create a double-pass delay line caused repeated problems with the operation of the

Mira as back reflections would cause the laser to lose mode-lock. The extra distance traveled by the beam also made the system even more susceptible to misalignment. After several realignments caused by complications with the double-pass delay line setup, it was abandoned in favor of the current single-pass configuration. The single-pass configuration is much more robust and provides a factor of two increase in the temporal resolution in exchange for halving the temporal variation available.

A stepper motor is used to control the movement of the retroreflector. The stepper motor turns a gearbox which reduces the movements of the motor by a factor of one hundred. The smallest achievable step in delay is 0.0202 ps. A RS232 serial communication interface between the stepper motor and lab computer allows for computer control of the motion of the mirror during experiments.

Chapter 5

Experimental Setup

5.1 Semiconductor Samples

All of the Faraday rotation experiments were performed with GaAs samples. The samples were prepared from mechanical grade Si n-doped GaAs [100] wafers with a dopent concentration of $N_c = 2.6 \times 10^{16}\text{cm}^{-3}$. This doping concentration was chosen since long spin lifetimes (§1.1) have been reported with samples at similar doping concentrations.[15] A two-dimensional array of micron thin windows were etched into the wafers by Alastair Fraser, a undergraduate research assistant, while working at the University of Alberta. These windows were necessary to reduce the amount of signal beam attenuation through the sample.

A pair of scanning electron microscope (SEM) images of the windows are shown

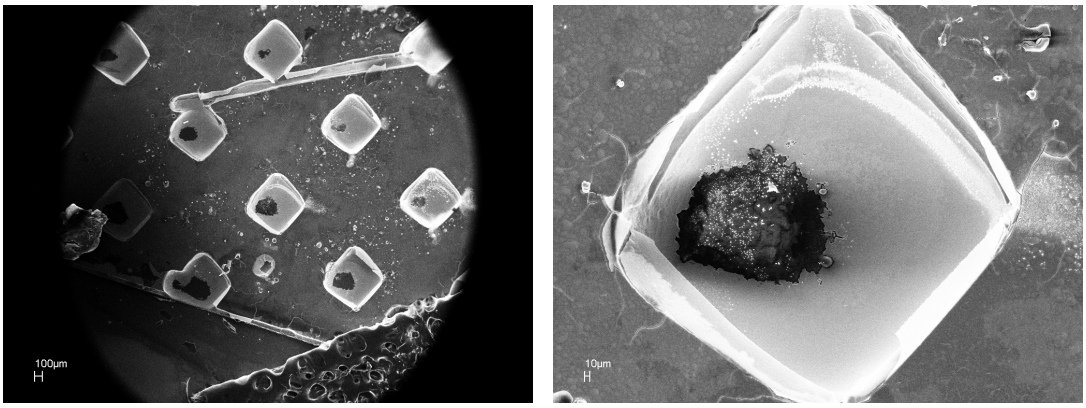

(a) (b)

Figure 5.1: Both images were taken before the photo resist used to pattern the arrays was removed from the sample. The windows are $100\mu m \times 100\mu m$ in area. a) SEM image of an array of etched windows on the GaAs wafer. b) A close up SEM image of the one of the windows.

in Fig.5.1. Notice that the surface inside the windows is not smooth. Ideally the samples would be grown using molecular beam epitaxy to achieve atomically smooth windows (to reduce beam diffraction) several monolayers thick, but such samples were not available to us.

5.1.1 Mounting

Samples are placed between square neodymium magnets of dimensions $2'' \times 2'' \times 0.5''$ inside the signal arm. The magnets are mounted as closely together as possible (approximately 33 mm) to create the strongest magnetic field possible. Since the Larmor frequency of electron spin precession is proportional to the externally applied magnetic field strength [Eq.1.5], a strong magnetic field is desired so that several

periods of precession can be measured before spin relaxation. In our configuration the magnets produce a field strength of 0.25 Telsa, which results in a Larmor precession period of approximately 0.65 ns.

Each of the samples were mounted onto a piece of glass microscope slide with a suitably large section hung off of the slide. This allows the signal beam to be transmitted through the sample without going through the glass slide. Rubber cement was strung around the samples to tie them to the glass slide. A minimum amount of adhesive should be used since the stresses placed on the sample while the adhesive sets could cause it to break. Double sided scotch tap was used to mount the glass slide to a two-axis optical mount. The controls on the mount were used to adjust the incident angle of the beam with the sample's surface.

A three-axis linear translation stage is used to control the position of the sample within the beam. Although the focus could be adjusted with the controls on L1 and L2 so that it resides on the sample (§3.5.2), it is much easier and quicker to move the sample to the appropriate position within the beam path. Manual actuators with threads of 100 turns per inch were used to position the sample in the beam.

5.2 Electronics (and Optics)

Time resolved Faraday rotation measurements were made with both the interferometric setup and with the optical bridge setup. There are similarities between these two

experimental setups but the interferometer setup is, as expected, more complicated.

It was important that the two detection schemes be configured as similarly as possible so that useful comparisons between them could be made. To this end the same sample was used in both experiments and the optical bridge was setup using the signal arm of the interferometer (§5.2.2). Optical bridge measurements were also performed inside the acoustical dampening box used by the interferometer.

5.2.1 Interferometer

There are two components to the interferometer's setup: the control software and equipment, and the measurement software and equipment.

A detailed explanation of the control system has been given in §3.4. The central component of the control system is a 7265 Signal Recovery lock-in amplifier operated in internal reference mode. An external summer circuit combines a DC signal from one of the ADC outputs on the back of the lock-in and a sine-wave at a frequency of 733 Hz and amplitude of 0.5 mV from the internal oscillator output. The summed signal is input on the front of the piezoelectric actuator's active controller to control the offset and motion of the actuator. The lock-in amplifier monitors the photodiode difference signal at the internal oscillator frequency (733 Hz), which is also the oscillation frequency of the actuator. In order to measure the control signal the lock-in amplifier was set to a sensitivity of 5 mV, with a time-constant of 100 ms.

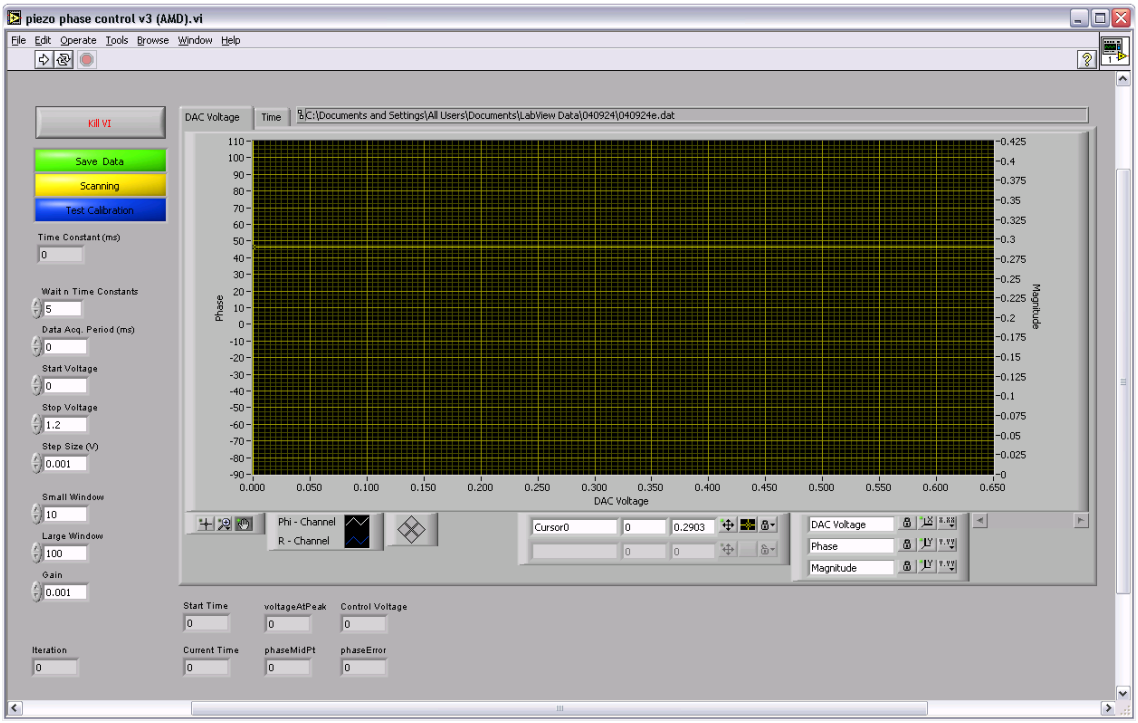

Figure 5.2: Screen capture of the user interface for the control software VI.

A personal computer connected to the lock-in amplifier via GPIB runs a LabVIEW VI called *"piezo phase control (AMD) v3.vi"* (Fig.5.2). The VI monitors and records the DAC output voltage, time, and magnitude and phase of the input signal. Controls are available for adjusting how many time-constants the software should wait before making the next measurement when in calibration mode. Both the start voltage, stop voltage and step size of the calibration can be adjusted, as well as the size of the small and large window arrays used to find the set-point. Once the VI is calibrated to the phase set-point the gain used in the control software's error amplifier can be adjusted.

For the experiments presented here the control software VI was always configured with a wait time of five time-constants between measurements. The large and small window arrays were consistently set to sizes of 100 and 10 respectively. Several gain parameters were tested before experimentation. With a gain value of 0.001 the error amplifier was best able to stabilize the interferometer, and therefore this value was used throughout our experiments.

To measure the Faraday rotation, another lock-in amplifier, an SRS SR830, measures the photodiode difference signal at the reference frequency of the optical chopper used to chop the pump beam. During our experiments, the pump beam was always chopped at 509 Hz, a prime number and lower frequency than the piezoelectric actuator's oscillation frequency. This frequency was chosen to prevent mixing between the feedback signal and Faraday rotation signal. The power level output on the Mira laser controller is connected to a ADC input on the lock-in amplifier so that any drifts in the power level of the laser can be removed from the measured signal. During TRFR experiments the SR830 was set to a sensitivity of 5 mV and a time-constant of 300 ms.

A LabVIEW VI, *"PI scan and measure (serial SR830) v3.vi"*, running on a separate computer measures several parameters (delay, magnitude, phase, x, y, time, reference frequency, and laser power) from the SR 830 via a RS-232 serial interface while positioning the retroreflector along the mechanical delay line (Fig.5.3). The

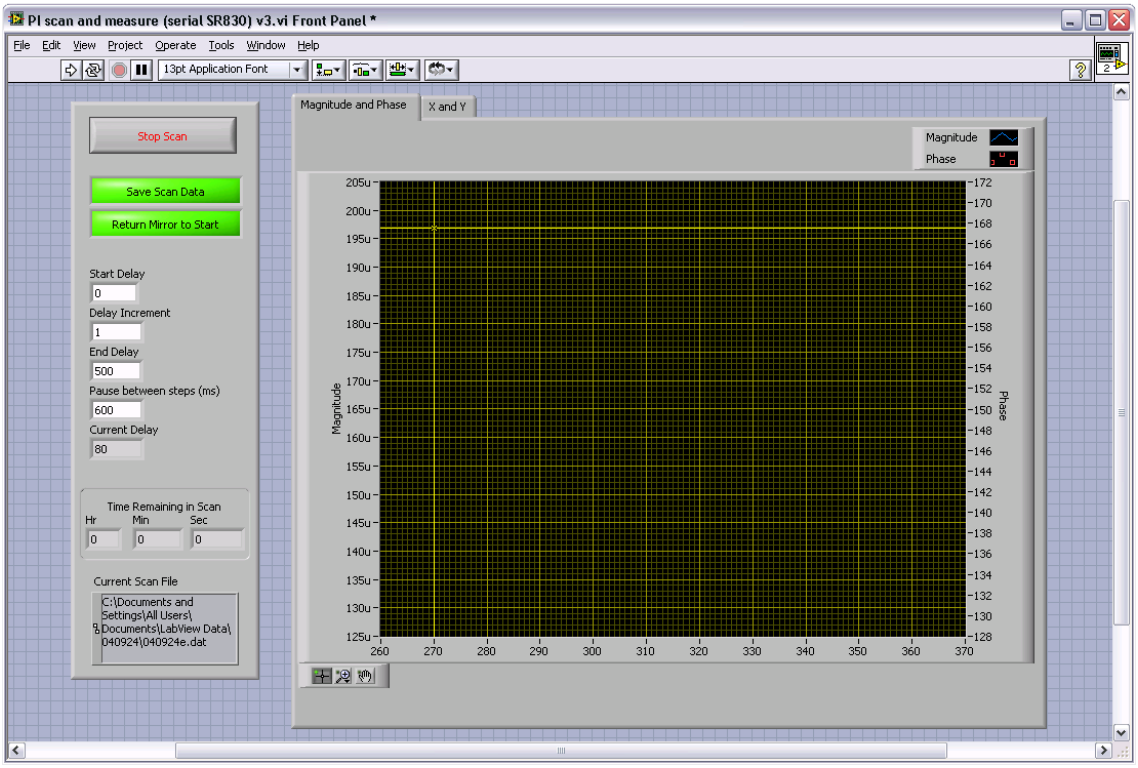

Figure 5.3: Screen capture of the user interface for the VI used to control the mechanical delay line and measure the Faraday rotation.

delay line is controlled via another RS-232 serial interface connected to the stepper motor. The VI controls the start delay, increment, end delay of the mechanical delay line. An adjustable value in the VI also controls how long the VI should wait after moving the retroreflector before reading the parameters from the lock-in amplifier. During our experiments the VI is set to wait 2000 ms to allow for sufficient settling time before taking a measurement.

During TRFR measurements the pump beam was adjusted to a power level of approximately 10 mW (measured before optically chopping the beam). The power

in the local arm and signal arm were adjusted to values of approximately 2 mW and 1 mW respectively. Transmission through the sample attenuates the signal arm by approximately one order of magnitude so that the power in the signal beam before recombination is about 100 μW. Thus the 2 mW in the local arm corresponds to a gain factor of approximately $\sqrt{20} = 4.5$. The wavelength of the laser was optimized during the experiment to maximize the TRFR signal. Typically the signal was optimized at a wavelength near 866 nm.

5.2.2 Optical Bridge

The optical bridge detection scheme is setup using the signal arm of the interferometer (Fig.5.4) so that the both schemes are as similar as possible. All that is required to setup the optical bridge is to remove the recombination cube, nPBS, from the beam path and block the local arm.

Instead of using a SRS SR830 to measure the Faraday rotation signal like in the interferometer setup, a Signal Recovery 7265 lock-in amplifier connected to the PC via GPIB is used instead. The 7265 lock-in amplifier was setup with a time-constant of 300 ms, a sensitivity of 2 mV, and a AC Gain of 30 dB and referenced at 509 Hz by the optical chopper chopping the pump beam during the TRFR measurements.

A LabVIEW VI similar to the one used for the interferometer is used to control the position of the delay line and read values from the lock-in amplifier. The VI,

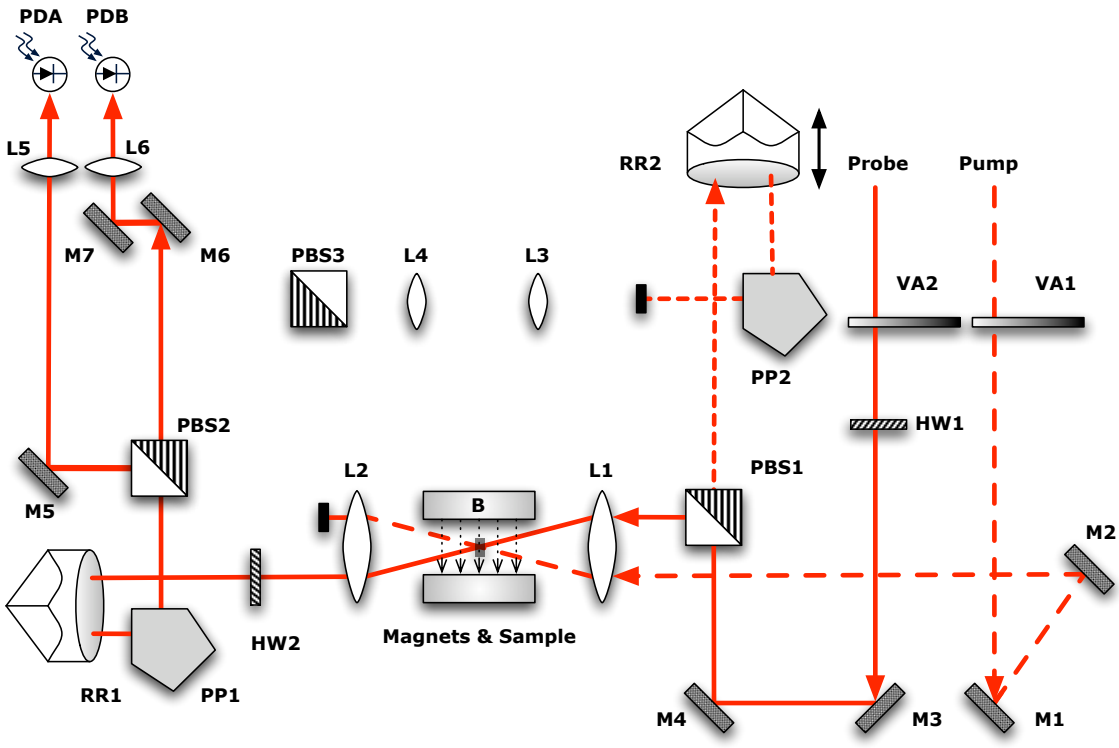

Figure 5.4: Schematic of the optical bridge setup built within the signal arm of the interferometer.

"traditional scan with ADC1 history.vi", is setup to wait 1000 ms after moving the retroreflector before measurement is taken. The delay, magnitude, theta, x, y, laser (through the ADC), and time are all recorded by the VI.

During the optical bridge measurements, values for the pump power, signal arm power and laser wavelength were similar to those used for the interferometer: 10 mW, 1 mW, and 866 nm respectively.

Chapter 6

Results and Analysis

6.1 Optical Amplification

To demonstrate passive optical amplification of Faraday rotation via interference with the local beam, the interferometer was setup nearly the same as it would be for TRFR measurements. However, the sample was removed and therefore the probe beam was optically chopped instead of the pump beam so that a lock-in measurement could still be made. Polarization rotation in the signal arm was achieved with the half-wave plate HW2.

According to Eq.2.19 the magnitude of the difference signal should increase linearly with the square-root of the power in the signal arm. The results for the optical amplification experiment do indeed show the expected linear trend (Fig.6.1). Imme-

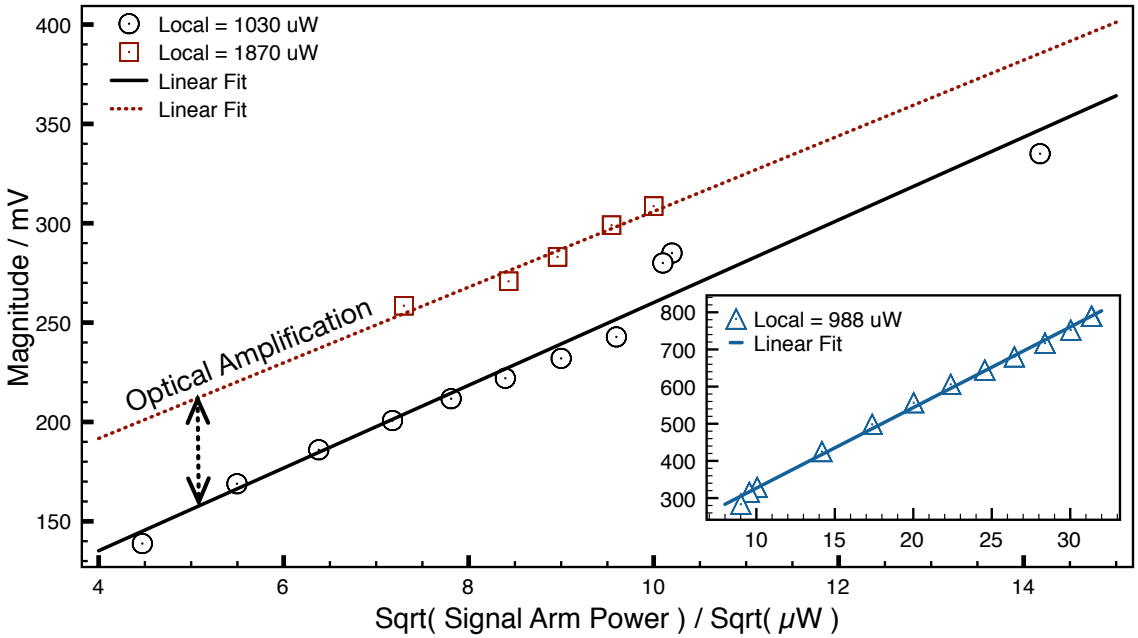

Figure 6.1: Demonstration of the expected linear relationship between the square root of the signal power and the difference signal at the photodiodes. The series within the sub-view was taken separately and thus the overlap of the two beams had changed slightly.

diately after taking the series with a local arm power of 1030 μW the power in the local arm was increased to 1870 μW and another series was taken. The sub-view shows data with a local arm power of 988 μW taken on a separate day, so it is not directly comparable to the other data due to variations in the quality of the beam overlap.

Since the arms of the interferometer are symmetric it will not matter which arm is held constant; the same linear relationship would exist if the signal arm were held constant and the local arm was increased instead.

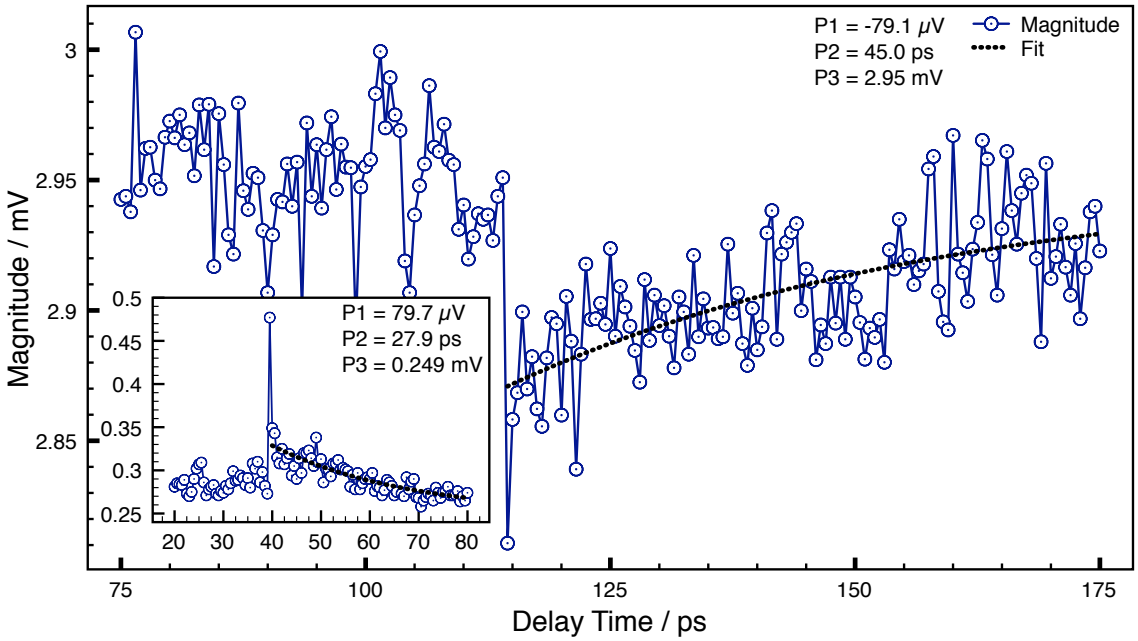

Figure 6.2: Sample TRFR signals taken with the interferometer and the optical bridge (insert).

6.2 Time-Resolved Faraday Rotation Measurements

Several TRFR measurements were taken using both the interferometric and optical bridge techniques. Care was taken so that nearly the same area on the sample was probed for each experiment so useful comparisons could be drawn. Typical TRFR signals for both the interferometer and optical bridge are shown in Fig.6.2.

Due to finite extinction ratios of the polarizing optics time-resolved absorption (TRA) could potentially affect the measured signal. However TRA increases transmission through the sample[30, 31] and thus has the opposite signal polarity of the signal shown for the interferometer (signal would increase). Any TRA component can

be observed separately with the interferometer by using a linearly polarized pump.

Each of the signals taken with either the interferometer or the optical bridge have been fitted with a decaying exponential function of the form $P_1 * e^{-t/P_2} + P_3$. Where P_2 is the effective spin lifetime of the signal (§1.1). The average fitting parameters for nine TRFR signals taken with the interferometer and four TRFR signals taken with the optical bridge are shown in Table 6.2. Pointing of the signal and pump beams was not changed during the interferometer or optical bridge measurements.

Technique	$\lvert P_1 \rvert$ / μ**V**	P_2 / **ps**	P_3 / **mV**	**RMS** / μ**V**
Interferometer	52.6 ± 14.9	31.2 ± 16.6	3.07 ± 0.27	31.9 ± 9.7
Optical Bridge	180 ± 67	10.9 ± 11.8	1.36 ± 0.88	125.2 ± 63.2

Table 6.1: Average fitting parameters for TRFR signals taken with the interferometer and with the optical bridge. Error values reported as one standard deviation.

Electron spin precession was not observed for any of the signals taken with either technique since the spin lifetimes ($P_2 \simeq 10 - 100$ ps) observed were too short for precession to take place (precession period of 0.65 ns). The observed spin lifetimes also fell short of what has been observed in the literature at room temperature (~ 1 ns).[16]

In general the TRFR signals measured with the optical bridge have stronger peaks, but shorter lifetimes. The difference signal is zeroed with the half-wave plate, HW1, before measurements are taken for the optical bridge leading to a smaller steady state value for the TRFR signals (P_3) than for the interferometer. Imperfections in

the interferometer analyzed in §2.2.1 will also contribute to the steady state value of the interferometer. The effective spin lifetimes (P_2) for each technique are within experimental error. Any large spikes in the signals, like those seen in Fig.6.2, were discounted from the fit. However, overall the optical bridge measurements did exhibit a stronger initial peak, due to interference between the pump and signal laser pulses on the sample at $\Delta t = 0$, which caused larger values of P_1 for the optical bridge. A larger sample size, and further tuning of the beam pointing during both sets of measurements, should eliminate this discrepancy between the two techniques.

The root mean square (RMS) values in Table 6.2 is calculated using Eq.6.1. This value is minimized by the fitting algorithm used on the data and quantifies the quality of the fit to the data. Overall the interferometer data contained more points than the optical bridge data, due to longer spin lifetimes, and finer delay increments.

$$RMS = \sqrt{\frac{1}{n}\sum_{i}^{n}(fit[i] - data[i])^2} \tag{6.1}$$

After fitting the data the signal-to-noise ratio of each of the TRFR measurements was calculated. First the fit function was subtracted from the data leaving only the noise. The signal-to-noise ratio can then be calculated using Eq.6.2 where $fit[i]$ is AC part of fit function (without P_3) taken at the times recorded in the experimental data, and $noise[i]$ is the steady-state value and noise. Calculating the signal-to-noise

ratio in this way removes the unimportant steady-state value, and provides a clearer picture of how strong the TRFR signal is compared to the noise. Average values for signal-to-noise ratio for TRFR signals taken with both the interferometer and the optical bridge are given in Table6.2.

$$S/N = 10 \log \left(\frac{\sum_i fit[i]^2}{\sum_i noise[i]^2} \right) \tag{6.2}$$

After removing the signal from the data the noise was analyzed. The noise mean, standard deviation and variance were all calculated. Values for the average values for these quantities for both the interferometer and the optical bridge are given in Table6.2.

Technique	**S/N / dB**	**Noise Parameters**		
		Mean / aV	Std. Dev. / μV	Var. / V^2 (10^{-9})
Interferometer	5.19 ± 4.54	-372 ± 614	14.0 ± 2.6	0.203 ± 0.083
Optical Bridge	4.80 ± 6.70	-28.2 ± 145	32.7 ± 16.6	1.28 ± 0.98

Table 6.2: Average values for the signal-to-noise ratio and parameters describing the noise distribution for TRFR signals taken with the interferometer and with the optical bridge. Error values reported as one standard deviation.

Taking the Faraday rotation detection limit to be three standard deviations of the noise the interferometer has a detection limit of approximately 50 mrad. This does not compare well with modern TRFR experiments using high-quality, quantum dot or epitaxial grown samples (ours were mechanical grade) at room temperature[16];

with cryogenic temperatures[19, 16] resolutions of 10 nrad can be reached. However, the interferometer offers better sensitivity than the optical bridge, which had a detection limit of 250 mrad, when both devices are operated in similar environments and experimental conditions. Optical amplification (gain factor of 4.5) accounts for the discrepancy in the sensitivity between the two devices.

Looking at the values presented it is clear that the interferometer is operating better than the optical bridge technique. The interferometer has a better signal-to-noise ratio than the optical bridge, and the noise distribution in the TRFR signals taken with the interferometer is more confined. Of course the interferometer had an advantage over the optical bridge technique since optical amplification from the interference with the 2 mW of power in the local arm was used to boost the signal slightly (a gain factor of $\sqrt{20} = 4.5$).

Overall our results bode well for the future of the interferometer as a useful device for TRFR experiments.

Detailed results for each of the analyzed signals are presented in Fig.6.3.

Interferometer

	Fit Parameters					Noise Parameters		
Signal	**P1 (V)**	**P2 (ps)**	**P3 (V)**	**Root Mean Square (V)**	**Signal to Noise (dB)**	**Mean (V)**	**Standard Deviation (V)**	**Variance (V^2)**
A	-4.933E-5	28.587	2.819E-3	3.302E-5	0.990	-2.273E-16	1.417E-5	2.007E-10
B	-4.442E-5	44.285	2.825E-3	2.372E-5	4.993	-1.369E-17	1.252E-5	1.567E-10
C	-3.178E-5	18.109	2.691E-3	2.292E-5	-2.068	-1.892E-15	1.731E-5	2.997E-10
D	-7.907E-5	45.016	2.949E-3	4.333E-5	7.486	-8.354E-17	1.957E-5	3.830E-10
E	-5.718E-5	17.346	3.060E-3	3.322E-5	3.967	-2.955E-18	1.341E-5	1.798E-10
F	-5.997E-5	34.896	3.262E-3	3.530E-5	10.154	-5.271E-17	1.206E-5	1.454E-10
G	-3.557E-5	13.960	3.246E-3	2.063E-5	3.123	-6.841E-16	1.314E-5	1.727E-10
H	-6.609E-5	61.609	3.297E-3	4.904E-5	12.861	-3.354E-18	1.154E-5	1.331E-10
I	-4.960E-5	15.951	3.482E-3	2.581E-5	5.197	-3.845E-16	1.255E-5	1.574E-10
Averages	-5.256E-5	31.084	3.070E-3	3.189E-5	5.189	-3.716E-16	1.403E-5	2.032E-10

Optical Bridge

	Fit Parameters					Noise Parameters		
Signal	**P1 (V)**	**P2 (ps)**	**P3 (V)**	**Root Mean Square (V)**	**Signal to Noise (dB)**	**Mean (V)**	**Standard Deviation (V)**	**Variance (V^2)**
A	7.967E-5	27.919	2.488E-4	3.926E-5	13.152	1.588E-17	9.975E-6	9.949E-11
B	2.075E-4	8.347	1.056E-3	1.308E-4	5.546	1.376E-16	3.432E-5	1.178E-9
C	-2.061E-4	5.099	1.989E-3	1.397E-4	3.668	-5.387E-17	3.646E-5	1.330E-9
D	-2.270E-4	2.042	2.135E-3	1.912E-4	-3.163	-2.126E-16	4.995E-5	2.495E-9
Averages	-3.648E-5	10.852	1.357E-3	1.252E-4	4.801	-2.823E-17	3.268E-5	1.276E-9

Figure 6.3: Detailed results for the TRFR signals analyzed and presented here.

Chapter 7

Discussion

The results presented in the previous section clearly demonstrate that we have been successful in building an interferometer that can passively optically amplify a Faraday rotation signal. Extensive work isolating the interferometer from noise sources and developing active computer stabilization (§3) was successful in reducing noise sources in the interferometer to a level that is comparable to what is seen in the traditional optical bridge detection scheme. In fact, our experiments show that the interferometer is able to resolve smaller Faraday rotations than the optical bridge; the interferometer's rotation resolution limit is 50 mrad, which is smaller than the 250 mrad resolution of the optical bridge. The difference in the sensitivity is accounted for by the optical gain factor of $\sqrt{20} = 4.5$ in the interferometer (§6.2).

Care was taken to operate both the optical bridge and interferometer under the

same environmental conditions and with the same GaAs samples so that useful comparisons could be drawn between the two techniques. The experiments were all performed at ambient temperatures and pressures and the same samples, which were of relatively poor quality, were used for testing both techniques. When the optical bridge technique is used on high-quality samples and the experiment is performed at cryogenic temperatures a resolution of 10 nrad can be achieved [19, 16]. Although we are far from achieving such small resolutions, the presented results demonstrate some promise that the interferometer can detect even weaker signals under similar conditions.

The interferometer was originally motivated by theoretical work [29] that considered the benefits of placing a quantum dot into a micro-cavity and measuring the Faraday rotation with an interferometer of the type presented here. It was theorized that such a device would be able to measure the Faraday rotation caused by a single electron spin on a semiconductor quantum dot. Our initial interest in examining the spin properties of novel quantum dot materials led us to investigate the interferometer as an unexplored method that could be used to increase the sensitivity of Faraday rotation detection non-invasively.

Measurement of single-electron spins on quantum dots contained within a micro-cavity using an optical bridge have recently been demonstrated [28, 27]. Use of a micro-cavity sample increases the rotation of the probe light's polarization axis by

an order of magnitude, which effectively increases the sensitivity of Faraday rotation detection. By placing the sample in an optical micro-cavity and performing the experiment with the interferometer at cryogenic temperatures with sophisticated detection equipment, including two lock-in amplifiers, it should be possible to achieve resolutions smaller than the optical bridge by an order of magnitude or two.

The optical gain factor is determined by the relative difference between the power in the local arm and signal arm. A significant advantage of the interferometer is that the optical gain factor effectively increases while the signal arm (probe) power is decreased and the local arm power is held constant. This characteristic of the interferometer will prove especially useful for low-power non-invasive experiments.

There are no fundamental, physical restrictions on the amount of optical amplification that can be achieved with the interferometer so resolutions that are even smaller than 0.1 nrad may be possible. Practically a detection limit is set by the detection equipment, namely the photodiodes. In our experiments we were limited to a maximum power of 2 mW in the local arm by the photodiodes and their difference amplifier. As the interferometer is pushed towards lower and lower resolutions tuning of the photodiodes will be necessary.

7.1 Future Directions

There are several directions available for future work on the interferometer. Possibly the most obvious step would be to acquire some high-quality samples. The samples we used produced measurable TRFR signals but were low-quality. With high-quality samples it would be possible to determine what resolutions can be achieved at ambient conditions; comparisons could then be drawn between published results for the optical bridge technique. Effort should also be made to determine to what extent optical amplification can be used at room-temperatures to strengthen the signal.

The analysis presented in §2.2.1 made it clear that higher quality polarizing optics and a nPBS with more ideal characteristics would also offer significant improvements.

Another obvious improvement would be to consider a more efficient stabilization scheme. There are several avenues to explore along this path including a more efficient stabilization algorithm, the current control-loop uses a simple error-amplifier. Implementation of a second, separately colored beam into the interferometer for active stabilization should also be considered since it would remove the coupling of the feedback signal and experimental signal mentioned earlier (§3.4). Fortunately dual-chromatic stabilization in laser interferometers has been implemented many times before and is well studied.

Currently the interferometer is setup to adapt to the use of a cryostat in the signal arm so that TRFR measurements can be made at cryogenic temperatures. It

is possible (perhaps likely) that the signal noise present with the interferometer does not scale with decreasing temperature in the same way as the optical bridge technique. If this were the case then the interferometer technique would not necessarily compete favorably with the optical bridge.

If it is determined that the interferometer cannot compete with the optical bridge technique at cryogenic temperatures there is still many interesting applications for new experiments. For example, instead of using the interferometer as a detection device the pump beam could be sent through the interferometer and recombined on a sample. By placing the two beams out of perfect overlap a variety of interference patterns could be created on the sample. This technique could be used to create many different spatially varied excitation profiles on the sample. Interesting spin-dynamics and interactions between neighboring fringes could then be studied.

Regardless of the next step taken there is a lot of opportunity for the interferometer presented here. Now that the initial challenges with the design of this device have been met, the more interesting work of testing its limits and exploring useful applications can begin.

Bibliography

[1] M. N. Baibich, J. M. Broto, A. Fert, F. Nguyen Van Dau, F. Petroff, P. Eitenne, G. Creuzet, A. Friederich, and J. Chazelas. Giant magnetoresistance of (001)fe/(001)cr magnetic superlattices. *Physical Review Letters*, 61(21):2472–2475, Nov 1988.

[2] C. Carbone and S. F. Alvarado. Antiparallel coupling between fe layers separated by a cr interlayer: Dependence of the magnetization on the film thickness. *Physical Review B*, 36(4):2433–2435, Aug 1987.

[3] P. Grünberg, R. Schreiber, Y. Pang, M. B. Brodsky, and H. Sowers. Layered magnetic structures: Evidence for antiferromagnetic coupling of fe layers across cr interlayers. *Physical Review Letters*, 57(19):2442–2445, Nov 1986.

[4] L. L. Hinchey and D. L. Mills. Magnetic properties of superlattices formed from ferromagnetic and antiferromagnetic materials. *Physical Review B*, 33(5):3329–3343, Mar 1986.

[5] S. A. Wolf, D. D. Awschalom, R. A. Buhrman, J. M. Daughton, S. von Molnar, M. L. Roukes, A. Y. Chtchelkanova, and D. M. Treger. Spintronics: A spin-based electronics vision for the future. *Science*, 294(5546):1488–1495, 2001.

[6] David D. Awschalom and Michael E. Flatte. Challenges for semiconductor spintronics. *Nature Physics*, 3(3):153–159, 2007.

[7] J. J. Baumberg, D. D. Awschalom, and N. Samarth. Femtosecond faraday-rotation in spin-engineered heterostructures. *Journal of Applied Physics*, 75(10):6199–6204, May 1994.

[8] J. M. Kikkawa and D. D. Awschalom. Lateral drag of spin coherence in gallium arsenide. *Nature*, 397:139–141, Jan 1999. 10.1038/16420.

[9] F. Meier and B. P. Zakharchenya, editors. *Optical Orientation*. Elsevier, Amsterdam, 1984.

[10] J. S. Blakemore. Semiconducting and other major properties of gallium arsenide. *Journal of Applied Physics*, 53(10):R123–R181, 1982.

[11] B. P. Zakharchenya, D. N. Mirlin, V. I. Perel', and I. I. Reshina. Spectrum and polarization of hot-electron photoluminescence in semiconductors. *Soviet Physics - Uspekhi*, 25(3):143–166, 1982.

[12] Pil Hun Song and K. W. Kim. Spin relaxation of conduction electrons in bulk iii-v semiconductors. *Physical Review B*, 66(3):035207, Jul 2002.

[13] R. I. Dzhioev, K. V. Kavokin, V. L. Korenev, M. V. Lazarev, B. Ya. Meltser, M. N. Stepanova, B. P. Zakharchenya, D. Gammon, and D. S. Katzer. Low-temperature spin relaxation in n-type gaas. *Physical Review B*, 66(24):245204, Dec 2002.

[14] J. Wagner, H. Schneider, D. Richards, A. Fischer, and K. Ploog. Observation of extremely long electron-spin-relaxation times in p-type $\delta-dopedgaas/\mathrm{al}_x ga_{1-x}\mathrm{as}$ double heterostructures. *Physical Review B*, 47(8):4786–4789, Feb 1993.

[15] J M Kikkawa and D D Awschalom. Resonant spin amplification in n-type gaas. *Physical Review Letters*, 80(19):4313–4316, May 1998.

[16] J. M. Kikkawa, I. P. Smorchkova, N. Samarth, and D. D. Awschalom. Room-temperature spin memory in two-dimensional electron gases. *Science*, 277(5330):1284–1287, 1997.

[17] J. M. Kikkawa, J. A. Gupta, I. Malajovich, and D. D. Awschalom. Spin coherence in semiconductors: storage, transport and reduced dimensionality. *Physica E: Low-dimensional Systems and Nanostructures*, 9(1):194–201, 2001.

[18] Eugene Hecht. *Optics (4th Edition)*. Addison Wesley, 2001.

[19] A. Kanno and Y. Masumoto. Spin relaxation mechanism of strain-induced gaas quantum dots studied by time-resolved kerr rotation. *Physical Review B*, 73, FEB 2006.

[20] N. P. Stern, M. Poggio, M. H. Bartl, E. L. Hu, G. D. Stucky, and D. D. Awschalom. Spin dynamics in electrochemically charged cdse quantum dots. *Physical Review B*, 72, OCT 2005.

[21] V N Golovach and D Loss. Electron spins in artificial atoms and molecules for quantum computing. *Semiconductor Science and Technology*, 17:355–366, March 2002.

[22] D Loss and D P DiVincenzo. Quantum computation with quantum dots. *Physical Review A*, 57(1):120–126, January 1998.

[23] J. A. Gupta, D. D. Awschalom, Al. L. Efros, and A. V. Rodina. Spin dynamics in semiconductor nanocrystals. *Physical Review B*, 66(12):125307, Sep 2002.

[24] J. A. Gupta, D. D. Awschalom, X. Peng, and A. P. Alivisatos. Spin coherence in semiconductor quantum dots. *Physical Review B*, 59(16):R10421–R10424, Apr 1999.

[25] R. Hanson, L. P. Kouwenhoven, J. R. Petta, S. Tarucha, and L. M. K. Vandersypen. Spins in few-electron quantum dots, 2006.

[26] J Preskill. Reliable quantum computers. *Proceedings: Mathematical, Physical and Engineering Sciences*, 454(1969):385, January 1998.

[27] Y. Q. Li, D. W. Steuerman, J. Berezovsky, D. S. Seferos, G. C. Bazan, and D. D. Awschalom. Cavity enhanced faraday rotation of semiconductor quantum dots. *Applied Physics Letters*, 88, MAY 8 2006.

[28] J. Berezovsky, M. H. Mikkelsen, O. Gywat, N. G. Stoltz, L. A. Coldren, and D. D. Awschalom. Nondestructive Optical Measurements of a Single Electron Spin in a Quantum Dot. *Science*, 314(5807):1916–1920, 2006.

[29] Mitsuro Sugita, Susumu Machida, and Yoshihisa Yamamoto. Quantum nondemolition measurement of a single electron spin in a quantum dot, 2003.

[30] C. V. Shank, R. L. Fork, R. F. Leheny, and Jagdeep Shah. Dynamics of photoexcited gaas band-edge absorption with subpicosecond resolution. *Physical Review Letters*, 42(2):112–115, Jan 1979.

[31] J. J. Baumberg, S. A. Crooker, D. D. Awschalom, N. Samarth, H. Luo, and J. K. Furdyna. Ultrafast faraday spectroscopy in magnetic semiconductor quantum structures. *Physical Review B*, 50(11):7689–7700, Sep 1994.

Appendix A

Operation of Polarization Interferometer

A.1 General Alignment Procedures

Before proceeding with the alignment procedure it is important to overview several methods that will be employed throughout the alignment.

A.1.1 Mirror Alignment

The screw holes on the optics table provide a convenient grid to follow during beam alignment. Alignment of the optics along the table is eased considerably if effort is made to direct the beam parallel to theses gridlines.

1. Note the gridline that is closest to the reflected beam.

2. Place a marker (a beam block covered with graph paper will suffice) near the mirror insuring that the base of marker is at some identifiable and repeatable position on the grid.

3. Note the position of the reflected beam on the marker.

4. Position the marker at another spot that is translated along the gridline as far away from the mirror as possible.

5. Use the tilt controls of the mirror direct the beam onto the same spot on the marker as previously noted in 3.

6. Repeat steps 2 - 5 until the beam is at the same position on the marker regardless as to where it is positioned along the gridline.

A.1.2 Normalizing an Incident Beam with Back Reflections

To quickly determine if a beam is incident normal to the surface of a glass optic check the back reflection coming off the optic.

1. Center an iris on the beam further up the beam path away from the optic.

2. Close the iris so that a small but significant amount of the beam continues to propagate through the iris. Practice will provide you with a sense of how much

light to allow through the iris.

3. Now adjust the tilt of the optic so that the back reflection is centered on the back of the iris.

4. The beam is now normal to the surface of the optic.

A.1.3 Lens Collimation

The following procedure is used for collimating a beam using two plano-convex singlet or achromatic doublet lenses. Such a system is normally used to expand, reduce, and/or spatially filter the beam.

1. Before placing a lens in the beam path use mirrors to create several meters for which the beam can travel. It is likely that the beam will have to be bounced back and forth several times along the same section of the optics table.

2. Place a beam block approximately two focal lengths away from the location of the second lens. Note the location of the beam on the block.

3. Place the second lens inside the beam path with the plano side facing the beam. The side of the lens facing the beam is important to maximize refraction in the system and create the best focus. Adjust the height and position of the lens until the beam is incident on the block at the same location it was before the lens was in place.

4. Check the back reflection from the lens to ensure that the beam is centered on the lens and that the optical axis of the lens is collinear with the beam. (A.1.2)

5. Repeat steps 3 and 4 until the lens is properly positioned in the beam path.

6. Now place the first lens in the beam path with the convex side facing the beam. Follow the same procedure for positioning the first lens to position the second.

7. Use a beam block (a business card will do) and check the shape and size of the beam at the exit of the lens system.

8. Compare the shape and size of the beam after several meters of propagation with the shape and size after the lens system.

9. Adjust the distance between the two lenses until the beam shape and size is relatively constant for several meters after the two lens system.

A.2 Interferometer Alignment

Begin the alignment of the interferometer with the probe beam. After the probe beam is properly aligned the pump beam is easily directed onto the sample and overlap between the probe and pump can be achieved.

It is important to have beam blocks with graph paper on them to compare beam positions. Several irises are also useful for alignment.

Use Fig. A.1 as a reference while following the alignment procedures below.

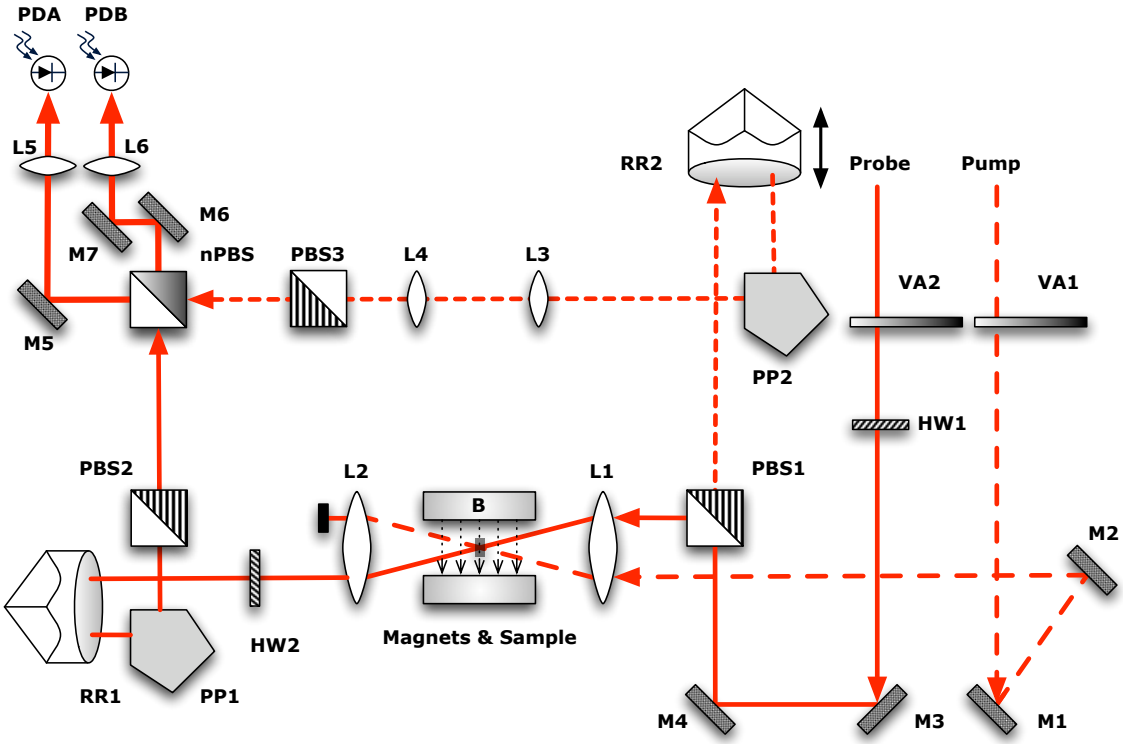

Figure A.1: The signal arm of the interferometer is indicated by a solid beam, whereas the local arm beam path is traced by a short dashed line. Lens pairs L1 and L2, as well as L3 and L4 are matched and form 1x beam collimators. VA = Variable Attenuator. HW = Half wave plate. M = Mirror. L = Lens. PP = Penta Prism. RR = Retroreflector. PBS = Polarizing Beamsplitting Cube. nPBS = non-Polarizing Beamsplitting Cube. PD = Photodiode. Further specification found in Appendix B.

A.2.1 Probe Beam Alignment

1. Ensure that the probe beam is parallel to a gridline while propagating towards mirror M3.

2. Place the variable attenuating wheel VA2 in the beam path. Check the back reflection from the wheel using the procedure found at A.1.2 to ensure that the beam is normal to the surface of VA2.

3. Place the half-wave plate HW1 in the beam path. Check the back reflection from the half-wave plate using the procedure found in A.1.2 to ensure that the beam is normal to the surface of HW1.

4. Using mirror M3 direct the beam at a right angle towards mirror M4. If necessary use M3 to direct the beam up or down so after mirror M4 the beam will propagate horizontal to the table at the height of the optics in the interferometer (typically around six inches).

5. Place M4 in the beam path and align the reflected beam so that it is level with the table surface and follows one of the gridlines on the table referenced by the screw hole placement. Refer to A.1.1 for assistance.

6. Mount PBS1 on a three-axis tilt stage and position it in the beam path. Follow the procedure in A.1.2 to ensure that the beam is incident normal to the surface of the cube.

7. Use the procedure for mirror alignment in A.1.1 to ensure that the reflected beam from the cube is parallel to the gridlines on the optics table. This may cause the back-reflection to deviate slightly.

8. Mount L1 and L2 on three-axis translation stages and use the procedure found in A.1.3 to position L1 and L2.

9. Translate L1 and L2 the same distant perpendicular to the local beam so that there is room for the pump beam to travel past cube PBS1 and be focused on the sample with lens L1. Typically this is about half an inch.

10. Position HW2 in the beam path and ensure that it the beam is incident normal to its surface using the procedure in A.1.2.

11. Mount the retroreflector RR1 onto a translation stage that allows you to adjust its height and position it in front of the beam.

12. Mount the penta prism (PP1) on a stage with three-axis tilt controls and position it in the beam path. Check the back reflections using the procedure in A.1.2 to ensure that the beam is incident normal to the surface of the penta prism and also adjust the tilt controls so that the reflected beam is still horizontal to the table.

13. Mount the polarizing beam splitting cube PBS2 on a mount with three-axis tilt control and place it in the beam path. Check the back reflection using the procedure in A.1.2 to ensure that the laser beam is incident normal to the beamsplitter.

14. Mount the retroreflector RR2 onto a translation stage with the piezoelectric actuator installed in front of the beam in the local arm. It is not necessary for the mount to allow vertical translation of the retroreflector as it was in the signal arm.

15. Mount the penta prism PP2 on a stage with three-axis tilt controls and position it in the beam path. Check the back reflections using the procedure in A.1.2 to ensure that the beam is incident normal to the surface of the penta prism and also adjust the tilt controls so that the reflected beam is still horizontal to the table.

16. Mount L3 and L4 on three-axis translation stages and use the procedure found in A.1.3 to position L1 and L2. (Note: Three-axis translation stages are not necessary for L3, L4 but will provide finer position control than other mounting solutions.)

17. Mount the polarizing beam splitting cube PBS3 on a mount with three-axis tilt control and place it in the beam path. Check the back reflection using the procedure in A.1.2 to ensure that the laser beam is incident normal to the beamsplitter.

18. Before positioning the non-polarizing beam splitter in the beam path use a beam block and check that the local and signal beams are overlapped. If the

two beams are at different heights use the vertical control on RR1 to move the signal beam to overlap the local beam.

19. Position mirror M5 in the path of the local beam and tilt the mirror so that the beam is reflected at a right-angle and is parallel to the gridlines on the table using the procedure found at A.1.1.

20. Connect the photodiode box to an oscilloscope and position the box in the path of the local beam so that the signal is maximized on the scope.

21. Position lens L5 in the beam path. Adjust the position of the lens to maximize the signal on the oscilloscope. Use the procedure at A.1.2 to ensure that the optical axis of the lens and the beam are collinear.

22. Use mirrors to send the signal beam along a path length of several meters. The overlap of the signal and local beams will be monitored at this far-field location to optimize the position of the non-polarizing beam splitter.

23. Mount the non-polarizing beam splitter, nPBS, on a three-axis tilt mount installed with actuators for fine control over the rotation of the tilt stage. The stage should itself be mounted on a linear, one-axis, translation stage so that the nPBS can be moved along the path of either the signal or local beam. Place the nPBS in the beam path. Check the back reflections in both the signal and

local arm using the procedure at A.1.2. It will not be possible to perfectly position the back reflections in both arms since the nPBS is not perfectly cubic.

24. Put the laser in continuous mode. Since the path lengths of the two arms are likely not matched at the moment the laser must be in continuous mode to detect an interference signal.

25. Adjust the tilt controls for the nPBS stage so that both the signal and local beam are at the same height before lens L5 and in the far-field setup in Step 22.

26. Iterate between translating the nPBS along the beam path with the linear translation stage and the rotation control on the tilt stage to overlap the signal and local beams before lens L5 and in the far-field.

27. Repeat 25 and 26 until the interference pattern is optimized. The interference lines will converge to encompass the whole beam waist when the two beams are optimally overlapped. Refer to Fig.A.2 for sketch of the changes in the interference pattern as the beam overlapped is optimized.

28. Block the local arm. Install mirrors M6 and M7 to direct the beam onto photodiode PDB. Use an oscilloscope to assist in optimizing the position of the beam.

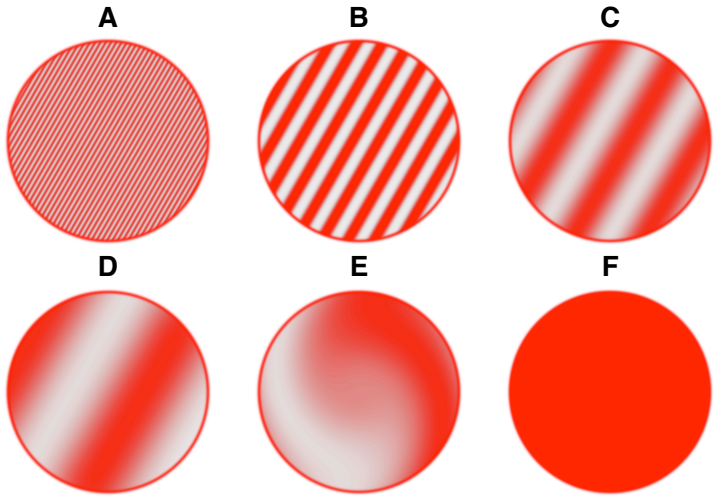

Figure A.2: Figures A through F are rough sketches of how the interference pattern changes as the beam overlap is optimized. In general the linear fringes will become wider, until one fringe begins to dominate the entire beam waist as in E. Minor tweaks will then allow most, but not all, of the beam waist to be either lit similar to the beam waist shown in F, or darkened (not shown) depending on the phase difference between the two arms.

29. Position lens L6 in the beam path. Adjust the position of the lens to maximize the signal on the oscilloscope. Use the procedure at A.1.2 to ensure that the optical axis of the lens and the beam are collinear.

30. Connect the oscilloscope to the difference channel PDA-PDB.

31. Mode-lock the laser.

32. Move RR2 along the beam path using the course linear stage to equalize the path length of both the local and signal arm. When this occurs an autocorrelation trace will appear on the oscilloscope as RR2. Several such traces may be found. In general the strongest autocorrelation trace will be the correct one and it should occur when the RR2 is closest to to PP2. Other autocorrelations signals are caused by back reflections bouncing within the interferometer.

33. If an autocorrelation signal cannot be found within the range of the translation stage holding RR2 and the local and signal arms are correctly overlapped the stage may have to be moved manually along the table surface and mounted at a different location. When doing this be careful to move the mount parallel to the gridlines on the table, and therefore the beam line. Use a straight edge to assist in making a translation of the stage.

34. Once the proper autocorrelation signal has been found position RR2 in the center of the trace.

35. While tapping the mount holding RR2 or moving RR2 by oscillating it through several wavelengths of the laser (800-900 nm) with the piezoelectric actuator maximize the peak-to-peak voltage difference of the difference signal on the scope by adjusting the tilt controls for the nPBS, the linear stage holding the nPBS stage, and by adjusting the vertical position of RR1.

None of the beam splitting cubes are perfectly cubic. The imperfections in the cubes cause unwanted distortions in the direction of transmitted and reflected beams. If the autocorrelation trace is weak after performing the alignment procedure attempt using a different face of a cube where possible, or flip them to achieve better results. The difference that this can make is surprisingly dramatic, with an order of magnitude increase in the peak-to-peak voltage of the autocorrelation trace possible.

A.2.2 Pump Beam Alignment

1. Ensure that the pump beam is parallel to a gridline while propagating towards mirror M1.

2. Place the variable attenuating wheel VA1 in the beam path. Use the procedure at A.1.2 to insure that the beam is normal to the surface of VA2.

3. Place mirror M1 in front of the beam.

4. Mount mirror M2 on a two-axis translation stage and place it in an appropriate

spot. Direct the beam with mirror M1 onto mirror M2. Make any necessary height adjustments to the beam using mirror M1 to angle the beam up or down.

5. Adjust the tilt controls on mirror M2 so that the beam is horizontal to the table and parallel to on of the gridlines. Refer to A.1.1 for assistance.

6. Translate mirror M2 as needed to position the pump beam as close to the edge of cube PBS1 as possible.

7. Block the pump beam.

8. Mount a pinhole on three-axis translation stage and position the pinhole at the focus of lens L1.

9. Unblock the pump beam and make minor adjustments to the tilt of mirror M2 so that the pump beam passes through the pinhole. The beams are now overlapped.

A.3 Daily Operation

Refer to the schematic of the interferometer in Fig.A.1 as needed.

1. To begin remove the sample so that both the signal beam and pump beam are traveling through free space.

2. Adjust the half-wave plate HW1 and variable attenuator wheel VA1 to achieve the desired level of power in the signal and local beams. Record the power levels of the local and signal beams.

3. Monitor the difference signal between photodiodes PDA and PDB while scanning retroreflector RR2 along its translation stage to determine the center of the autocorrelation trace.

4. Use the tilt controls on the mount of the non-polarizing beam splitting cube to optimize the amplitude of the autocorrelation trace. Also adjust the one-axis translation stage that the nPBS is mounted on and the height of retroreflector RR1 to achieve the strongest autocorrelation signal. Record the optimized amplitude of the autocorrelation signal.

5. Place the sample in the local beam path and optimize the probe and pump beam overlap on the sample using mirror M2.

6. Check the amplitude of the autocorrelation signal again and repeat Step 4 if necessary.

Appendix B

Optics Specifications for Polarization Interferometer

The component list for the polarization interferometer relative to the schematic in Fig.A.1 and reprinted here for convenience. Refer to Chapter 3 for a complete discussion of components and their function.

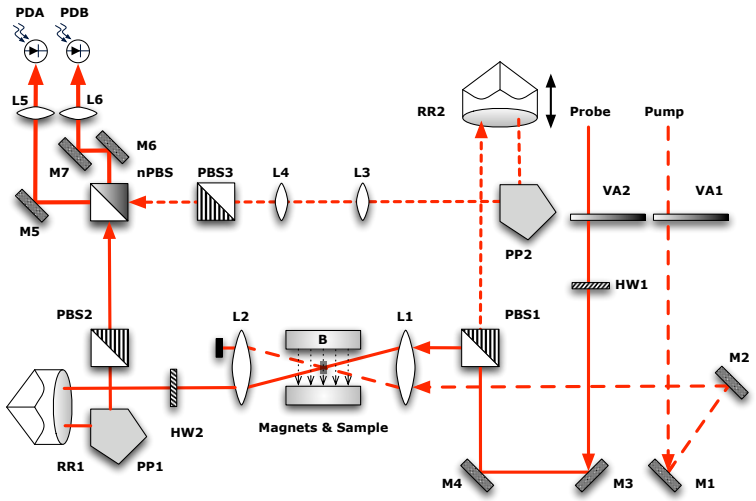

Figure B.1: Schematic of the polarization interferometer.

Components L1, L2:	**Achromatic doublet lens**
Manufacturer:	Newport
Part number:	PAC086
Diameter:	50.8 mm
Effective focal length:	150 mm
$f/\#$:	3.0
Clear aperture:	>central 90% of diameter
Surface flatness:	$< \frac{\lambda}{4}$ at 632.8 nm over clear aperture
Material:	BK 7-SF 5

Components L3, L4:	**Plano-convex singlet lens**
Manufacturer:	Melles Griot
Part number:	01 LPX 175
Diameter:	25.4 mm
Paraxial focal length:	100 mm
Clear aperture:	22.5 mm
Material:	BK7 Glass
Components PP1, PP2:	**Penta prisms**
Manufacturer:	Newport
Part number:	BPP-25.4
Aperture:	25.4 mm x 25.4 mm
Beam deviation:	$90^\circ \pm 30$ arc sec
Clear aperture:	Central diameter, >85% of dimension
Surface flatness:	$< \frac{\lambda}{4}$ at 632.8 nm over clear aperture
Material:	BK7 Glass

Components RR1, RR2:	**Hollow retroreflector**
Manufacturer:	Newport
Part number:	UBBR1
Wavefront distortion:	$< \frac{\lambda}{3}$ at 632.8 nm over clear aperture
Parallelism:	5 arc sec
Coating:	Protected gold
Components PBS1, PBS2, PBS3:	**Polarizing cube beamsplitter**
Manufacturer:	Newport
Part number:	10FC16PB.5
Dimensions:	25.4 mm^3
Wavefront distortion:	$< \frac{\lambda}{4}$ at 632.8 nm over clear aperture
Clear aperture:	>80% of dimensions
Efficiency:	Tp ¿ 80%, ¿90% average, Rs ¿ 99.5% average
Extinction ratio:	Tp/Ts >500:1, 1000:1 average
Transmitted beam deviation:	<5 arc min
Reflected beam deviation:	$90^\circ \pm 5$ arc min
Material:	SF 2, NSSK grade, precision annealed optical glass

Component nPBS:	**Non-polarizing beamsplitter cube**
Manufacturer:	Thorlabs
Part number:	BS014
Dimensions:	25.4 mm^3
Flatness:	$\frac{\lambda}{10}$ from 700nm to 1100nm
Clear aperture:	>90% of dimensions
Splitter ratio tolerance:	<15% over entire wavelength range
	|Ts-Tp |<15% and |Rs-Rp |<15%
Transmitted beam deviation:	<5 arc min
Reflected beam deviation:	90°± 5 arc min
Material:	BK7 grade A glass
Component HW1:	**Half-wave plate**
Manufacturer:	CVI
Part number:	QWPM-800-10-2-R115
Diameter:	25.4 mm
Wavefront distortion:	$\frac{\lambda}{10}$ at 633 nm
Parallelism:	<0.5 arc sec
Material:	Crystal quartz

Component HW2:	**Half-wave plate**
Manufacturer:	Thorlabs
Part number:	WPH05M-808
Diameter:	12.7 mm
Wavefront distortion:	$\frac{\lambda}{10}$ at 808nm
Parallelism:	<10 arc sec
Material:	Crystal quartz
Components M1-M7:	**Protected silver mirror**
Manufacturer:	Newport
Part number:	10D10ER.2
Diameter:	25.4 mm
Surface flatness:	$\frac{\lambda}{10}$ from 480nm to 1100nm
Clear aperture:	>80% of central diameter

Components VA1, VA2:	**Continuously variable metallic neutral density filters**
Manufacturer:	Thorlabs
Part number:	NDC-100C-2
Diameter:	4.5 inches
Spectral range:	380-1200 nm
Irregularity (per cm^2):	$< \lambda$
Optical density:	0 - 2.0
Substrate:	UV fused silica

Appendix C

Protective Acoustical Dampening Box

C.1 Box Design

The acoustical dampening box was designed to provide a sturdy, rigid enclosure for the interferometer. The box was meant to eliminate air flow over the interferometer, reduce acoustical vibrations, and block stray light from being detected at the photodiodes.

Particle board was used to create the roofing and side panels of the box since it is suitable as an acoustical dampening material, and it was readily available as a sturdy building material. The box dimensions are $38\frac{1}{4}'' \times 54\frac{1}{4}'' \times 13\frac{3}{4}''$ (W x L x H). There is

enough room in the enclosure to contain all the optics and mounts with some room for future expansion. The ceiling is $9\frac{1}{4}''$ tall so there is not any danger of any of the optical mounts being inadvertently bumped when installing the roof panels.

The box is constructed with a series of removable side panels that are held in place by aluminum posts $1''$ in diameter. The bottom of the posts have a cylindrical cavity that slides alignment screws positioned on the optics table. The use of alignment screws allows the posts to be positioned on the table and rotated so that they are in the proper orientation. A set screw in the base of the post keeps the posts from rotating once they have been aligned. The side panels are positioned with an attached acrylic edge that is slid down a milled grove in the posts. Once the panels are in place aluminum brackets attach each panel to its two neighbors. The brackets are necessary to increase the stability of the walls. The box lid is composed a framing piece and four removable panels that allow easy access to the sections of the interferometer.

One side-panel is made to accommodate a piece of inset glass that is held in place with an adhesive and sealant. Laser light can then enter the interferometer and the box continues to block unwanted air currents. The $\frac{1}{4}''$ thick glass panel used in the box is not made of any special optical material.

Any wires needed for electrical connections inside the box are passed under one of the panels. A small slit at the bottom of a panel is created, but the foam is left in place to create a seal around the wire.

The following drawings provide details on the geometry of the box and its components.

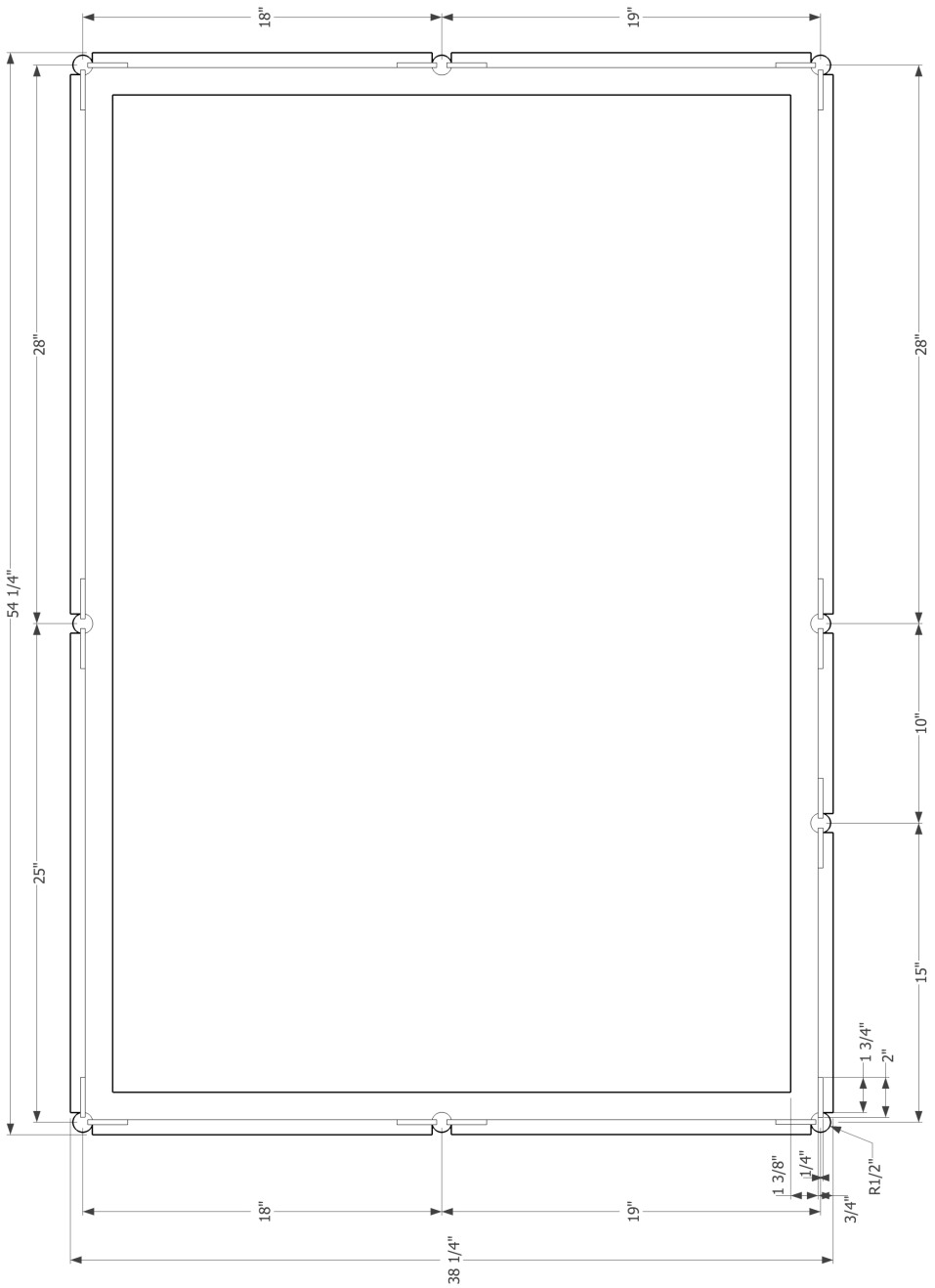

Figure C.1: Top view of the box with acoustical foam lining the interior of the walls.

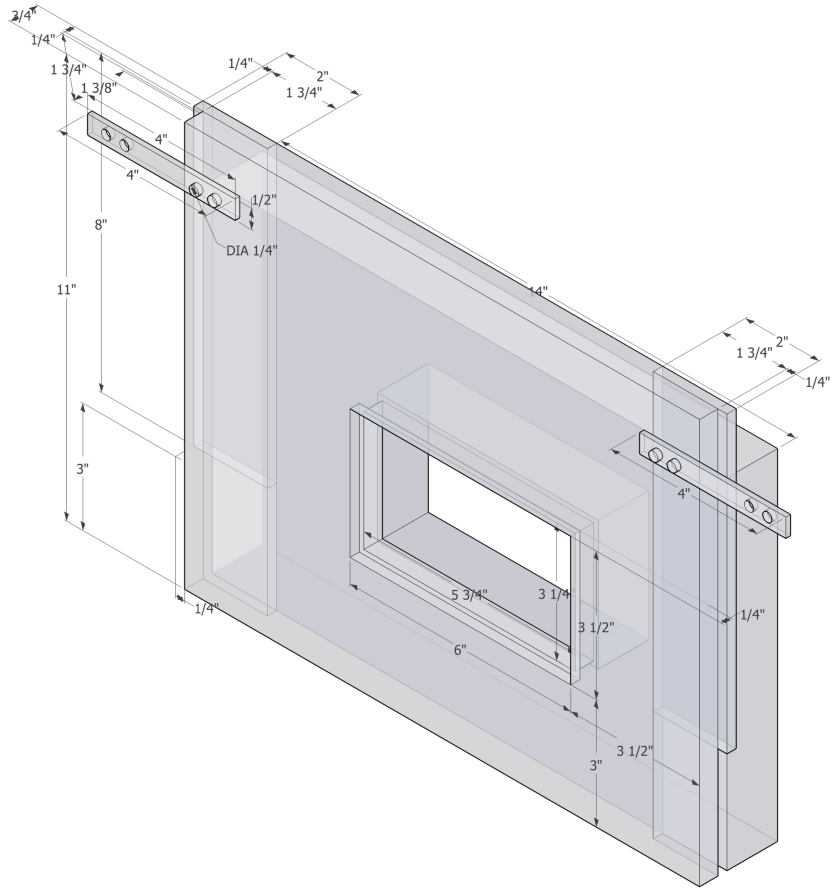

Figure C.2: Three dimensional perspective of the window side panel with foam attached. The other panels are similarly fashioned.

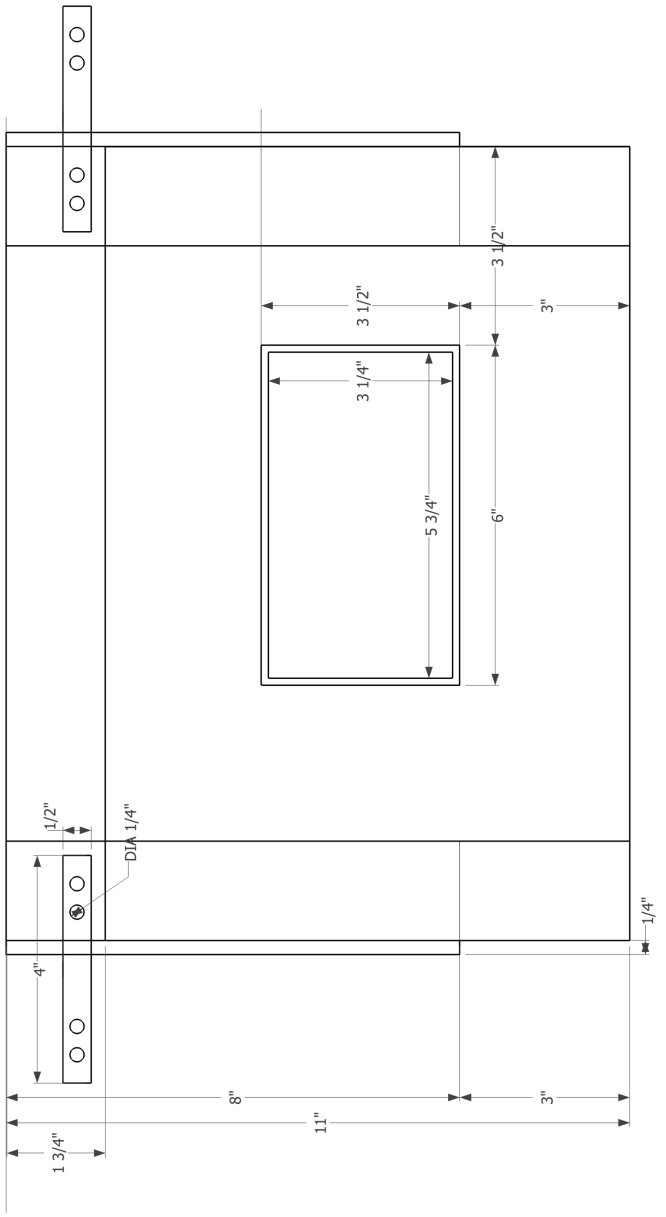

Figure C.3: Front view of the window side panel with foam attached. The other panels are similarly fashioned.

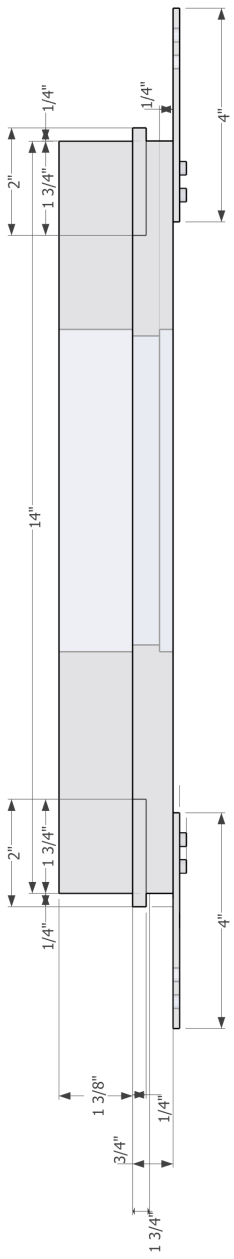

Figure C.4: Top view of the window side panel with foam attached. The other panels are similarly fashioned.

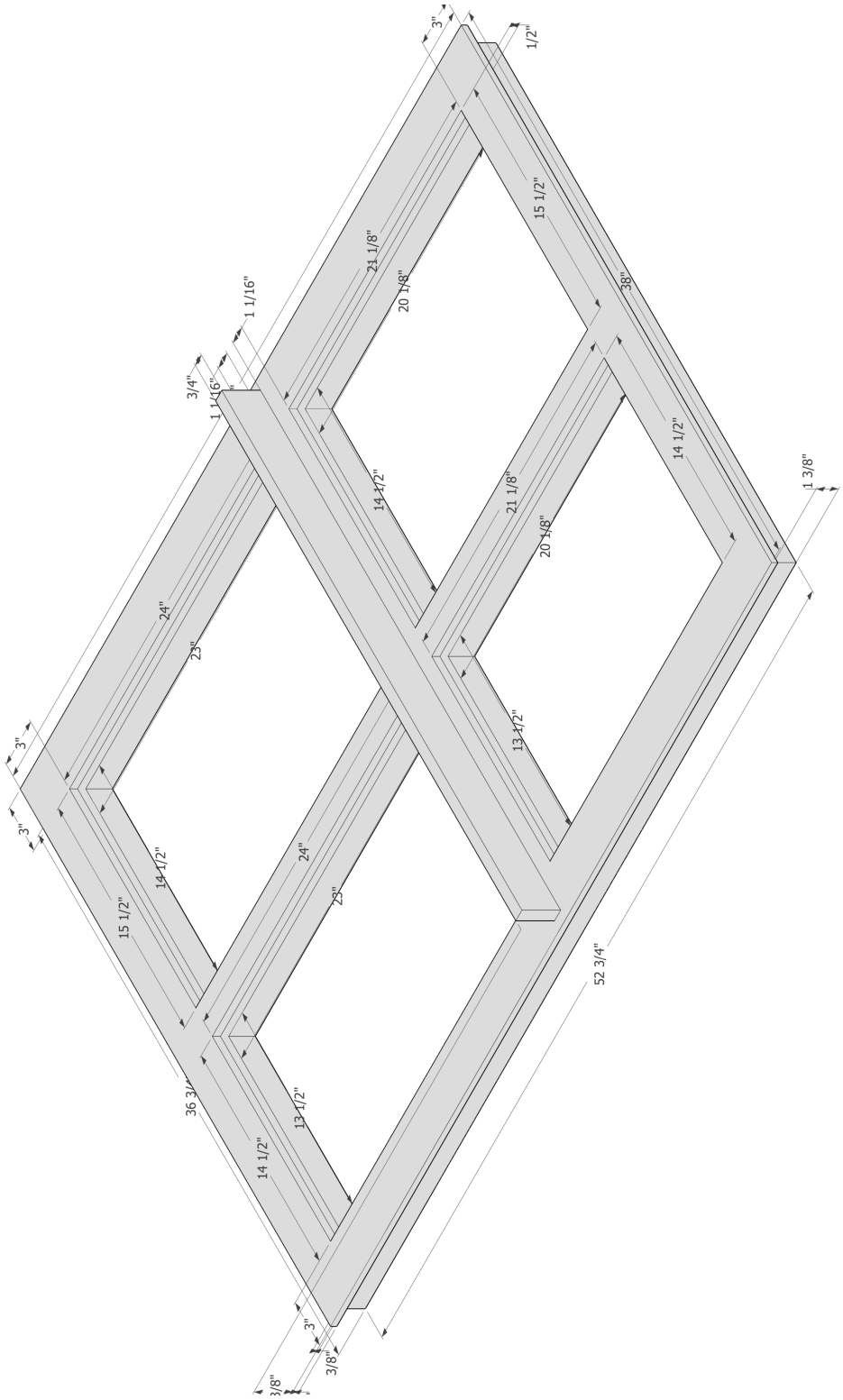

Figure C.5: Three dimensional perspective of the box lid with foam attached.

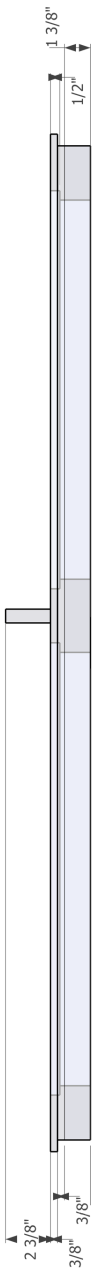

Figure C.6: Front view of the box lid with foam attached.

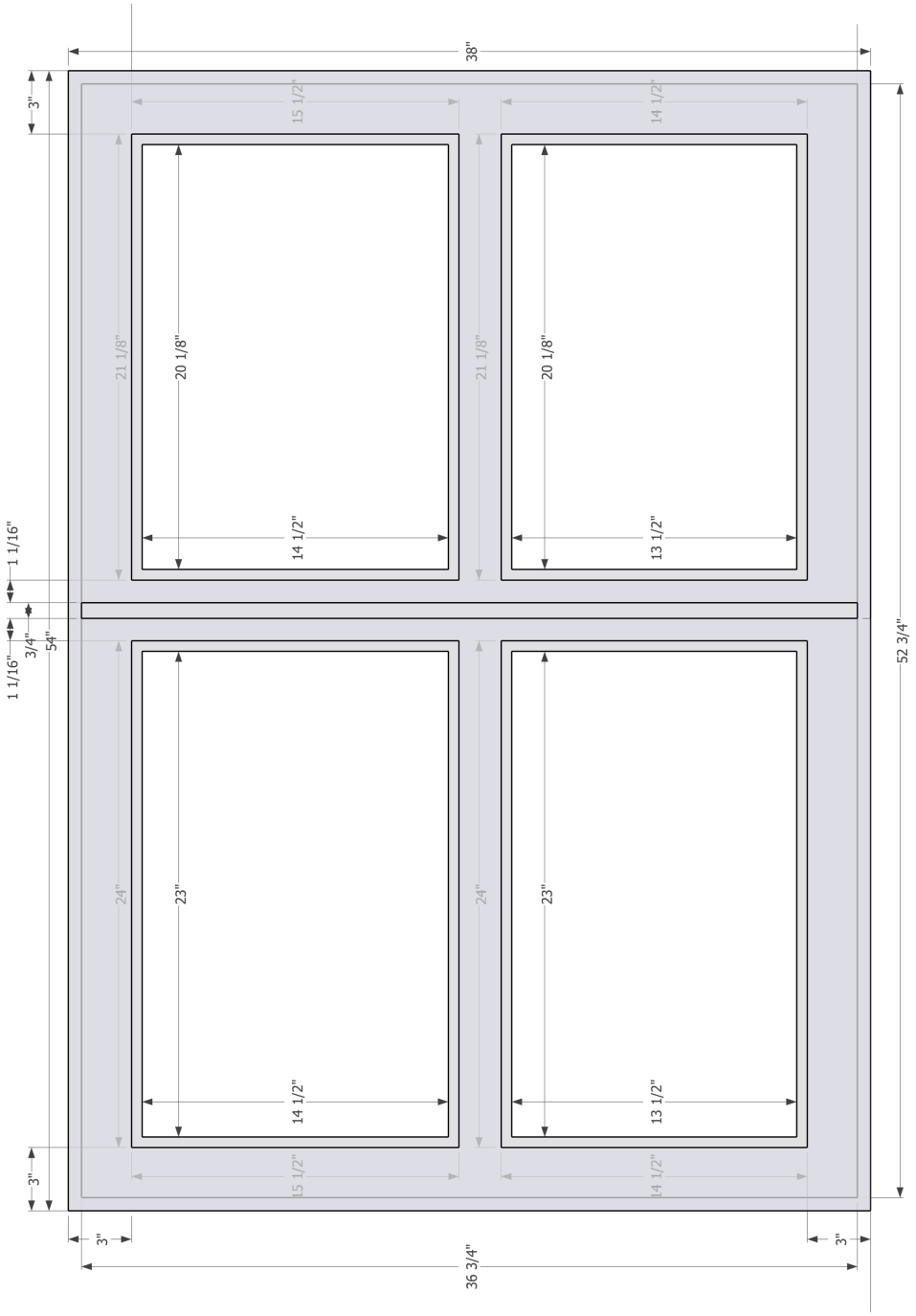

Figure C.7: Top view of the box lid with foam attached.

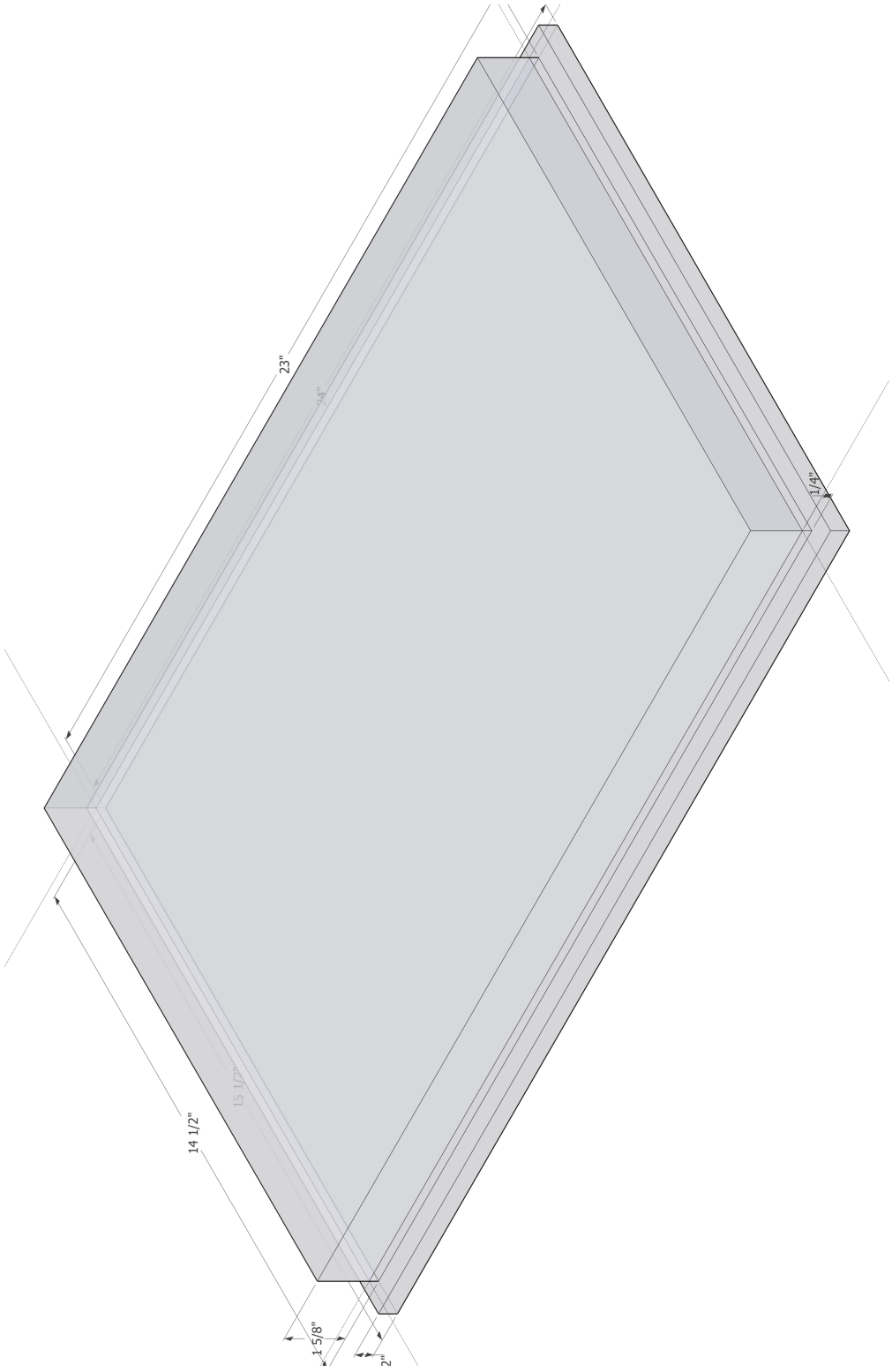

Figure C.8: Three dimensional perspective of a panel for the box lid.

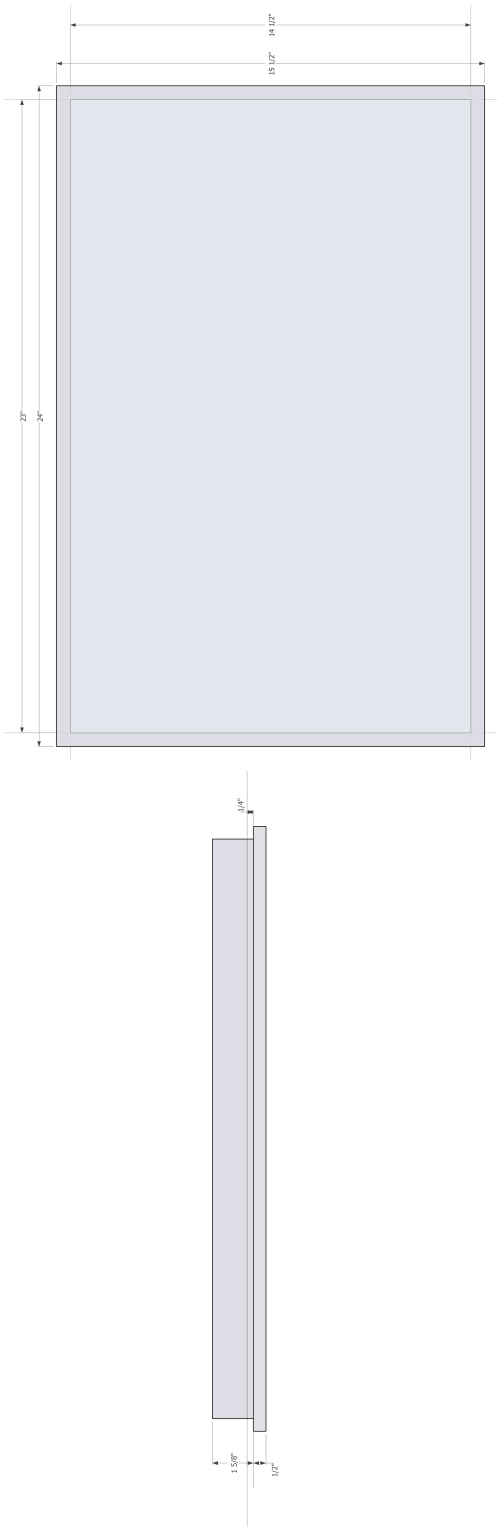

(a) Side view.

(b) Front view.

Figure C.9: Side and front view of a panel for the box lid.

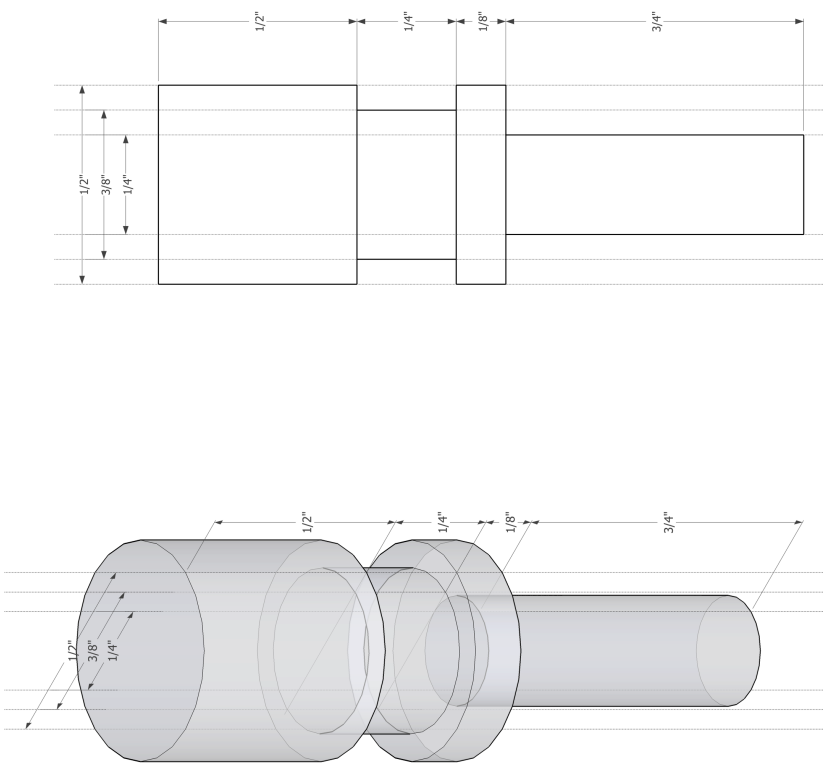

(b) Front view.

(a) Perspective view.

Figure C.10: Three dimensional perspective and front view of alignment screws for the box posts.

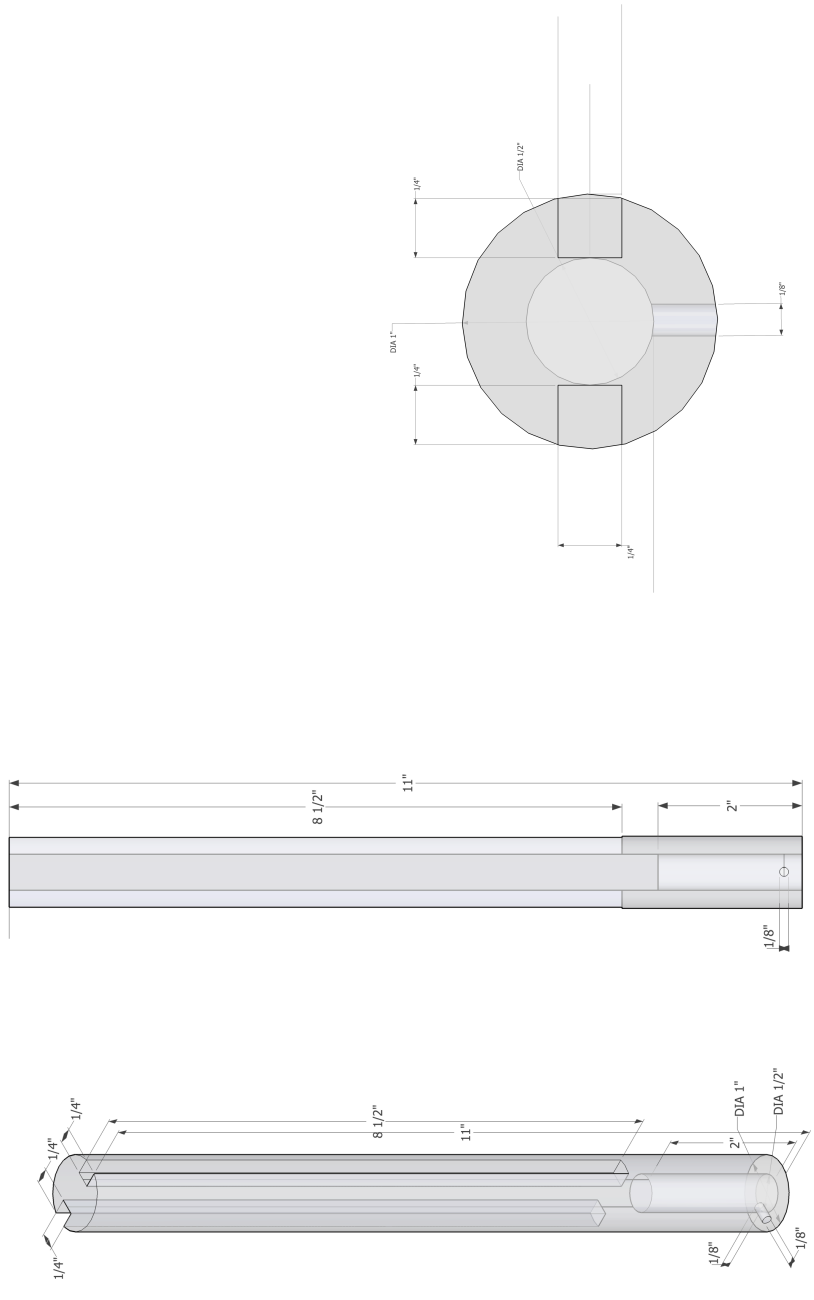

(a) Perspective view. (b) Side view. (c) Top view.

Figure C.11: Three dimensional perspective, side view and front view of the box posts.

C.2 AlphaComposite^{TM}Foam Sheets

AlphaComposite Polyurethane Foam with Peel and Stick Adhesive backing from Acoustical Solutions (www.acousticalsolutions.com) was used to line the interior surfaces of the protective box to provide sound dampening. The foam is comprised of three layers - a 1/4" layer of foam to act as a decoupler, a 1/8" 1 lb. per square foot vinyl sound blocking material, and a 1" of foam for sound absorption.

C.2.1 Technical Data Sheet

Technical data found at www.acousticalsolutions.com/datasheets/data_composite_afbf.asp at the time of writing.

Product Data

Weight:	1 1/4 - 1 1/2 lbs. per sqft.
Flame Spread:	95
Smoke Density:	340
Standard Sheet Size:	2' x 4'

Sound Absorption Data (NRC Values)

Octave Band Frequencies (Hz)	
125:	0.33
250:	0.24
500:	0.63
1000:	1.23
2000:	1.35
4000:	1.14
NRC:	0.85

The Noise Reduction Coefficient (NRC) of an acoustical material is the arithmetic average to the nearest multiple of 0.05 of its absorption coefficients at 4 one-third octave bands with center frequencies of 250, 500, 1000, 2000 Hertz. The NRC rating can be viewed as a percentage (example: .80 = 80%) of what soundwaves that come in contact with the acoustical material are absorbed by the material and not reflected back within the room. Values over 1.0 are due to the way manufacturers test the material.

Sound Transmission Loss

Octave Band Frequencies (Hz)	**dB Reduction**
125:	20
250:	21
500:	25
1000:	28
2000:	32
4000:	42
STC:	29

The Sound Transmission Class (STC) is a measure of the reduction in noise a partition can provided measured in decibels. The final STC value represents a best fit to a set of curves which define the sound transmission class. Note that the STC is heavily weighted to the frequencies used for human speech.